Title
Marine Electromagnetic Exploration of Gas Hydrate in the California Borderlands

Author
Kannberg, Peter

Publication Date
2018

Peer reviewed|Thesis/dissertation

UNIVERSITY OF CALIFORNIA SAN DIEGO

Marine Electromagnetic Exploration of Gas Hydrate in the California Borderlands

A dissertation submitted in partial satisfaction of the
requirements for the degree
Doctor of Philosophy

in

Earth Sciences

by

Peter K. Kannberg

Committee in charge:

Professor Steven Constable, Chair
Professor Alistair Harding
Professor Miriam Kastner
Professor Leonard Srnka
Professor David Victor

2018

The dissertation of Peter K. Kannberg is approved, and it is acceptable in quality and form for publication on microfilm and electronically:

Chair

University of California San Diego

2018

DEDICATION

To Ingrid and Baz.

EPIGRAPH

Numbers is hard and real and they never have feelings
But you push too hard, even numbers got limits
—Mos Def

TABLE OF CONTENTS

LIST OF ABBREVIATIONS

BSR	Bottom Simulating Reflector
CSEM	Controlled Source Electromagnetic
EM	Electromagnetic
HSZ	Hydrate Stability Zone
ILBL	Inverted Long Baseline
OBEM	Ocean Bottom Electromagnetic (receiver)
SUESI	Scripps Undersea Electromagnetic Source Instrument
USBL	Ultra Short Baseline

LIST OF FIGURES

ACKNOWLEDGEMENTS

Steve showed me what it is to be a scientist. Every survey IâĂŹve done with him has been different, because it our equipment and expertise is part of a continuum where they are always improving. There is always something that can be done to make our surveys more accurate and comprehensive, and Steve is always looking for ways to make that happen.

My committee members were exceptionally generous with their time, and every conversation I had with them was fruitful.

EM folk: Every student to work in the lab has benefited from Dave MyerâĂŹs matlab codes, even though he, like his codes, doesnâĂŹt believe in the existence of towed arrays. Never have I ever had a more enjoyable experience working on the deck of a ship than with the EM lab technicians, Jake and Chris. The technicians and engineers, Jacques Lemire and John Souders, are the backbone of our lab, without whom our work would be impossible. IâĂŹd especially like to thanks Karen Weitemeyer for introducing me to EM methods for hydrate. Without our initial conversations, I wouldnâĂŹt be here at SIO. Dallas Sherman has participated in nearly every survey IâĂŹve been a part of, and youâĂŹre welcome for your thesis project.

My cohort, both in IGPP and SIO are an unusually close-knit group. They have made it a joy to be at SIO. Having been to other universities, the SIO community is uniquely cohesive and supportive.

My wife, Julia has been impossibly supportive over the last couple years. My family, especially Julia and our twins, is the greatest thing that has ever happened to me. The last few years have been a whirlwind of life-changing events, and there is no one who I would rather experience those with than Julia.

My parents, Landis and Margaret Kannberg, instilled in me the curiosity and self-confidence that has guided me throughout my life. My dad always showed me the

best way to do something, regardless of how difficult and time-consuming it was. Then my mom would show me that there are far more pragmatic ways to do the same exact thing.

And lastly, I would like to acknowledge my twins, Ingrid Meleana and Sebastian Landis Kannberg. There are entire sections of this thesis that I have no recollection writing, having been written under extreme twin-induced sleep deprivation.

There are no doubt people I am leaving out. To those, I am eternally grateful for your assistance in reaching this milestone.

Ocean Floor Geophysics funded the Del Mar Seep survey.

Santa Cruz Basin collaboration and funding were provided by the U.S. Department of the Interior, Bureau of Ocean Energy Management, Resource Evaluation Division under Agreement Number M13AS00011. Additional funding provided by Ocean Floor Geophysics.

VITA

2004	B. A. in Earth Sciences *with Distinction*, University of Rochester
2003-2006	Marine Laboratory Specialist, Integrated Ocean Drilling Program
2006-2008	Assistant Laboratory Officer, Integrated Ocean Drilling Program
2008	Field Camp Supervisor, High Canadian Arctic
2008-2011	Graduate Research Assistant, Oregon State University
2011-2018	Graduate Research Assistant, University of California San Diego
2018	Ph. D. in Earth Sciences, University of California San Diego

PUBLICATIONS

Sherman, D., Kannberg, P. K., & Constable, S., (2017). Surface towed electromagnetic system for mapping of subsea Arctic permafrost. Earth and Planetary Science Letters. 460. 97-104. 10.1016/j.epsl.2016.12.002.

Constable, S., Kannberg, P. K., & Weitemeyer, K., (2016). Vulcan: A deep-towed CSEM receiver, Geochem. Geophys. Geosyst., 17, 1042-1064, doi: 10.1002/2015GC006174.

Kannberg, P. K., Trehu, A. M., Pierce, S. D., Paull, C. K., & Caress, D. W., (2013), Temporal variation of methane flares in the ocean above Hydrate Ridge, Oregon, Earth Planet. Sci. Lett., 368, 33-42, doi:10.1016/j.epsl.2013.02.030.

SELECTED PRESENTATIONS

Kannberg, P. K., & Constable, S., (2018). Detecting methane hydrate in the Gulf of Mexico using controlled source electromagnetic, Gordon Research Conference

Kannberg, P. K., & Constable, S., (2017). Deep-towed CSEM survey of gas hydrates in the Gulf of Mexico, AGU Fall Meeting.

Kannberg, P. K., & Constable, S., (2016). High Resolution Electromagnetic Mapping of Gas Hydrate Offshore Southern California, AGU Fall Meeting.

Kannberg, P. K., & Constable, S., (2015). Resistivity structure of the Del Mar methane seep, AGU Fall Meeting.

Kannberg, P. K., & Constable, S., (2014). Hydrates in the California Borderlands Revisited: Results from a Controlled-Source Electromagnetic Survey of the Santa Cruz Basin, AGU Fall Meeting.

Kannberg, P. K., Constable, S., & Key, K., (2013). Hydrates in the California Borderlands: 2D CSEM inversion results from towed and seafloor arrays, AGU Fall Meeting.

Kannberg, P. K., & Constable, S., (2012). Mapping methane hydrate with a towed marine transmitter-receiver array, AGU Fall Meeting.

Kannberg, P. K., Trehu, A. M., Weitemeyer, K., Constable, S., & Arsenault, M., (2010). Resistivity and seismic structure at southern Hydrate Ridge, AGU Fall Meeting.

Kannberg, P. K., & Trehu, A. M., (2009) .Heat flow and gas hydrates on the continental margin of India: Building on results from NGHP expedition 01, AGU Fall Meeting.

ABSTRACT OF THE DISSERTATION

Marine Electromagnetic Exploration of Gas Hydrate in the California Borderlands

by

Peter K. Kannberg

Doctor of Philosophy in Earth Sciences

University of California San Diego, 2018

Professor Steven Constable, Chair

Gas hydrate, an ice-like solid formed from methane and water, is prevalent in marine slope sediments. Gas hydrate in sediments is a slope stability geohazard, a potential energy source, a carbon reservoir sensitive to warming oceans, and the base of chemosynthetic ecosystems. Critical to assessing these varied roles is identifying the location and extent of these dynamic hydrate deposits. Acoustic methods historically used to identify hydrate deposits are not as sensitive to the hydrate as they are to the free gas sometimes associated with hydrate. Gas hydrate is electrically resistive which makes it a good target for controlled-source electromagnetic (CSEM) methods.

Presented in this thesis is a deep-towed CSEM transmitter and receiver array system built for identifying gas hydrate deposits, and the results of two surveys in the California Borderlands to assess and characterize hydrate-bearing sediments first at the Del Mar Seep and then in the Santa Cruz Basin. The Del Mar Seep, located in the Inner California Borderlands, is a natural methane seep, but little is known about the hydrate system underlying the seep. Inversion results showed that while the surface expression of the seep is only 200m in diameter, the hydrate system underlying the seep is imaged as a kilometer-wide resistive body. Using Archie's equation, the total gas in place at the Del Mar Seep is 2 billion m^3 at STP. The second survey took place in the Santa Cruz Basin, in the Outer California Borderlands, where indirect seismic indicators of hydrate were found in legacy seismic data. Six lines of CSEM data were collected in the Santa Cruz Basin coincident with seismic data. While the seismic data indicated that most of the hydrate should be in the center of the basin, inversions indicate that resistors are stronger and more prevalent on the flanks, associated with steep migration pathways such as dipping beds and faults. Two shallow resistive bodies are interpreted as undiscovered methane seeps. The Del Mar Seep survey, and very likely the Santa Cruz Basin survey, demonstrate that the deep-towed receiver array is capable of identifying and quantifying methane hydrate deposits.

Chapter 1

Introduction

1.1 Introduction to Gas Hydrate

At high pressures and low temperatures, water and methane can combine to form methane hydrate, a type of clathrate, in which water molecules form in a cage-like structure around the methane molecule (Sloan and Koh, 2007). Conditions necessary for methane hydrate formation are common on continental slopes and arctic permafrost environments. Generically called gas hydrate, the clathrate structure can contain any gas molecule small enough to fit within the bounds of the cages. In addition to methane, carbon dioxide, hydrogen sulfide, and ethane are common guest molecules. The hydrate stability zone (HSZ) is defined as the region that is capable of hosting hydrate given the local temperature and pressure conditions, free gas, and pore water compositions. Hydrates are found worldwide across the ocean slopes and basins, as well as terrestrially in arctic permafrost regions (figure 1.1).

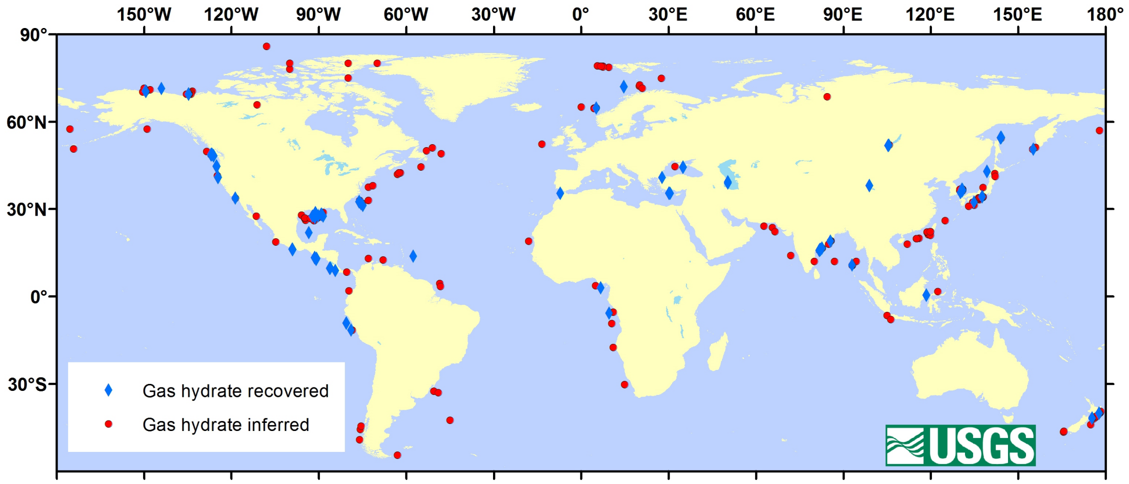

Figure 1.1: Global hydrate distribution, showing both hydrate recovered during coring operations, as well as hydrate inferred from geophysical methods. (USGS Gas Hydrates Project, 2013)

1.1.1 Hydrate Stability Curve

The temperature profile used in calculating the hydrate stability curve (figure 1.2) is a combination of water column temperature above the seafloor, and the geothermal gradient below. Pressure is generally assumed to be hydrostatic, even in the shallow sediments. Hydrates composed of pure methane have a narrower hydrate stability field than those composed of other gases commonly found in seep environments. For example, including carbon dioxide and ethane in the gas hydrate extends the HSZ (figure 1.3). Higher order hydrocarbons in the sediment further complicate the depth extent of the hydrate stability field. Hydrate clathrates can exist in three types: structure-I, the smallest cage size which hosts small guest molecules (e.g. CO_2, CH_4, H_2S); structure-II, whose increased size can host larger molecules such as butane, pentane, and propane; and structure-H, which can host even larger molecules, but is rarely found in nature (Sloan and Koh, 2007). The hydrate stability field of structure-II hydrates extends beyond that of structure-I hydrates, but will only form in the presence of these larger guest molecules. Understanding how these factors interact is necessary to accurately infer hydrate presence with any geophysical tool.

1.1.2 Sources of Methane

A small fraction of any organic matter buried in the sediment is turned into methane, through a process that can occur either biogenically in shallow sediments through microbial processes, which produce exclusively methane; or thermogenically deeper in the section. In addition to methane, thermogenic organic matter degradation generates higher order hydrocarbons, such as ethane, butane, and pentane. The hydrocarbon and isotopic composition of the resulting hydrate forming gas is dependent on the production method, and when combined with the thermal gradient, will determine the local hydrate stability field. A biogenically dominated system will have only structure-I hydrate and a shallow HSZ, while in a similar geologic setting a thermogenic system would have both structure-I and structure-II hydrate and a deeper HSZ. In mixed-gas systems, multiple HSZs may be present, one for each distinct gas mixture. Biogenic methane is isotopically distinguishable from thermogenic methane; biogenic methane is typically depleted in carbon-13 ($\delta^{13}C$) and deuterium (δD) relative to thermogenic sources (Whiticar, 1999). $\delta^{13}C$ is considered to be more diagnostic of methane provenance. In practice, most methane in hydrate systems tends to be of mixed origin.

Abiotic methane has been suggested as a potential methane source for hydrates in certain geologic environments (Johnson et al., 2015). Abiotic methane is the result of hydrated serpentinization of ultramafic rocks, typically at depths of less than 3-4 km where permeability permits fluid flow and temperatures are 200 °C to 350 °C (Martin and Fyfe, 1970; Cannat et al., 2010). If such conditions are present, methane produced within the ultramafic rocks could migrate up through the sediment column and be stored as hydrate. This methane has a unique isotopic signature that is heavily enriched in $\delta^{13}C$ and δD.

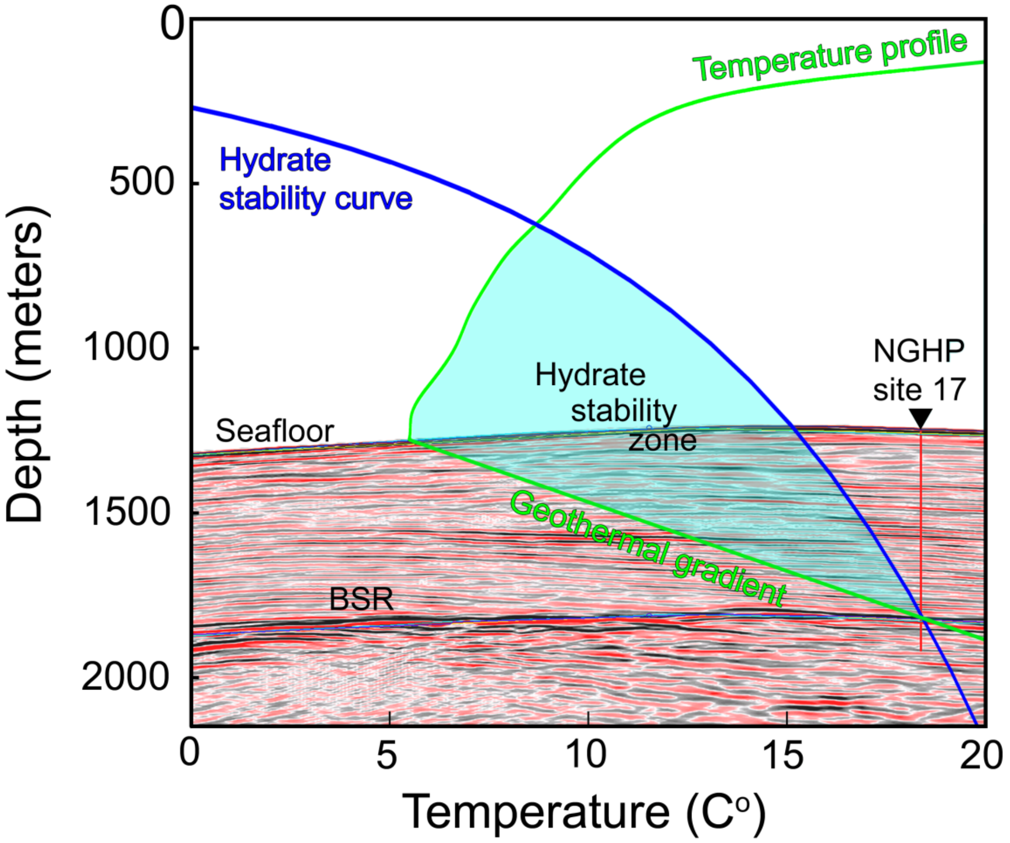

Figure 1.2: Hydrate stability curve from the National Gas Hydrate Program expedition 01 at site 17, in the Andaman Sea. The region between where the temperature profile crosses the stability curve to where it exits at a deeper depth is known as the hydrate stability zone. The seismic velocity anomaly known as the bottom simulating reflector is present at the base of the hydrate stability zone.

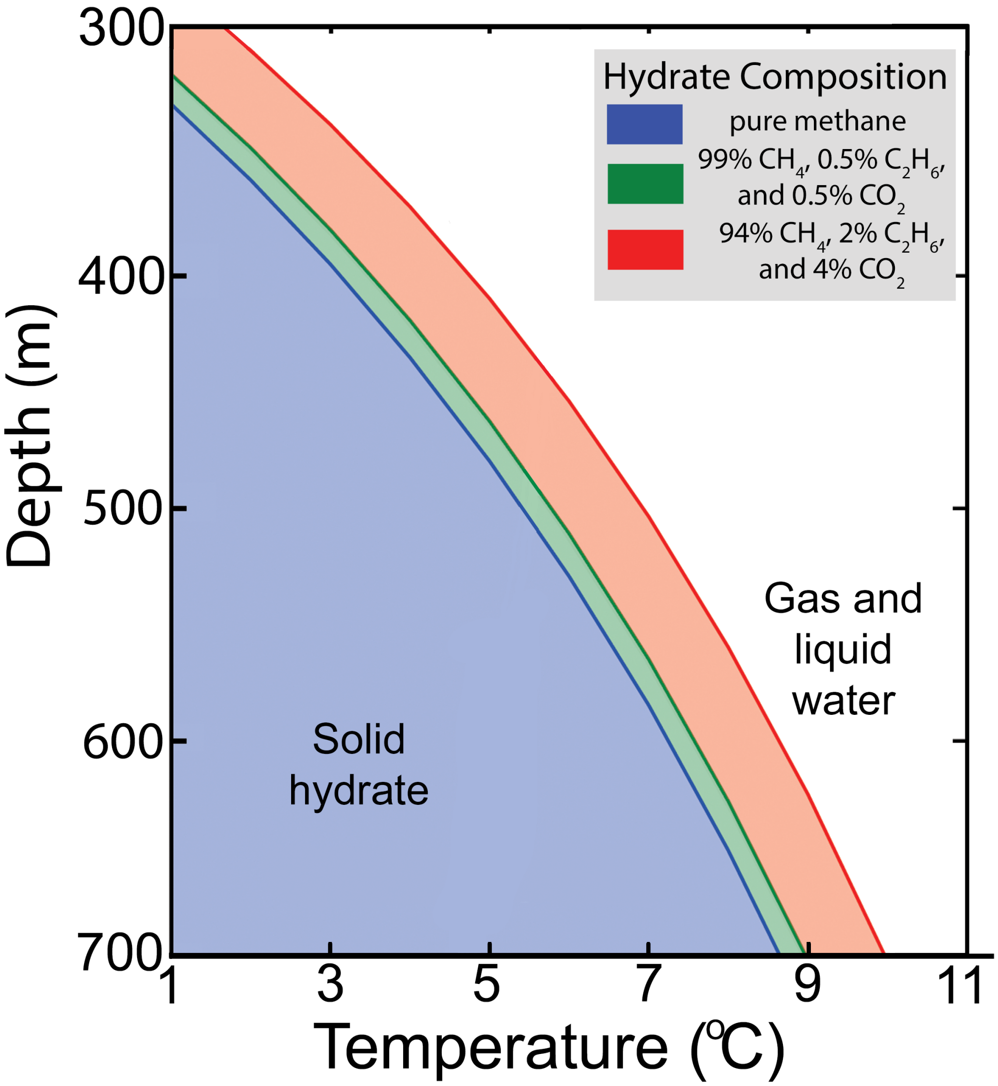

Figure 1.3: Hydrate stability curves for pure methane and mixed gases calculated using Colorado School of Mines' Hydrate software ("CSMHYD") (Sloan and Koh, 2007). Incorporating non-methane gases into the hydrate lattice stabilizes the clathrate, allowing hydrate formation at lower pressures and higher temperatures. Here, gas compositions are from void space samples from cores recovered at northern Hydrate Ridge (Westbrook et al, 1994). (Adapted from Kannberg, 2013)

1.1.3 Geochemical Controls

During hydrate synthesis, water molecules are removed from the pore fluid to construct the cage-like structure surrounding the guest molecule. In the process, the pore fluid becomes more saline as excluded salts accumulate. It is typically thought that the higher salinity fluids are diffusing up to the seafloor and into the seawater above and therefore not observed. Where hydrate synthesis rates are high, this hyper-saline fluid can concentrate in the pore fluids, inhibiting further hydrate formation (Sloan and Koh, 2007). Accumulation of these brines can create a situation where hydrate, free gas, and dissolved methane can coexist, providing a pathway for free gas to transit through the HSZ. This brine-inhibition model is proposed to exist near the summit of South Hydrate Ridge offshore Oregon, USA, when hyper-saline pore fluid samples were found in cores recovered during IODP Leg 204 (Milkov et al., 2004). While hypersaline brines have been found near the seafloor, they have not been recovered from deeper hydrate formations.

1.2 Hydrate as Hazard and Resource

Hydrates are a reservoir of carbon that has the potential to exacerbate climate change and ocean acidification, provide an unconventional energy resource, complicate drilling operations, and endanger seafloor infrastructure. Identifying the extent and concentration of hydrate in a given area is necessary to determine the impact hydrate will have in these scenarios as discussed in greater detail in the following sections.

1.2.1 Climactic and Ocean chemistry hazard

Determining the presence of seeps, and the potential volume of methane these reservoirs represent is essential to understanding the chemical balance of the oceans. Under certain circumstances, methane gas released from the seafloor as bubbles has the potential to reach the atmosphere. Where ocean water concentrations of methane are less than the concentration of methane in the bubbles, as is the case in most of the ocean, the methane gas should dissolve rapidly. However, numerous cases of inhibited dissolution have been documented and are attributed to the presence of bubbles coated in either oil or hydrate, sequestering the methane in the bubble and preventing it from interacting with the surrounding water mass (Merewether et al., 1985, MacDonald et al., 2002, Rehder et al., 2009). Bubbles may remain armored by hydrate skins as long as they remain within the hydrate stability zone (Rehder et al., 2002, Heeschen et al., 2003, Kannberg et al., 2013). As the hydrate-armored bubbles extend beyond this zone, the hydrate skin should dissociate, dissolving the trapped methane. Through a microbially mediated process, dissolved methane will then oxidized into carbon dioxide over time-scales of days to months, potentially exacerbating ongoing ocean acidification (Valentine et al., 2001, Grant and Whiticar, 2002).

Methane is a potent green house gas, 28 times more effective at trapping heat than carbon dioxide over 100 years in spite of only having a residence time of 10 years in the atmosphere before being oxidized into carbon dioxide (IPCC, 2014). Bubbles released from shallow cold water seeps, such as in the arctic, are capable of reaching the mixing zone and venting to the atmosphere because the transit time of the bubbles though the water column is less than the dissolution time. As mentioned previously, armoring of the bubbles, either with oil or surfactants, is another way to inhibit dissolution and gas exchange allowing methane released from deep seeps to reach the sea surface (Leifer and MacDonald, 2003). Rapid releases of methane at the seafloor can saturate the local water with methane. The entrained flow increases bubble rise rate promoting extension of the bubble plume to the sea surface (Leifer et al., 2006). Lastly, solid pieces of methane hydrate can either break off seafloor outcrops, or be released as part of a mass-wasting event. These buoyant blocks of hydrate will not begin to dissociate until reaching the upper limit of the HSZ, at which point they begin to emit gas. Depending on local water temperature and depth, it is possible for these hydrate blocks to reach the surface and vent directly to the atmosphere (Brewer et al., 2002, Paull et al., 2003).

1.2.2 Drilling Hazards

Methane hydrate has been recognized as a potential drilling hazard since the 1980s (McConnell et al., 2012). Initial hazard assessments focused on avoiding seafloor morphology characteristic of natural seeps until deep-water oil exploration prompted the discovery of deeply buried gas hydrates in the 1990s. Typically, diffuse hydrate poses little hazard to drilling operations, and can be easily managed using existing technology. A greater hazard is created when hydrate-bearing sands seismically mask the presence of significant quantities of overpressurized free gas, such as occur in deepwater Gulf of Mexico. In this case, the hazard results from the presence of gas, while the hydrate serves as the caprock leading to overpressures. Counterintuitively, hydrate cementation of sediment grains can promote borehole stability (Collett et al., 2012). Potential hazards are most commonly dealt with through avoidance. Once the hazard is identified, the drilling site is moved off-hazard and the target drilled horizontally. Production boreholes offshore Malaysia had to be moved at great expense after drilling through hydrates, in order to avoid thermally-induced hydrate dissociation and subsequent sediment subsidence and destabilization caused by producing warm fluids (Hadley et al., 2008).

However, as McConnell (2010) notes, “simple avoidance... of wells located in gas-hydrate-prone areas without regard to evaluation of the actual hazards, is clearly not optimal”. Identification of hydrate as a drilling hazard has focused exclusively on seismic methods. CSEM methods do not exhibit the same sensitivities to low saturations of free gases, and could represent a better method of imaging gas accumulations that are obfuscated by hydrates in seismic data.

1.2.3 Slope Stability Hazard

Potential hazards associated with hydrate dissociation driven slope failure were first identified by McIver (1977). Overpressures resulting from dissociating hydrate at the base of the HSZ and the decrease in sediment strength as the sediment transitions from hydrate cemented to hydrate free are hypothesized to lead to slope instabilities (Kvenvolden, 1993; Priest and Grozic, 2016, Crutchley et al., 2016). Additional instabilities within the HSZ can form when cemented hydrate sediments provide a glide plane for the overriding sediments (Yelisetti et al., 2014). There is also evidence that hydrate cemented sediment packages can slowly deform, similar to glaciers (Mountjoy et al., 2014). All of these mechanics represent significant hazards to any infrastructure located on or below hydrate bearing sediments.

1.2.4 Hydrate as Energy Resource

The amount of carbon sequestered as methane hydrate in the ocean sediments is immense; estimates range from $1\text{-}100\times10^{15}$ m^3 of hydrate-bound gas (Collett and Boswell, 2011). The large uncertainty of these estimates derives from uncertainty in estimated initial organic matter content and rate of conversion to methane, sediment volume within the HSZ, and gas hydrate concentration in those sediments. The vast majority of this hydrate is diffuse hydrate found in low concentrations in deep marine clays. The technically recoverable resource is the product of the fraction of hydrate that is thought to be recoverable using existing technology and the fraction of gas hydrate that can be produced within a given period of time. It is used to provide a more realistic estimate of hydrate volume from an energy perspective. The TRR global hydrate volume is estimated to be 3×10^{13} m^3 of free gas (Collett and Boswell, 2011). The total proved natural gas resources worldwide are 1.87×10^{14} m^3, roughly six times the technically recoverable resource volume of hydrate (BP review of global energy resources, 2014), However, as our understanding of how to extract known hydrate deposits increases, the fraction of technically recoverable hydrate will increase.

1.3 Hydrate Exploration Techniques

The base of the HSZ represents the transition from free gas to solid hydrate. As methane is formed deeper in the sediment section and advects into the HSZ, hydrate is formed. Hydrate formation clogs pore throats, concentrating free gas at the lower edge of the HSZ. When imaged using acoustic methods, the free gas negative velocity anomaly can be a prominent reflection, known as the bottom-simulating reflection (BSR). The depth of the HSZ is locally defined by the geothermal gradient, and, with other factors being equal, the BSR will be present at a constant depth below the seafloor, regardless of bathymetric changes.

1.4.1 Changing ideas about what the BSR represents

Historically, the BSR has been to used infer hydrate presence, but with increasing understanding of hydrate systems and resultant BSRs, the association between BSR and hydrate becomes more complex (Hillman et al., 2017). Three types of hydrate related BSRs have been identified: continuous, discontinuous and pluming (Shedd et al., 2012). Continuous BSRs are large-scale features extending across basins, such as in the Santa Cruz Basin, or encompassing bathymetric highs, such as at Hydrate Ridge, offshore Oregon, or Blake Ridge, offshore South Carolina (Tréhu et al., 2004; Shipley et al., 1979). BSRs found at these sites cross-cut stratigraphy, and were the first BSRs identified to be associated with hydrates. Discontinuous BSRs are isolated to certain sedimentary beds as they cross into the HSZ, and are common in the Gulf of Mexico (Hillman et al., 2017). At present, discontinuous BSRs are thought to indicate higher hydrate saturations than continuous BSRs sites and are increasingly targets for energy exploration and extraction. Pluming BSRs are found in places where localized advective fluid flow shoals the base of the HSZ, which causes and abrupt vertical shift in the depth of the BSR, but conductive thermal effects dominate the geothermal gradient in most hydrate bearing regions (Shedd at el., 2012).

In certain situations, the BSR does not represent the thermodynamic base of the HSZ. While temperature and pressure are first order controls on HSZ depth, how the BSR manifests relative to the HSZ is also dependent on methane flux rate, methane solubility, porosity, and permeability (Xu and Ruppel., 1999; Hillman et al., 2017). The base of the HSZ is a transition zone where free gas, hydrate, and pore fluid exist simultaneously. The slope of the geothermal gradient will control the abruptness of the base of the HSZ, with larger gradients resulting in shorter transitions zones. The BSR will typically occur within the transition zone where the shallowest free gas is present, and hydrates can be found below the BSR (Guerin et al., 1999; Liu and Flemings, 2007). However, in certain situations, a BSR may form in the absence of free gas (Hyndman and Spence, 1992).

Seismic acquisition methods will also determine how a BSR manifests in seismic profiles. Low resolution seismic lines tend to show continuous BSRs while higher frequency collocated seismic lines indicate discontinuous BSRs. Hillman et al. (2017) suggest that there is no such thing as a continuous BSR, just discontinuous BSRs that are imaged at the wrong frequency. The BSR is best imaged in seismic lines that are perpendicular to bedding strike. If the geometry of the sediment beds is unknown, it is feasible that a BSR could go undetected by a misaligned seismic survey (Hillman et al., 2017).

The most revealing evidence of the inadequacies in using BSRs to infer hydrate presence comes from a study of boreholes in the Gulf of Mexico. Majumdar et al. (2016) reviewed resistivity well logs from 788 boreholes in the Gulf of Mexico, of which 35 crossed a BSR. Of those 35 BSR-crossing wells, only 13 (37%) showed resistivities of at least 0.5 Ωm above background across a 10 m thick section, which was the threshold for interpreting hydrate occurrence. Additionally, of the 753 wells that did not intersect the BSR, 103 (14%) showed evidence of hydrate. A BSR will increase the likelihood of finding hydrate bearing sediments by 2.6 times, but hydrate presence cannot be directly inferred from a BSR. Additionally, the presence of a BSR does not usefully constrain concentration and distribution of hydrate in the sediments above it.

1.4.2 Limitations of Acoustic Methods

Acoustic methods, such as seismology, are sensitive to the velocity and density of the medium the waves are traveling through. Velocities of typical shallow ocean sediments are slightly higher than that of ocean water, ranging from 1.5 km/s to 1.6 km/s. Velocities will increase in hydrate rich beds, but the degree of increase will depend on hydrate formation type, with hydrate cementation of sediment grains causing a large increase in velocity, while hydrate forming in the pore space will cause a smaller increase in velocity. Slow velocity and low density free gas have a confounding effect on acoustic methods in hydrate areas. In methane seep environments where gas flux outpaces hydrate formation rates, free gas will be present within the HSZ. Free gas concentrations as low as 15% of pore space volume will halve the acoustic velocity in 50% porosity sandstone (Lee, 2004). Seismic methods will underestimate hydrate saturation if unaccounted for free gas is present in the system. Additionally, seismic methods are typically higher resolution than electromagnetic (EM) methods, but inverting seismic data for velocity produces models with resolutions similar to those of EM inversions (e.g. Weitemeyer et al., 2011) unless very high effort seismic methods (i.e. Full Waveform Inversion) are used with broadband data.

1.4.3 Hydrate Resistivity Measurements

Increased electrical resistivity of hydrate bearing sediments was first observed academically in well logs from the Alaskan permafrost and offshore Guatemala in the 1980s (Collett and Ladd, 2000). Borehole logging methods are the most reliable way to determine hydrate concentration and vertical distribution but are an expensive method that only provides point measurements. Hydrate presence is inferred from boreholes using a suite of downhole tools, including electrical resistivity, acoustic velocity, sediment density, neutron porosity, borehole diameter, and spontaneous potential. Of those borehole measurements, electrical resistivity logs are most commonly used to calculate hydrate saturation. Typically, methods (i.e. Archie's equation) for converting electrical resistivity into hydrate saturation have come out of hydrocarbon exploration techniques, but their applicability to the unique environment and thermodynamics of hydrates has not been established (figure 1.4).

Calculating hydrate resistivity, in both pure hydrate and mixed systems, is necessary in order to best know how to apply mixing laws to determine hydrate saturation (Spangenberg and Kulenkampff, 2006). In most hydrate systems, the conductivity of the sediments is dominated by pore water conductivity. However, in massive hydrate beds where production will be most economical, the conduction pathway is dominated by the conductivity of hydrate itself. Understanding both of these end members, from disseminated pore space hydrates to massive pore-filling hydrate bodies, improves interpretation of electrical resistivity well logs and CSEM survey results. Pure hydrate is 2.3×10^4 Ωm at 0° C, but hydrate resistivity is temperature dependent and decreases to 1.2×10^4 Ωm at 10° C (Du Frane et al., 2011). Pure hydrate can be found near the seafloor at methane seeps, but hydrates are typically in mixed sediment systems. Du Frane et al. (2015) measured resistivity of sand-hydrates mixes at a variety of sand concentrations and temperatures to emulate pore-filling hydrates in water free reservoir-grade sandstone. At 45 volume percent (vol %) sand and 55 vol % hydrate, resistivity was measured at 2.8×10^3 Ωm and 2.5×10^3 Ωm at 0° C and 10° C, respectively. These laboratory measured resistivities closely match recent well logs from offshore Joetsu, Japan, where resistivities measured regularly exceeded 10^3 Ωm, and peaked at 10^4 Ωm (Matsumoto et al., 2017). Other lab measurements of mixed systems found lower

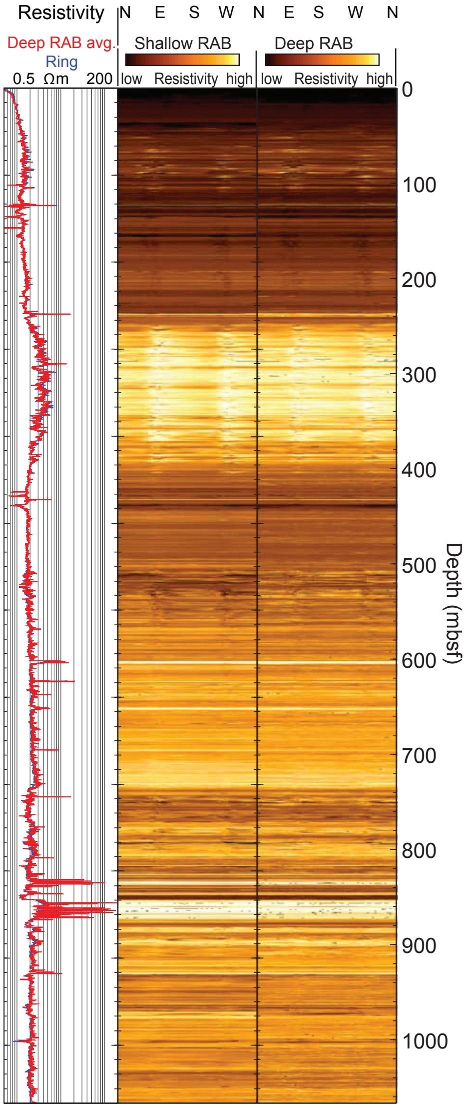

Figure 1.4: Electrical resistivity logged in hole G at Walker Ridge 313 as part of the Gulf of Mexico Gas Hydrate Joint Industry Project, Leg II (Cook et al., 2009). Increased resistivity is a commonly interpreted indicator of hydrate presence in borehole logging data.

resistivities at equivalent hydrate saturations than those measured by Du Frane et al. (2015). Spangenberg and Kulenkampff (2006) measured 265 Ωm in a 62 vol % sand and 36 vol % hydrate, but had 2 vol % free water, which could explain why this study differed from Du Frane et al. (2015). Hydrate resistivity is mildly temperature dependent, but resistivity is largely dependent on hydrate saturation and sediment porosity.

This thesis details the procedures for, and results of, using the CSEM method to explore hydrate bearing sediments. Chapter 2 discusses the CSEM method and instrumentation used to collect marine electromagnetic data over hydrate targets. Chapter 3 examines the use of CSEM to image hydrate underlying the Del Mar Seep, an active methane seep in the San Diego Trough. The 4th chapter explores the hydrate potential of the Santa Cruz Basin using CSEM. Chapter 5 reviews these surveys in a broader scientific context, and evaluates the future use of this method.

Chapter 2

CSEM Methods and Instrumentation

2.1 CSEM Theory

Controlled Source Electromagnetic (CSEM) methods use a transmitted electric or magnetic signal which propagates through the environment and is observed on electric or magnetic receivers. The transmitted signal is attenuated by the surrounding environment, the degree to which is dependent on the local resistivity structure. Resistive environments are preservative of the original signal while conductive regimes are more attenuative. The transmitted electric field can be modified in three ways: firstly through geometric spreading, where the amplitude of the signal falls off over radius cubed, but phase is unaffected. Similarly, the galvanic effects induce amplitude change, but no phase shift, and occur where resistivity abruptly changes. Electric field amplitude will increase with decreasing conductivity. Lastly, inductive attenuation decreases amplitude and causes a phase shift. Inductive attenuation will occur independent of resistivity contrasts. All three of these effects will be present, the combined effect being dependent on the environment.

2.1.1 Skin Depth Attenuation

Inductive attenuation in a given environment is a function of the conductivity of the environment and the frequency of the signal. This relationship is defined by the skin depth, which is the depth at which the amplitude of a plane wave electromagnetic signal will decrease by 1/e (~37%) and phase is delayed by 1 radian (~57°) in a uniform medium. The general form of the electromagnetic attenuation factor, α, (after Burger et al., 2006) is:

$$\alpha = \omega\left\{\frac{\mu\varepsilon}{2}\left[\left(1+\frac{\sigma^2}{\varepsilon^2\omega^2}\right)^{\frac{1}{2}}-1\right]\right\}^{\frac{1}{2}}$$

where ω is the angular frequency, μ is the magnetic permeability, which in non-magnetic media is $4\pi\times10^{-7}$ Farads per meter (F/m), ε is the dielectric permittivity in F/m, and σ is the conductivity in Siemens per meter (S/m). At low frequencies, such as those used in CSEM, and at common marine conductivities, $\frac{\sigma^2}{\varepsilon^2\omega^2} \gg 1$, and written in terms of skin depth (), the inverse of the attenuation factor, the equation can be reduced to:

$$\delta = \left(\frac{2}{\mu_0\sigma\omega}\right)^{\frac{1}{2}}$$

When calculated for $\mu_0 =$ $4\pi\times10^{-7}$ F/m, angular frequency converted to frequency ($\omega = 2\pi f$), and written in terms of resistivity (ρ) the equation becomes:

$$\delta \approx 504\left(\frac{\rho}{f}\right)^{\frac{1}{2}}$$

The frequencies used in this thesis to map methane hydrate range from 0.5-13.5 Hz , which result in skin depths of 390 m at 0.5 Hz and 75 m at 13.5 Hz in 0.3 Ωm seawater. Shallow marine sediments are typically 1 Ωm, which gives skin depths of 712 m and 137 m at 0.5 Hz and 13.5 Hz, respectively.

2.1.2 CSEM Method

While high frequency magnetotelluric signals are usable in resistive terrestrial environments, in the marine environment, the conductive seawater attenuates high-frequency signals. The loss of those frequencies limits the ability of the MT method to accurately resolve shallow resistivity structures. To mitigate this effect, a transmitter is used to re-transmit a portion of those missing frequencies into the marine environment just above the seafloor. There the transmitted current is well coupled to the seafloor and little electric field strength is attenuated in seawater. However, while the conductive seawater attenuates signal, it also allows for large electric currents to be transmitted and attenuates magnetotelluric and man-made noise in the CSEM frequency spectrum.

The basic methodology of the CSEM method is to tow a transmitter at or just above the seafloor, and then record its transmitted signal on stationary seafloor or towed receivers. In the marine environment, multiple transmitter types have been used (Edwards, 2005), but the most widely employed, including the work presented in this thesis, is the horizontal electric dipole (Constable and Srnka, 2007). A horizontal dipole transmitter has the advantage over vertical electric or magnetic transmitters of inducing both horizontal and vertical current flow which creates galvanic effects on both vertical and horizontal boundaries. To take full advantage of this, receivers need to be capable of sensing both horizontal and vertical fields. While magnetic field measurements can be made on seafloor instruments, magnetic field receivers are impractical on towed receivers due to their sensitivity to instrument movement in Earth's large magnetic field. The transmitter (SUESI) and receivers (known as Vulcans) used in this thesis are described in detail later in this chapter.

CSEM data acquisition can be either in the time- or frequency-domain. The physics controlling each are the same, but operational considerations typically favor frequency-domain data acquisition in the marine environment (Constable and Srnka, 2007). Square-wave harmonic amplitude falls off geometrically, so modified square waves are specifically designed to amplify desirable frequencies. Scripps Institution of Oceanography typically uses "waveform D," a waveform designed to provide useable frequency content across a couple decades of frequencies (Myer et al., 2011). Time-domain data are Fourier decomposed into amplitude and phase to recover frequency-domain data for analysis and inversion. By computing the Fourier coefficients for each pre-whitened fundamental waveform, and then stacking, statistics on data errors can be calculated. In practice, data errors are often much smaller than errors resulting from uncertainty in array navigation and geometry.

2.1.3 CSEM for Hydrate Targets

Methane hydrate is typically found in the upper few hundred meters of sediment. These shallow targets require novel survey design in order to properly resolve the shallow geology. These surveys require relatively short source receiver offsets, and consequently small source-dipole moments in order to keep near-transmitter receivers from saturating. Depth resolution is controlled through the use of multi-frequency waveforms and by using multiple source receiver offsets. Due to the relationship between frequency and skin depth attenuation, higher frequencies sample shallower geology, while lower frequencies can penetrate into deeper structure. Likewise, the greater the source-receiver offset, the deeper the sensitivity. In a typical hydrocarbon CSEM survey, where target depths extend to kilometers, seafloor receiver spacing is often too large to adequately sample hydrate bearing sediments. Additionally, large source dipoles required to penetrate deep targets will saturate at close source-receiver offsets, limiting their use in defining the near-seafloor resistivity. The upward shift in target depth leads to the natural progression from seafloor receivers to towed receivers, where sensitivity to deep structure is sacrificed for enhanced resolution in the shallow sedimentary section. Through the use of multiple frequencies and multiple fixed source-receiver offsets, the shallow sediment where hydrate exists can be adequately sampled.

The transition from seafloor receivers to towed receivers resulted in new problems such as greater uncertainty in receiver geometry, while reducing other issues such as errors resulting from uncertainty in source-receiver offset. Additionally, data density increased greatly, increasing computational intensity of models. Computational efficiencies can be used to model seafloor receiver data such as transmitter-receiver reciprocity, where the number of transmitter positions modeled is much greater than the number of receiver positions. In this case running electric field calculations for each receiver position rather than for each transmitter position can reduce the number of calculations. Reciprocity is not applicable to a towed multi receiver array where the number of receiver positions will always be greater than the number of transmitters.

2.2 CSEM Towed Instrument Array

2.2.1 SUESI Electric Field Transmitter

The Scripps Undersea Electromagnetic Source Instrument (SUESI) is used to transmit electrical current into the ocean and underlying geology as part of a CSEM survey (figure 2.1). SUESI is a deep towed 500A transmitter, typically “flown” 50-150 m above the seafloor. SUESI is capable of operation at depth up to 6000 m with data from onboard sensors telemetered in real-time via the tow cable to the shipboard operators. While SUESI’s original intended use was in conjunction with seafloor receivers, its adaptability has permitted it to be the foundation of a deep-towed receiver array.

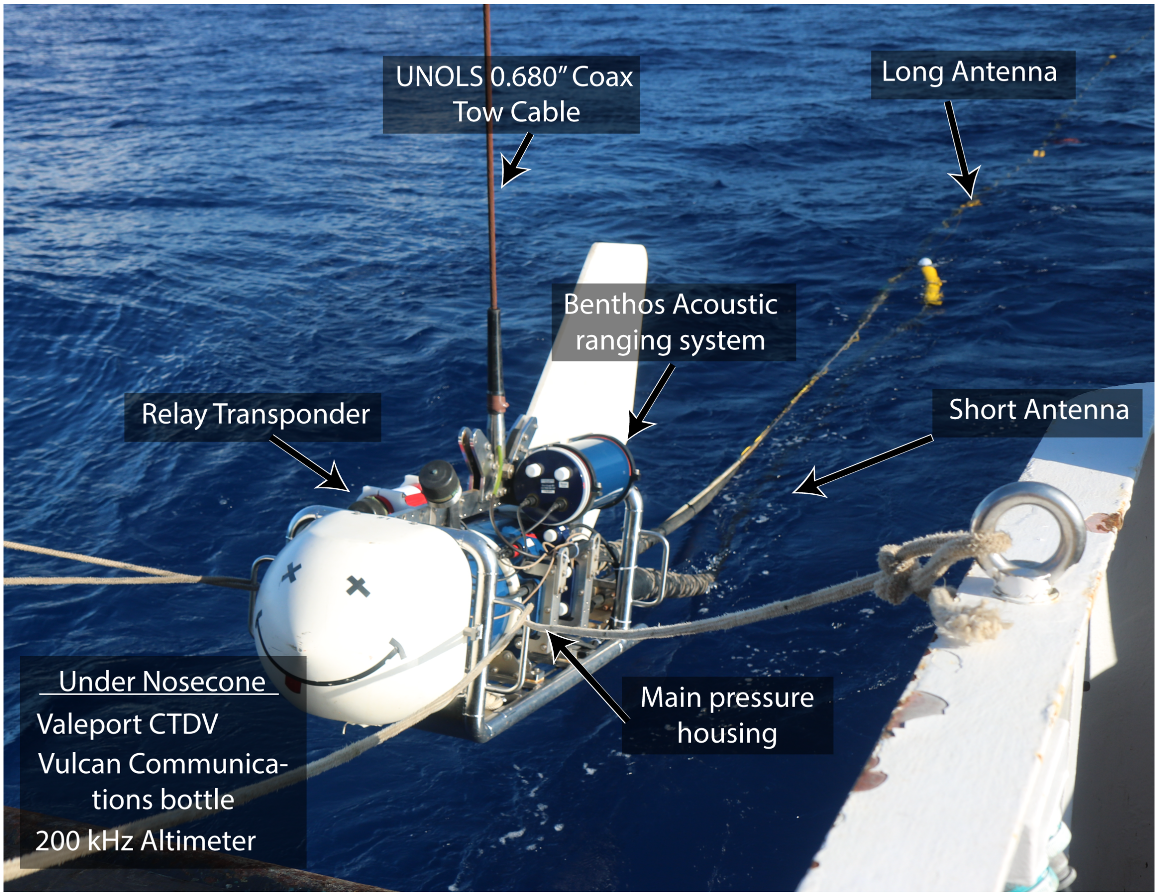

Figure 2.1: Scripps Undersea Electromagnetic Source Instrument (SUESI) being deployed off the back deck of the R/V Point Sur.

The electric signal generated by SUESI at the seafloor starts as a 400 Hz phase locked signal created by a GPS timing unit aboard the ship. This signal is passed to the SUESI control deckbox, where the GPS square wave is converted to a variable amplitude sine wave. The sine wave is then used as input to a programmable power supply ("Elgar") where it is amplified and transformed to 0-2000 VAC. This voltage is then transmitted down the 0.680" (17 mm) standard coaxial tow cable to SUESI. The deckbox is also responsible for imprinting a frequency-shift keyed communication signal on the high voltage power, which is separated by a cross-over network in SUESI. The frequency-shift keyed signal allows 9600 baud bi-directional communication. While

SUESI is capable of utilizing a fiber optic tow cable, which allows much faster data communications, coaxial cable is still required to transmit the high voltage. Coaxial fiber optic cables can be made, but the standard fiber optic cable for research vessels includes 3-phase conductors, and cannot be used with SUESI's 400 Hz power.

Inside SUESI, the high voltage is transformed down to 0-260 VAC to power the 24 V onboard control and auxiliary systems using a standard wide input power supply, and 0-40 VAC for the main transmitted current. SUESI is capable of transmitting up to 500 A, but in practice this is often less, restricted by antenna design or survey requirements. For example, a 100 A signal is enough to image the upper 200 m of sediment with a short towed receiver array. Additionally, operating the Elgar and SUESI below their maximum output current increases reliability. A Hall effect sensor measures transmitted current and waveform shape on the antenna. Accurate current measurements are necessary for data processing as the receiver signal is normalized by the source dipole moment. Six underwater connectors supply 24 V power and communications to a number of auxiliary systems. Four connectors are used for a 200 kHz Kongsberg acoustic altimeter, a Valeport brand conductivity, temperature, pressure, and seawater velocity sensor, an acoustic Benthos ranging system for navigation, and a Vulcan telemetry system described in section 2.3.3. These sensor measurements are relayed back up to the shipboard SUESI control deckbox and displayed on a graphical user interface (GUI) which is used by the winch operator. The remaining two power and comunication ports can be used for mission-specific sensors as desired, such as a dissolved methane sensor when towing in seep environments, or powering a USBL transponder.

The transmitted current is passed from SUESI to the seawater via an antenna. Two custom made aluminum cored cables exit the aft end of SUESI and carry the current to copper electrodes that tip each cable. One of the two cables is a fixed 10m length to the near electrode while the second, longer cable and accompanying electrode defines the dipole length. Transmitted current amplitude is largely a function of seawater conductivity, dipole separation, and electrode length. Electrode length is limited to 10% dipole length in order to satisfy the approximation that electrodes are points in space as defined by modeling software (Constable et al., 2016). Electrode diameters are between 0.5 in. (13 mm) and 1 in. (25 mm). Increasing electrode diameter has little effect on output current, but larger sizes are less susceptible to corrosion and brittleness caused from use and can carry larger currents with less loss.

An antenna tail-end transponder (A-TET) is towed behind the antenna. The A-TET contains a compass, pitch, and roll sensor; a pressure sensor; an acoustic transponder; and an RS232 communications isolation board. The pressure sensor is important for determining dip of the antenna, while the acoustic transponder is navigated acoustically using one of the methods described later in section 2.2.3. The communications isolation board controls telemetry that extends from SUESI to the A-TET and the Vulcan array twinned to the antenna. The current in the transmitting dipole induces noise in the telemetry cable and the communications isolation board prevents this from corrupting communications and electric field signal.

SUESI is used in conjunction with an armored coaxial 0.680 in. (17 mm) tow cable commonly found on academic research ships. The tow cable is run through the block on the ship’s A-frame and the armored portion is terminated at the lift point on

SUESI. The coaxial core is connected to the transformer pressure case of SUESI, delivering both high voltage power and FSK communications. The ship moves at 1-3 knots during deployment to ensure tension on the antenna and Vulcan array. Once the array and antenna are in the water, a decktest of the SUESI electronics is performed to make sure all of the electronic components are functioning, SUESI is capable of transmitting, and that the deckbox is capable of communicating with SUESI and the Vulcans. SUESI is launched after a successful deck test and is lowered at 10 m/min until reaching 100 meters above seafloor. At that point, winch control is switched to the laboratory, where the winch operator has access to the SUESI GUI showing array geometry and SUESI altimeter and depth.

2.2.2 SUESI Waveform

As SUESI is lowered to the seafloor, it records a conductivity, temperature, and depth (CTD) profile of the ocean, which is used for acoustic navigation of receivers and transmitter as well as accurately including seawater conductivity in models. SUESI is capable of transmitting custom ternary waveforms, but is most often programmed to transmit what is colloquially known as "waveform-D" (Myer et al., 2011). Waveform-D is a doubly symmetric binary waveform that injects energy into 5 or 6 frequencies across the first 3 decades of harmonics, in contrast to a square wave that exhibits a geometric decrease in energy with increasing harmonics (figures 2.2 and 2.3). Due to skin depth attenuation, lower frequencies are sensitive to deeper structures than high frequencies. Increasing the frequency content of the transmitted signal is one way to enhance depth resolution (Constable et al., 2015).

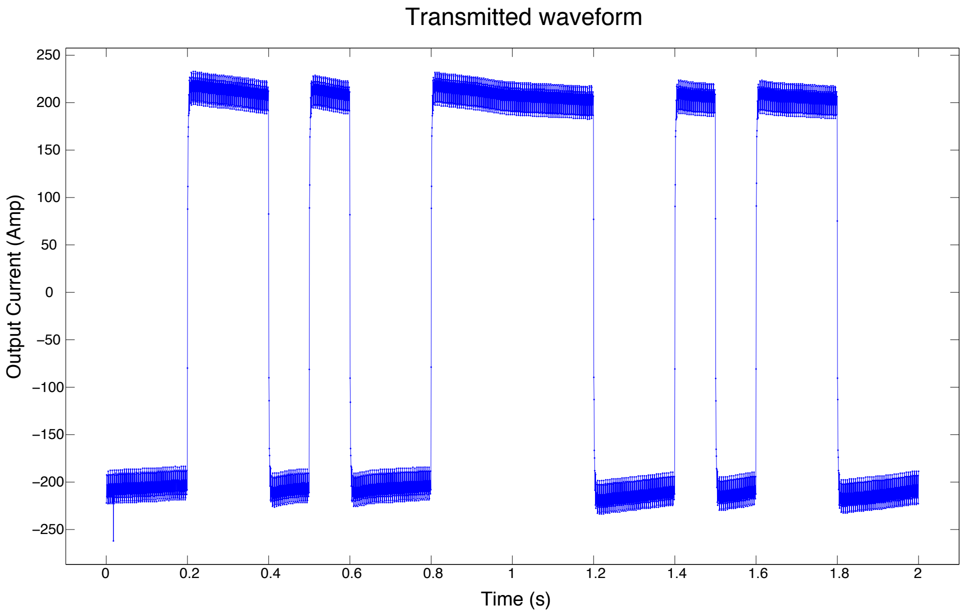

Figure 2.2: “Waveform-D” as transmitted by SUESI, recorded using a hall-effect sensor and transmitted to the shipboard operators in near real-time.

2.2.3 Receiver Clock Accuracy and SUESI Timing Pulse

Historically, CSEM phase data have been much harder to accurately model than amplitude data. These difficulties stem from uncertainties in transmitter timing and receiver clock drift. Higher frequencies are particularly susceptible to timing error since a given timing error projects into a larger phase error as frequency increases. Receiver clocks are GPS-synced prior to deployment and clock drift is measured after recovery. Drift is assumed to be linear between these two points, but any nonlinear component is unknowable under deep sea temperature variations. The Seascan brand clocks in the Vulcan towed receivers are accurate to about 2 ms/day. A 2 ms error would result in an 8° phase shift at 11.5 Hz, the highest frequency used in the Del Mar seep inversions; a phase shift that is comparable to a 15% error in phase that would be problematic to invert when data errors are assumed to be less than 5%.

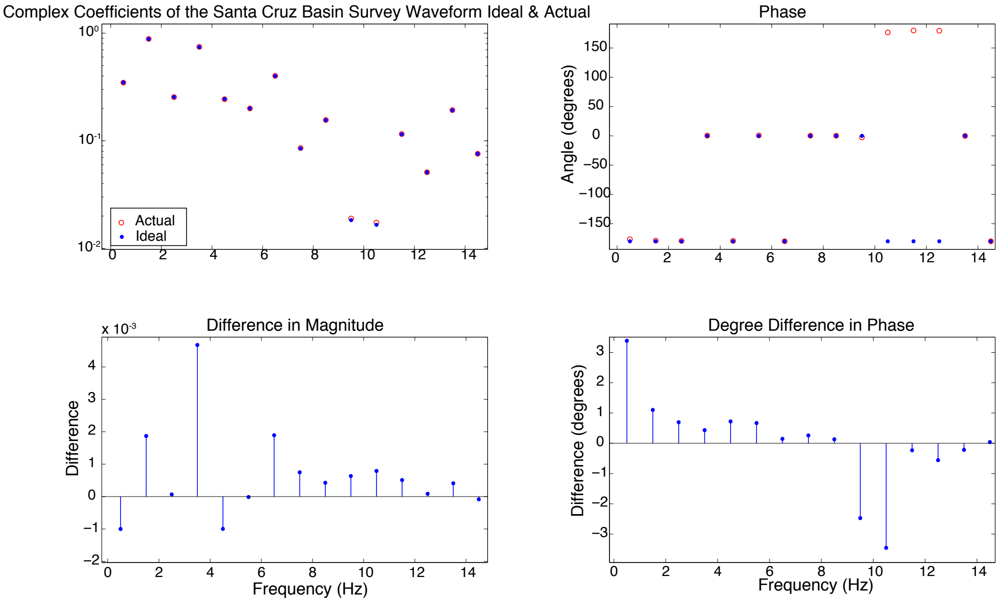

Figure 2.3: Comparison of the ideal waveform-D versus that actually transmitted by SUESI. This also shows the relative power of each frequency when using waveform-D.

SUESI maintains accurate timing using a 400 Hz GPS-locked signal that is used to create the transmitted waveform. Recently improvements to the Vulcans allow this waveform to be sent to the loggers on the spare pair of wires on the Vulcan array tow cable. This waveform can be used to either calibrate the internal Seascan clock, or to directly calculate phase difference between the broadcasted electric field and waveform transmitted down the wire, completely independent of the internal clock. Initial tests have shown that the internal clock can be calibrated to accuracies of ~100 μs, or roughly 0.4° at 11.5 Hz by processing the timing signal with the same code as the CSEM signal and taking the phase difference between the two (Constable et al., 2016). The improved timing has provided accurate phase data, allowing much better data fits (figure 2.4)

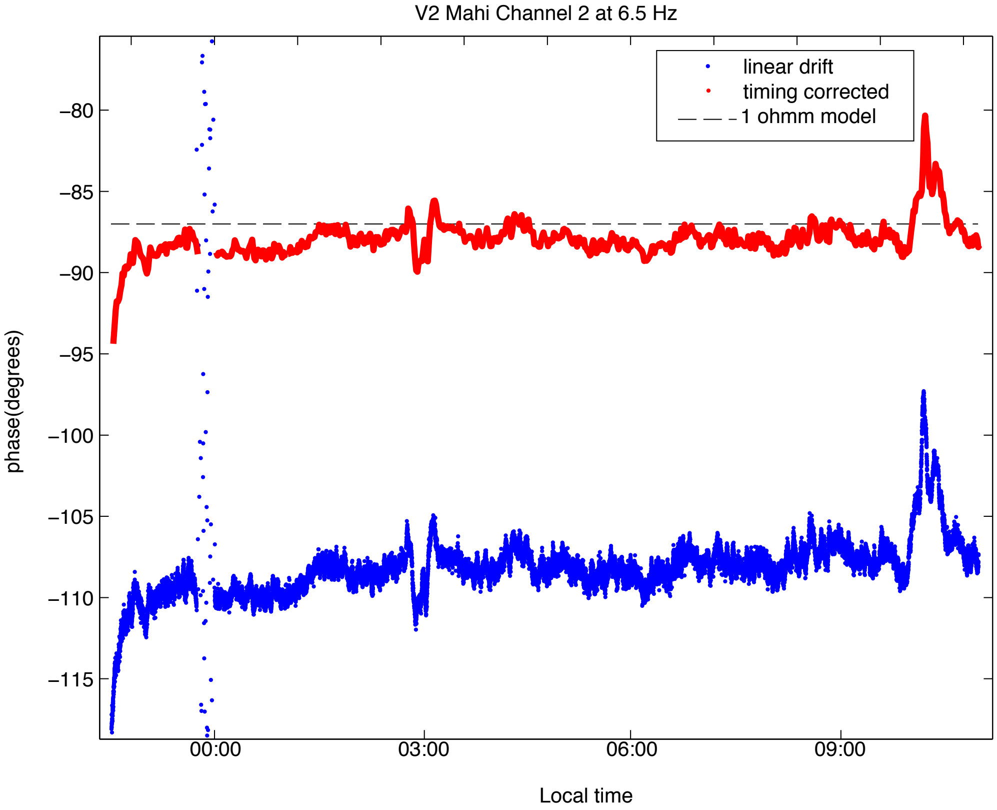

Figure 2.4: Phase data before (blue) and after (red) timing is corrected using the transmitted timing pulse. The dashed line shows the phase response of a 1 Ωm halfspace model, which fits the corrected data. The transmitter was briefly turned off at time 0:00, resulting in random noise.

2.3 Vulcan Receiver Instrumentation

The receiver system used in conjunction with SUESI transmitter is called the Vulcan, a 3-axis electric field receiver that is deep towed behind SUESI at ranges of 250-1500 m (*Figure 2.5*). Vulcan is equipped with 1 m vertical and crossline dipoles on polyethylene wings and a 2 m inline dipole made of spun Kevlar tube tipped with silver-silver chloride electrodes. Rigid receiver dipoles have proven less noisy in the frequency bands we normally transmit (0.5-15 Hz) because flexible cable dipoles are more susceptible to noise as they move through the Earth's magnetic field (Constable et al., 2016).

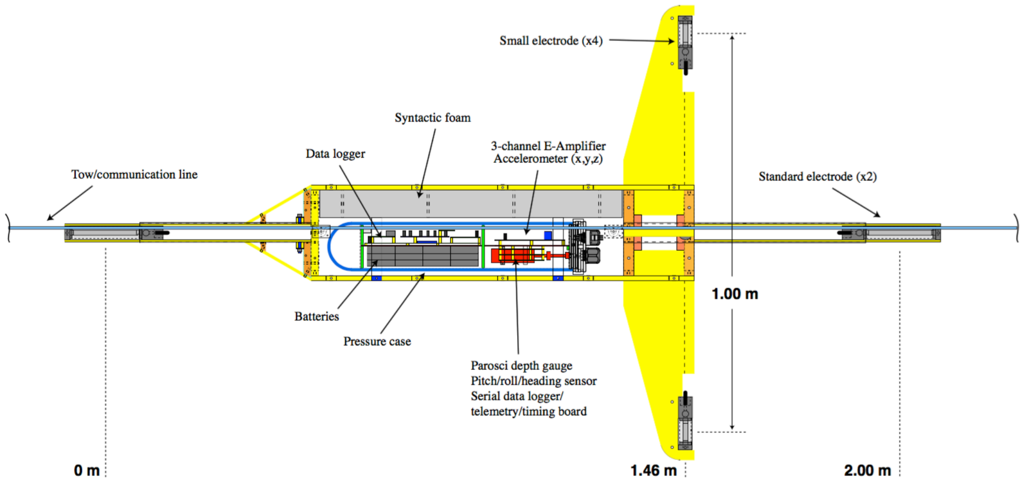

Figure 2.5: Profile of the Vulcan receiver, showing horizontal and vertical dipoles. Inside the Vulcan housing is the data logger and syntactic foam, whose relative placement provides a righting moment.

2.3.1 Vulcan Electronics

The receiver instrumentation is composed of two discrete electronics packages: an electric field logger and a serial data logger (*Figure 2.6*). The electric field logger amplifies, records, and time-stamps the three electric field measurements and three axes of accelerometer measurements. The clock on the logger is accurate to 2 ms/day. These data are recorded on a removable flash card. The serial data logger records and time stamps data from a pressure sensor, a compass and pitch and roll sensor. The serial data logger includes an RS422 driver that allows real-time communication from each Vulcan to SUESI and then up to the deckbox control unit on the ship. The data recorded on the serial data logger are transmitted to the SUESI deckbox every 10-30 seconds, and are recorded locally on internal flash memory every 2 seconds. An electronics pressure vessel is housed in the streamlined high-density polyethylene body of the Vulcan, which is trimmed using a combination of stainless steel weights and syntactic foam to be slightly buoyant in seawater. The arrangement of the foam and weights provides a strong righting moment.

Vulcan amplifier and logger boards

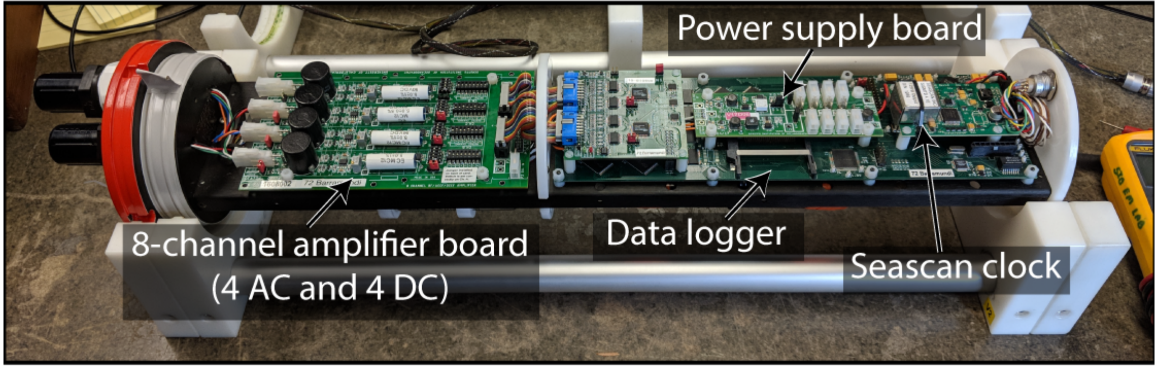

Vulcan serial data logger and batteries

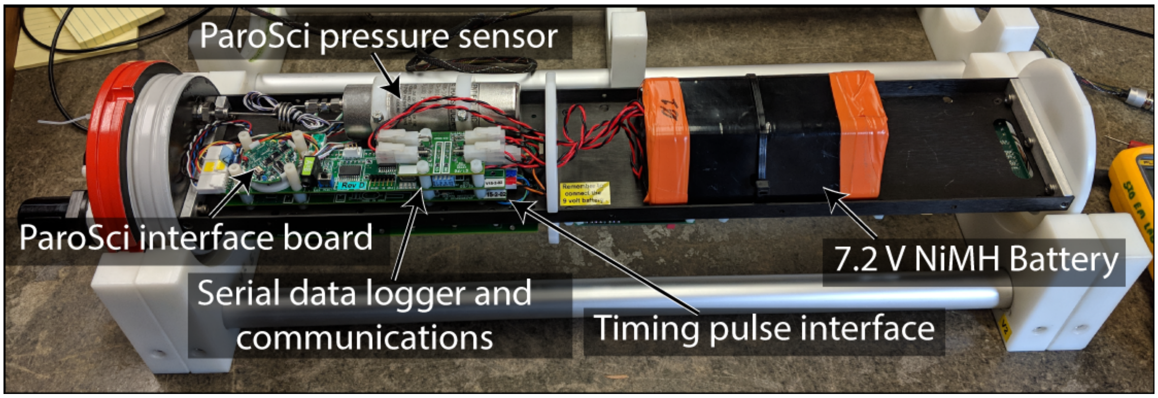

Figure 2.6: Vulcan data logger components.

2.3.2 Vulcan Towed Array

The Vulcans are normally deployed as a string of 4 instruments (Figure 2.7). To accommodate different target depths, multiple cabling setups allow for varying transmitter and receiver offsets. Two common array arrangements are Vulcans placed at either 200, 300, 400, and 500 m or at 450, 650, 850, and 1050 m behind SUESI. Shorter arrays accommodate smaller radius turns and are more responsive to changes in SUESI depth as SUESI is "flown" over bathymetry. Longer arrays are capable of imaging deeper geologic structure. Expected target depth, number of turns and turn radius, and anticipated bathymetry are accounted for when choosing the appropriate array for a survey. The Vulcan array is not limited to 4 receivers, with 6 or more Vulcans capable of simultaneous operation. During deployment the Vulcans can be installed on the array without transferring the load on the line by using split harneses, which attach to the Vulcans with quick release pins (figure 2.8). In practice, the load on the line is small (about 20 kg), with the array capable of being hauled in by one or two people while the ship is moving at up to 3 knots, but is deployed and recovered with a winch. Each Vulcan weighs 25 kg and is handled by two people on deck. The Vulcans are connected to each other and SUESI with a negatively buoyant cable consisting of a Kevlar strength member, polyurethane insulation, and 2 pairs of twisted copper wire. The cable is made neutrally buoyant with small syntactic foam blocks.

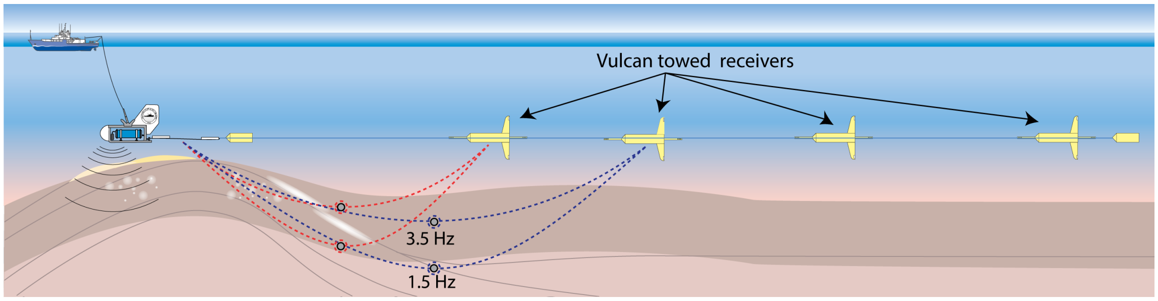

Figure 2.7: Common SUESI and Vulcan tower array configuration. The yellow towfish trailing SUESI is the antenna tail-end transponder (ATET). Another towfish trails behind the Vulcan array, colloquially referred to as the BTET, which houses a 200 kHz altimeter, a pressure sensor, a compass pitch, and roll sensor, and a transponder used for navigation. Blue and red dashed arcs illustrate the increased depth penetration of lower frequencies and longer source-receiver offsets.

Similar to the A-TET, another tail-end transponder (known as the B-TET) sits at the end of the Vulcan array. The B-TET houses an electronics package that contains a pressure sensor, a compass, a pitch and roll sensor, as well as an acoustic transponder. In early Vulcan surveys, the only seafloor reference was from the altimeter on SUESI, with the rest of the array only providing water depth. Recently, an altimeter was added to the B-TET, which allows real-time measurements of the distance above seafloor at the end of the array. This altimeter allows longer arrays to be towed safely, as the geometry of the array with respect to seafloor can be monitored accurately in real time. Knowing real time array geometry is especially important when towing in regions with seafloor infrastructure, such as is prevalent in the Gulf of Mexico.

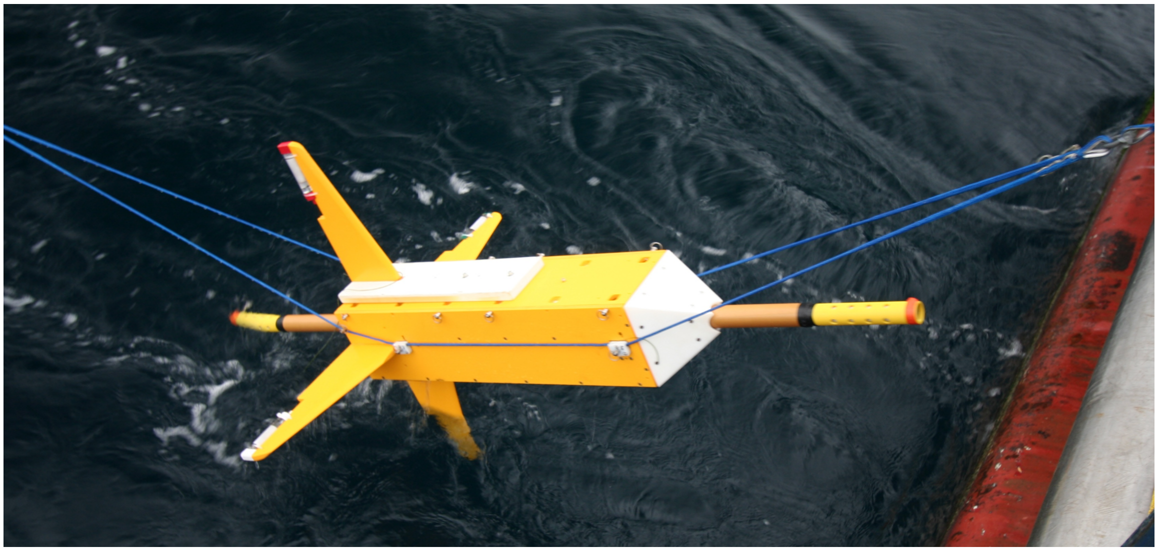

Figure 2.8: A Vulcan receiver being deployed. Note the blue lines which clip to the side of the Vulcan towfish and allow placement of the receiver into the array while under load. Not shown in this picture is the communication cable used for real-time navigation of the array.

The internal compasses on the Vulcans are corrupted by the magnetic field from the nickel-metal hydride battery packs located ~20 cm away in the pressure vessel. To recover orientation, we attach external compasses to the rear “stinger” of the inline dipole. Housed in small pressure cases, the external compasses have a lower sample rate, limited by the internal 9V lithium battery. For a given heading, the offset between the internal, high sample rate corrupted compass and the accurate external compass is constant and can be used to calibrate the internal compass (figure 2.9). The internal compass must be recalibrated after every large heading change, as the interaction of the battery's magnetic field and Earth's magnetic field is not linear.

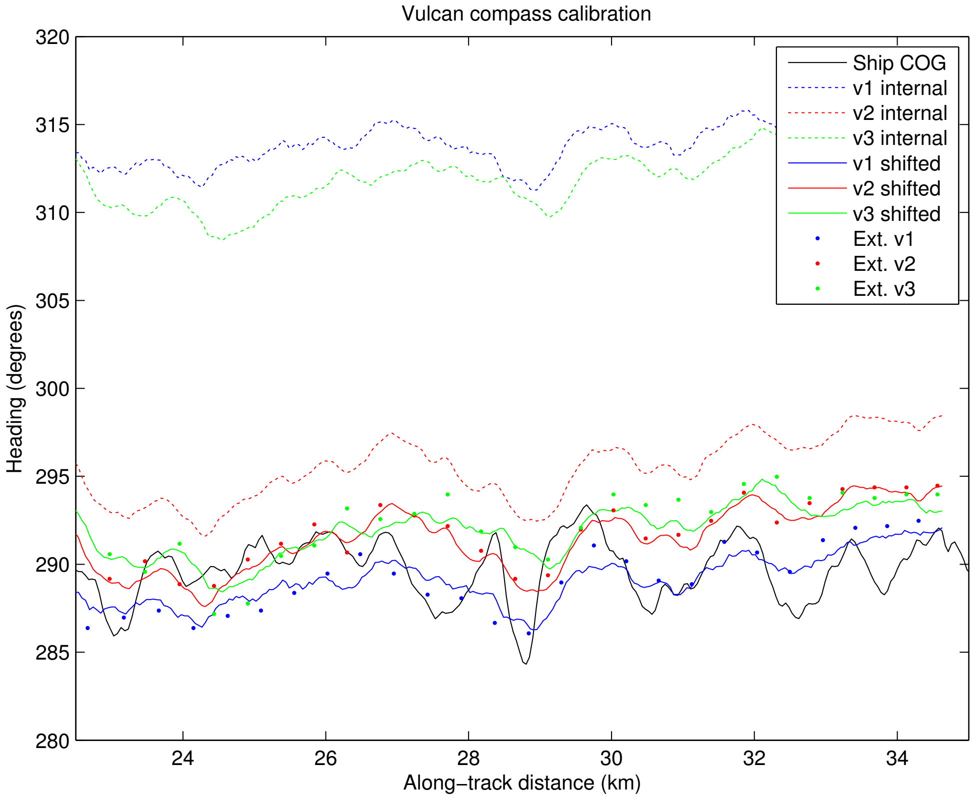

Figure 2.9: Vulcan internal compass (dashed line) corrected using external compass (points). Internal Vulcan compass measurements are corrupted by the magnetic field of the NiMH batteries. For a constant heading, this can be corrected (solid lines) using an external compass strapped to the rear stinger of the Vulcan. Ship course over ground also shown (black line).

2.3.3 Vulcan Array Navigation

Understanding the geometry of the Vulcan array, and where it is in space, is very important during the inversion process. Uncertainties in navigation are often the greatest sources of error in CSEM surveys (Myer et al., 2012). Towed receiver arrays have different navigational requirements and different error structure than traditional seafloor node-based receiver surveys.

The largest source of error in CSEM surveys using seafloor receivers is caused by uncertainties in short range source-receiver offset (Myer at al., 2012). The fixed-offset nature of the Vulcan array precludes range-based sources of error. However, a towed receiver is moving through the water, and has a fluctuating orientation and relative seafloor position, unlike the seafloor receivers. To quantify the total estimated error from navigational parameters for each dipole, a sensitivity analysis of each parameter was performed (Constable et al., 2016) (figure 2.10). Errors in azimuth are range and frequency independent and will only impact the amplitude on the inline dipole, which will decrease with the cosine of azimuth error. Likewise, errors in roll will only affect amplitude on the vertical dipole. Height is typically measured to better than a meter, but overestimation of altitude will lead to underestimating amplitude and phase. This effect increases with range before reaching a frequency dependent threshold that is dictated by skin depth attenuation in seawater. Crossline set is the horizontal distance the receiver has deviated perpendicular to the tow line. Errors in crossline set have a much stronger effect on amplitude than phase, and decrease quickly with increasing source-receiver offset, with higher frequencies exacerbating the effect. Curvature of the array can cause overestimation of source-receiver offset, leading to errors in range. However, a Vulcan receiver was acoustically measured to be within 0.75 m of the expected 1200 m offset, which is at the resolution of the acoustic unit. Vertical dipole error is dominated by pitch, as changes in pitch will cause the larger horizontal field to be coupled into the vertical dipole. Pitch errors in the inline dipole are a function of the relative amplitude and phase of the vertical and horizontal electric fields that change as range increases. At short offsets, the pitch errors in amplitude and phase are negatively correlated, but this changes to a positive correlation as range increases. Seawater conductivity, like all navigation errors other than depth, has a larger effect on amplitude than phase.

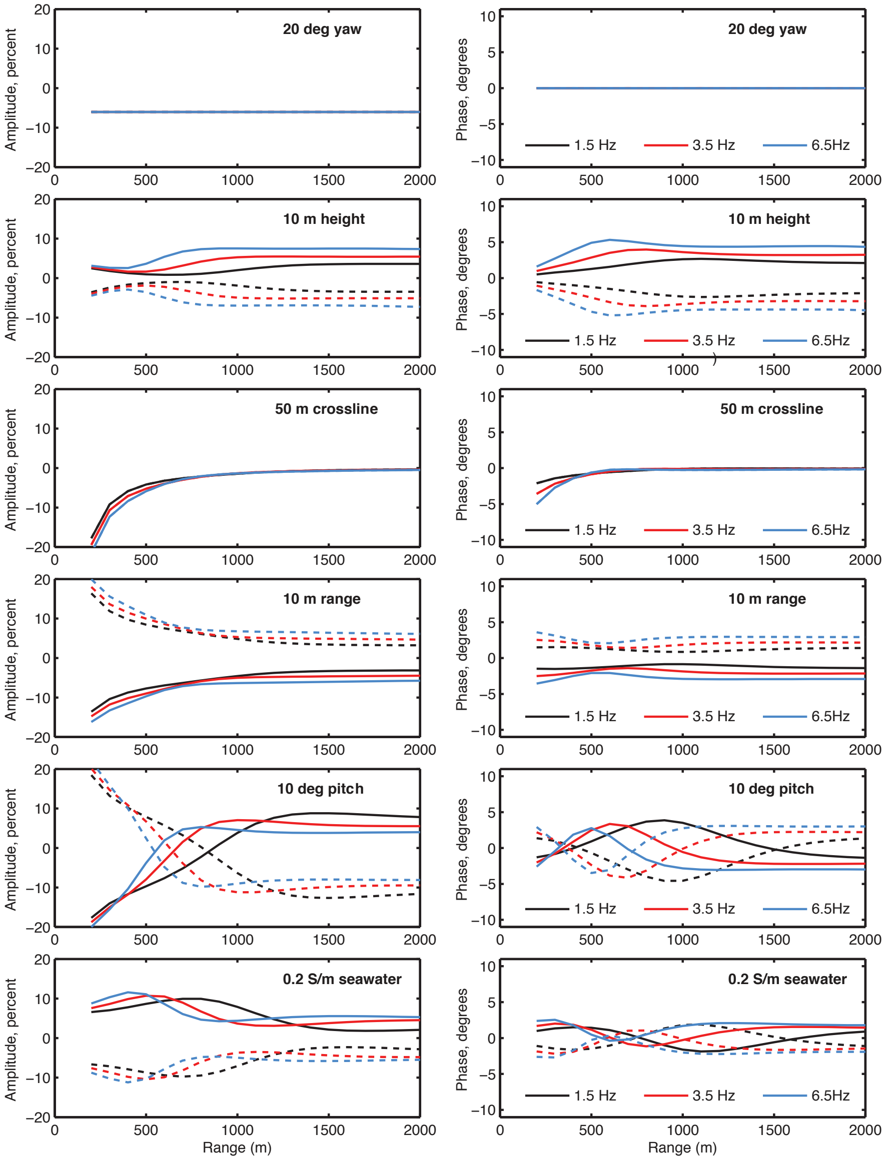

Figure 2.10: Electric field amplitude (left column) and phase (right column) sensitivity to various navigational parameters as a function of distance and frequency in a 1 Ωm halfspace. (From Constable et al., 2016).

Total navigation error for each source receiver offset, frequency, and dipole was calculated using the geometric mean of errors estimated for antenna and receiver azimuth, range, depth, crossline set, pitch, roll, and seawater conductivity (figure 2.10). Total vertical dipole errors are much larger than inline errors, caused by the vertical dipole's sensitivity to pitch. In practice, this is not an issue because the sensitivity of the vertical dipole to resistors, especially vertical resistors, is much greater than the inline dipole sensitivity to those same features. Navigation error estimates, calibrated through sensitivity analyses, and coupled with accurate phase measurements using the SUESI timing pulse described previously, have allowed data fits to better than 1% for inversions of recent survey data. As shown in figure 2.11, estimated errors at a given receiver geometry are dependent on the resistivity of local geology. All inversions use a 1 Ωm starting model, with data error estimates calculated based on this value. However, as the model incorporates resistive structure, the assumptions of the data error estimates are no longer valid, which can result in increased misfit near resistive or conductive features that are typically the target of CSEM surveys. That is, we know the least about the errors associated with part of the model that we care most about. There is currently no mechanism to update the error structure as a function of local model resistivity between inversion iterations, but by simply adding realistic navigation errors to our data error calculation, model misfits have decreased when compared to static error floors.

When inverting a 2D Vulcan profile, all of the survey navigational parameters necessary for inversion can be defined relative to SUESI, making geolocation unnecessary. The altimeter aboard SUESI, coupled with depth sensor, is used to measure the seafloor bathymetry. Ship position and layback can be used to determine SUESI position relative to an arbitrary point on the survey track (e.g. the start of the survey line). The Vulcan receivers are located a fixed distance behind SUESI, with their geometry and depth determined by onboard sensors. Constructing models using a SUESI as a reference allows accurate inversions in surveys where navigational systems (such as those described below) are either inaccurate or absent. However, this method is only useable in 2D profiles. Absolute position is necessary for 3D inversions containing multiple survey lines and off-trackline bathymetry.

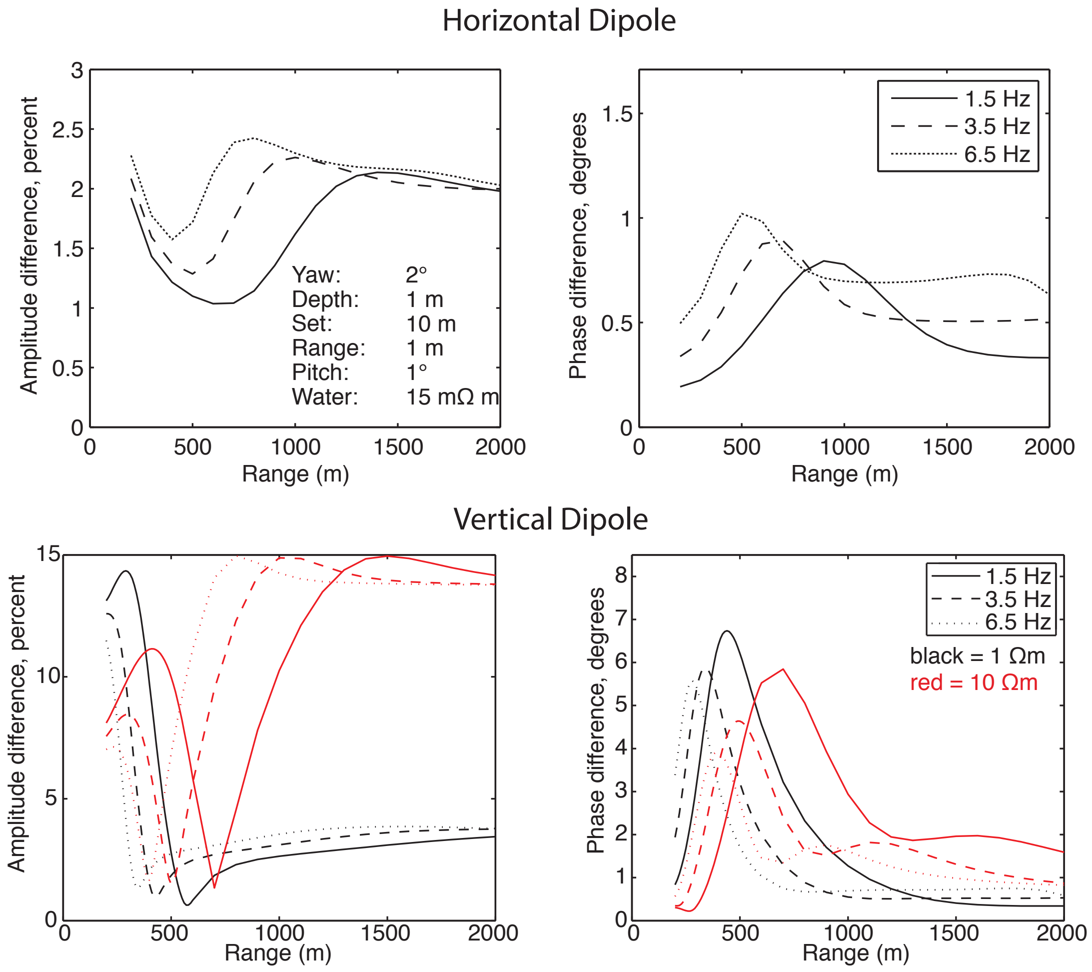

Figure 2.11: Effect of navigation errors from receivers and transmitter geometrically summed for the horizontal (top row) and vertical (bottom row) dipole. The vertical dipole plots also compare the effect navigational errors in a 1 Ωm half space with those in a 10 Ωm half space. (Adapted from Constable et al., 2016)

While absolute locations are not crucial for Vulcan 2D inversions, they are necessary when doing combined Vulcan-seafloor receiver surveys as well as 3D inversions. Additionally, shallow seafloor geology can change over the space of tens of meters, so accurately correlating CSEM results with seismic and borehole data requires good navigational constraints on array location. The Vulcan array can be navigated in a few different ways. The first is by using the “Barracuda” Inverted Long Base Line (ILBL) acoustic positional system. Barracuda consists of three GPS positioned acoustic transponders on the sea surface, one on the ship, and two towed behind the ship. The two towed transponders are towed to the port and starboard with paravane deflectors which maintain an offset of ~300 m (Key et al., 2012). An acoustic unit mounted on SUESI ranges to the baracuda transponders, which along with depth allows SUESI’s position to be triangulated. Relay transponders on the A-TET and B-TET allow their positions also to be calculated. Similarly, a seafloor based LBL system can be used to navigate the towed array. Instead of GPS located transponders on the sea surface, the seafloor system relies on moored transponders that can be ranged on by the towed array. Each moored transponder is acoustically navigated from the ship prior to the Vulcan survey. Lastly, an ultra-short baseline (USBL) ship mounted system can be used to navigate the array. USBL systems can work well, but suffer from drawbacks. They are seldom installed on research vessels. The layback of the SUESI and Vulcan array is often too large for the USBL to range to. To be accurate, USBL systems need careful calibration using deployed seafloor transponders.

2.4 Conclusions

Over the course of multiple expeditions, the Vulcan towed receiver array, coupled with the SUESI transmitter, has successfully imaged gas hydrates in continental slope sediments. Iterative updates to the instrumentation system has led to improved estimation of array geometry, allowing for accurate error models to be constructed, and improving inversions results. Timing errors resulting from clock inaccuracies are not longer a problem with the addition of a timing pulse recorded on each receiver. Accurate timing has permitted phase data to be included in our inversions, doubling the amount of invertible data. Phase and amplitude are sensitive to different sets of electromagnetic effects, so including phase data presents a richer dataset. The capability of this system is demonstrated in inversion results of the Del Mar Seep (Chapter 3) and the Santa Cruz Basin (Chapter 4).

Chapter 3

CSEM Survey of the Del Mar Methane Seep

3.1 Introduction

3.1.1 Geology of the Inner California Borderlands

The Del Mar Seep is located roughly 50 km offshore San Diego, CA, USA, near the northern end of the San Diego Trough, which is part of the Inner California Borderlands. The Inner California Borderlands formed after the Mendocino plate subducted completely under the North American plate, causing the Riviera triple junction to jump southward. The resulting transition from convergent to transform plate boundary caused: the western transverse range to rotate, the outer borderlands to translate offshore, and the Inner California Borderlands to form extensionally (Bohannon and Geist, 1998). This tectonic activity created the basins and ridges that comprise the present day California borderlands. In the late Miocene, the motion of the Pacific plate changed from northwesterly to northerly, causing the San Andreas fault to jump landward (Atwater and Stock, 1998). With most of the plate motion being accommodated by the San Andreas Fault, deformation in the borderlands decreased substantially, and currently accounts for only 20% of the relative plate motion. The basement of the Inner California Borderlands is composed of the Catalina Schist, a blueschist facies similar to the Franciscan complex, overlain by Miocene and younger sediments.

The Del Mar Seep is positioned on a transpressional pop-up structure within the San Diego trough fault zone (Ryan et al., 2012). The San Diego rough fault splits southwest of the structure, and is situated between the northeast principle strand and southwest strand. The seep is expressed as a 10 m high mound situated in the southern flank of the 4 km wide anticline (figure 3.1). Using high resolution AUV multibeam and chirp data, Ryan et al. (2012) found that the mound exhibited rough, pockmarked seafloor that is typically associated with natural methane seeps (Paull et al., 2008, 2011; Kannberg et al. 2013). The north-northeast trending oblong seep mound measures 200 m by 400 m, and is bracketed on either side by lineations interpreted to be dip-slip faults. These faults, and the anticlinal structure of the entire pop-up structure provide a fluid migration pathway and structural trap for methane rich fluids.

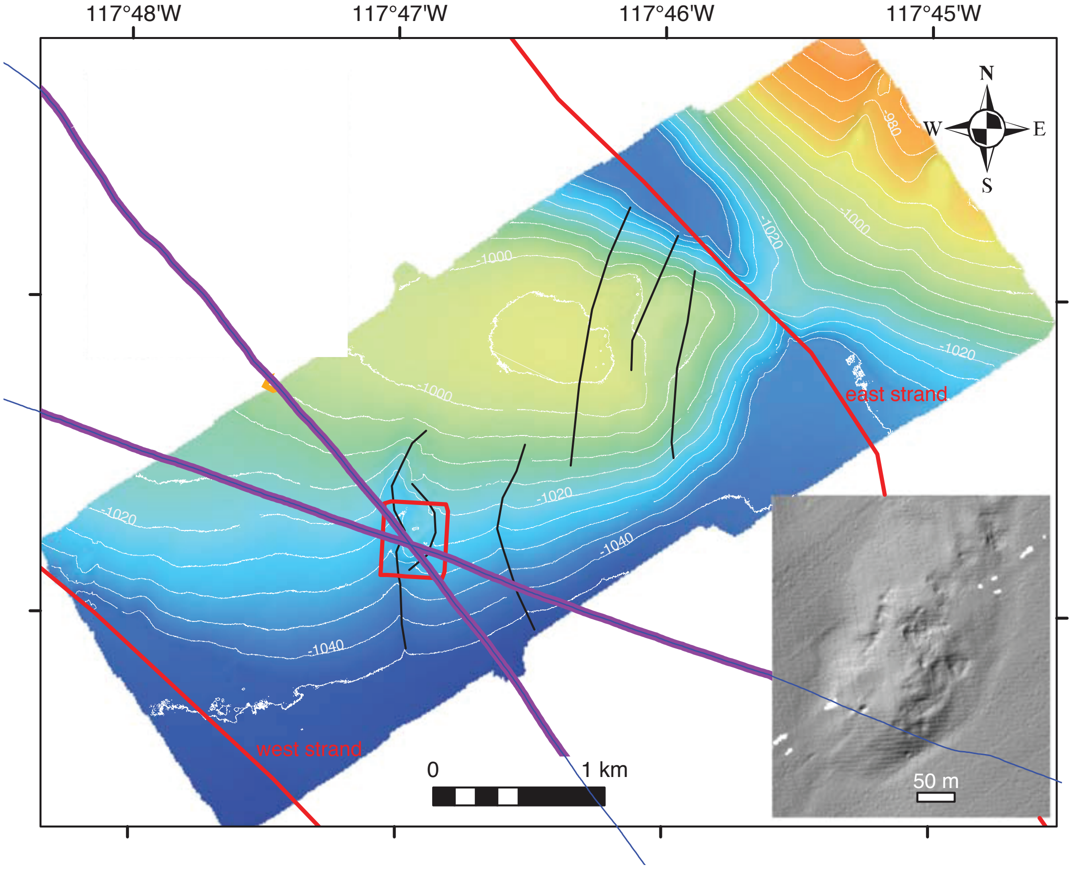

Figure 3.1: Del Mar Seep bathymetry and CSEM survey track lines (purple lines). Red rectangle defines extent of high-resolution bathymetry shown in lower right inset. Pockmarks and rough seafloor texture are common at natural methane seeps. Black lines indicate faults, and the red lines show eastern and western strands of the transpressive San Diego trough fault that creates the pop-up structure. (Figure adapted from Ryan et al., 2012)

3.1.2 Hydrate at the Del Mar Seep

Natural methane seeps are common offshore Southern California (e.g. Hein et al., 2006; Paull et al., 2008; Maloney et al., 2015). The Del Mar Seep exhibits features that currently define natural methane seeps across the globe such as authigenic carbonate crusts formed during methane reduction at the seafloor, pockmarks thought to be related to mass expulsion events, bubble flares imaged on echosounders, blanking in chirp profiles indicating free gas, and increased dissolved methane in water column above the seep (Ryan et al., 2012; Maloney et al., 2015). A $\delta^{13}C$ of −59‰ recovered from push core sediments indicates a biogenic source while the measured δD of −185‰ is associated with thermogenic methane; this discrepancy suggests a mixed system (Whiticar, 1999). Methane-ethane ratio, which may be more instructive of methane source, was not measured. There are no reflection seismic lines present across the seep site, but lines to the north and south show no indication of a BSR. High amplitude reflectors in a seismic line to the north were interpreted to be free gas by Maloney et al. (2015).

Whereas acoustic methods such as reflection seismology are sensitive to sediment velocity, CSEM methods are sensitive to bulk resistivity. Methane hydrate is electrically resistive, and electromagnetic measurements are commonly used to identify and quantify hydrate in well logs (Collett and Ladd, 2000). The resistivity of pure hydrate is 1.2×10^4 Ωm at 10° C, but that resistivity is highly temperature dependent. (Du Frane et al., 2011). A mixed sand and hydrate sample with 45% volume sand and 55% volume hydrate was measured to be 2.5×10^3 Ωm at 10° C (Du Frane et al., 2015). In natural settings, the resistors found in well logs that are interpreted to be hydrate have measured 2 Ωm to 10^4 Ωm (Collett et al., 2008; Lee, 2012; Matsumoto et al., 2017). Hydrate resistivity is dependent on local geologic conditions. Occasionally, small increases in borehole resistivity from background have been interpreted to be hydrate but later discovered to be the result of lithologic changes (Cook and Tost, 2014). Hydrate resistivity is strongly controlled by local geological conditions, such as grain size, sediment type, and pore water conductivity (Spangenberg and Kulenkampff, 2006). Additionally, these geologic conditions, coupled with the other environmental factors (pore fluid methane concentration, fluid flux rates, temperature) will further affect resistivity by influencing hydrate formation type (i.e. disseminated, pore-filling, crack-forming, or nodular) (Spangenberg, 2001).

3.1.3 Prior CSEM surveys of hydrate targets

Edwards (1997) first proposed marine controlled source electromagnetic (CSEM) methods for hydrate exploration. Since then, multiple marine CSEM surveys of hydrates have taken place on continental margins across the world (e.g. Weitemeyer et al., 2006, 2011; Schwalenberg et al., 2010; Goswami et al., 2015). These studies used a number of different instrument systems to electromagnetically image resistive structures beneath the seafloor. Weitemeyer et al. (2006, 2011) towed an electric field transmitter over ocean bottom electromagnetic (OBEM) receivers deployed on the seafloor, while the Goswami et al. (2015) used a towed receiver in addition to OBEMs. Schwalenberg et al. (2010) employed a bottom-towed array, consisting of a transmitter and two receivers, which was towed along the seafloor, stopping every 100-200 m where an electric field was transmitted and recorded for 15 minutes. A deep towed transmitter and receiver array was first used in the Gulf of Mexico, which provided the instrumentation basis for our Del Mar Seep survey (Weitemeyer and Constable, 2010). Each of these studies was able to image resistive structure within the hydrate stability field, interpreted to be methane hydrate.

3.2 Methodology

Our CSEM survey at the Del Mar Seep consists of two crossing lines which intersect at the seep site (purple lines, figure 3.1). The 8 km long line 1 was towed from the southeast to the northwest, with the ship traversing directly over the seep. However, as shown in the bathymetry profile from line 1, the physical expression of the mound at the seep site is absent, suggesting that bottom water current pushed the instrument array either north of south of the central seep site. The CSEM array will be sensitive to structure a couple hundred meters on either side of the array, so resistors underlying the seep will be detectable (Constable, 2010). After crossing the seep, a second 3 km line was towed from the northwest to the southeast, along a more northerly track than line 1. Line 2 crossed more directly over the seep, with the mound apparent in the bathymetry profile used in the inversions.

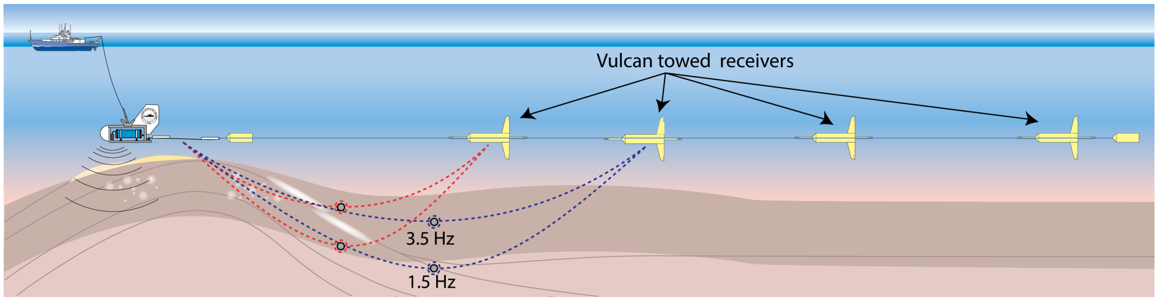

Figure 3.2: General schematic of a CSEM towed Vulcan survey. Deep towed SUESI transmitter tows the antenna and Vulcan receiver array. Depth constraint illustrated by lower frequencies and larger source-receiver offsets penetrating deeper sediments.

3.2.1 CSEM Instrumentation

The CSEM instrumentation used to image the Del Mar Seep consists of an electric field transmitter capable of transmitting 500 A, known as the Scripps undersea electromagnetic source instrument (SUESI) and four 3-axis electric field receivers, known as Vulcans (Figure 3.2) (Constable et al., 2016). SUESI is deep-towed, 50-100m above the seafloor, at 1.5-2 knots and the Vulcans were towed behind SUESI at distances of 200 m, 300 m, 400 m, and 500 m. For hydrate exploration, this system has significant advantages over other systems, as well as some drawbacks. Seafloor receivers are large and heavy, requiring significant deck space and a crane for deployment. Deployment of seafloor receivers is a time-consuming process, as the receivers must be deployed, then navigated to determine where they landed on the seafloor, and then once surveyed, the receivers must be recovered, leaving behind concrete anchors on the seafloor. Towed arrays like the SEUSI-Vulcan system transmit and record continuously, evenly sampling the upper sediments along the survey track, whereas the discrete nature of seafloor receivers results in regions between receivers being less densely sampled. Adequately sampling the upper sediment is especially important when targeting methane hydrate, as it typically exists in the upper few hundred meters of sediment. The fixed nature of OBEMs means that longer source-receiver offsets (3+ km) are possible and therefore will be sensitive to deeper structure than a fixed source-receiver offset. Bottom-towed systems are also time consuming, as data acquisition can only occur when the system is stationary because noise levels are too high when pulling the system along the seafloor. Operating a bottom-towed system near artificial seafloor hazards, such as oil production infrastructure and pipelines, or natural hazards, like the pinnacle at South Hydrate Ridge is not feasible. The 50-100 m tow altitude of the Vulcan array keeps the system well clear of most potential hazards. The bottom-towed system is well coupled to the seafloor, and the transmitted electric field is not as attenuated by the ocean as a transmitter towed above the seafloor. Additionally, the bottom-towed system does not have as much navigational uncertainty as a towed system because depth is fixed to the seafloor, and the increased drag of the receivers along the seafloor ensures that the array hews closely to the transmitter track. Navigational uncertainties of the Vulcan system were quantified by Constable et al. (2016) and improved the inversion process.

Our survey of the Del Mar Seep started as an instrument test, and the close proximity of the seep to the SIO operated Nimitz Marine Facilities provided a convenient target. At the Del Mar Seep, SUESI transmitted the 100 A electric field through a 50 m antenna tipped with copper electrodes, creating a 5×10^4 Am dipole moment. SUESI has an onboard conductivity, depth, temperature, and sound velocity (CTDV) that is used to construct seawater conductivity profiles as SUESI is lowered to depth, necessary for accurate inversions. The seawater sound velocity profiles will provide more accurate navigation if using acoustic methods such as ultra-short baseline (USBL) positioning. An altimeter on SUESI is used to maintain a constant distance above seafloor, which at the Del Mar Seep was 50 m. All of this information is communicated up the tow cable to the shipboard science party in real time. CSEM depth sensitivity is a function of source receiver offset, which is fixed for the Vulcan system, and transmitted frequency, with higher frequencies attenuated more quickly. SUESI can transmit any tertiary waveform, but is typically programmed to transmit a doubly symmetric modified square wave. This waveform, known as waveform-D, was designed to distribute transmitted energy across two decades of frequency, broadening depth sensitivity (Myer et al., 2011).

The Vulcan receiver is a 3-axis electric field receiver with a 2 m inline dipole and

1 m crossline and vertical dipoles that use silver silver-chloride electrodes. Each Vulcan has pressure, pitch, roll, and compass sensors, which are all sent back to the ship in real time to monitor array geometry. Traditional OBEM surveys typically have depth sensitivity of up to ½ source-receiver offset. Depth sensitivity of a towed array can be equal to the source-receiver offset, likely due to the higher data density of towed arrays. Based on the local geothermal gradient, the calculated base of HSZ is 125-150 m below seafloor, well within the 500 m expected depth sensitivity of the Vulcan array. Instrument improvements tested on this cruise included a timing pulse sent from SUESI to the Vulcan receivers that provides more accurate timing than the onboard clocks. Additionally, the Vulcans were programmed to send a subset of the electric field data back to the shipboard operators in real time, which could provide the basis for real time calculations of resistivity pseudosections.

3.2.2 Data Processing

CSEM time-series are processed following the Myer et al. (2011) procedure where Fourier coefficients of receiver time-series are divided by the Fourier coefficients calculated from the transmitted waveform. The complex numbers of that division are normalized by the source-dipole moment and corrected for receiver calibration. The Fourier transform window is defined by the waveform period, and the resulting complex coefficients are stacked over a 60 s period. The resulting stacked values are the same as taking the Fourier coefficients for the entire 60 s period, but allow for calculation of data errors over that time period. In practice, these data errors are much smaller than navigation errors. However, this method of calculating data errors provides a simple method to detect outliers, and allows accurate error estimation used in the inversion process. Stacked complex Fourier coefficients are converted to amplitude and phase for inversion.

3.2.3 Array Navigation and Receiver Timing

At the Del Mar Seep, SUESI and the Vulcan receivers were navigated by calculating the position of the receivers relative to SUESI based on the onboard compass and depth sensors. Uncertainty in transmitter and receiver position and geometry is often the largest source of error, with the greatest error resulting from inaccurate source-receiver offset measurements, but does not affect the fixed-offset Vulcan array (Myer et al., 2012). Constable et al. (2016) quantified the uncertainties associated with the Vulcan towed array, taking into account average errors in transmitter azimuth and altitude above seafloor, receiver azimuth, pitch, roll, and horizontal set, as well as seawater conductivity. The total error is a function of distance from transmitter, frequency, dipole, and geologic resistivity, with geologic resistivity being fixed at 1 Ωm for error calculations used in the inversion process. The error in the vertical dipole is significantly greater than in the horizontal dipole largely due to uncertainty in vertical dipole dip, which will cause the vertical dipole to become more coupled with the stronger horizontal electric fields. Higher vertical dipole error is offset by the vertical dipole's increased sensitivity to resistivity changes in the underlying geology.

CSEM phase data can be more challenging to model accurately than amplitude data because of uncertainties in transmitter timing and receiver clock drift and accuracy. The clocks used in the Vulcan receivers are accurate to 2 ms/day, and in the past the drift has been treated as linear over the course of the receiver deployment. One of the improvements made to the Vulcan array on the Del Mar Seep survey was to send the transmitted waveform directly to the receivers on the telemetry cable, allowing precise timing to be recorded and calibrating the onboard clock. By updating the timing system, onboard clocks are estimated to be accurate to ~100 μs. This is especially important when transmitting a multi-decadal waveform, as a given timing error will project into larger phase errors at higher frequencies. A timing error of 2 ms equates to an 8° phase shift, or 15% error at 11.5 Hz, which was the highest frequency inverted in the Del Mar Seep data. The phase error is reduced to 0.4°, or 0.7% error when using the updated timing system (See Figure 2.4).

3.2.4 Modeling and Inversion

Modeling and inversions were performed using the MARE2DEM modeling code (Key, 2017). MARE2DEM is a finite element electromagnetic modeling program that utilizes the Occam inversion method, which first minimizes the global misfit between the model and data, then finds the smoothest model that fits the data (Constable et al., 1987). The models are parameterized using a bathymetry forming parallelogram mesh that limits the total number of parameters, reducing computation times. MARE2DEM decomposes the parallelograms into finite element triangles, which are adaptively refined until errors resulting from improper meshing are under 1%. At the short source-receiver offsets used in the Del Mar Seep, a finite dipole with 3 integration points is necessary to accurately approximate the source dipole. All inversions are anisotropic with the vertical resistivity allowed to differ from the horizontal resistivity, with the two horizontal resistivities fixed to each other.

All inversions use a starting model with 1 Ωm sediment resistivity half space, and bathymetry calculated by combining SUESI depth and altitude. Seawater resistivity is measured onboard SUESI during descent and ascent at the beginning and end of dives as it traverses the water column. These measured resistivities are binned over 200 m depth windows and added to the starting model as a fixed parameter. Models have 10,000 to 16,000 free parameters, depending on length of survey line and parameter size. All inversions were run on the Triton Shared Compute Cluster, part of the San Diego Supercomputer Center. Inversions typically converged after 5-10 iterations, using roughly 3000 core-hours of compute time in the process.

3.3 Results

Measured at the receiver, electric field amplitude will increase and phase lag will decrease in the presence of resistive geology. Figure 3.3 shows the amplitude and phase at a single frequency for a single Vulcan along line 1. Perturbations in the signal can result from noise in the time series, changes in array geometry, or variations in the resistivity of geology. Both amplitude and phase are largely uniform, with the exception of a large anomaly in the data near the end of the line 1. Comparison of the data to one-dimensional half space models showed that this feature is consistent with a resistive body, however inversions are necessary to resolve absolute resistivity and depth.

Two-dimensional inversions were performed for line 1 incorporating the second, third, and fourth Vulcans. For each Vulcan, amplitude and phase at 1.5 Hz, 3.5 Hz, 6.5 Hz, and 13.5 Hz were inverted for both vertical and inline dipoles, resulting in 9072 inverted data points on line 1. Parallelogram parameter size in the model is 100 m wide by 20 m tall, draped over seafloor bathymetry. Complex data are inverted as amplitude and phase, as opposed to real and imaginary, because navigational errors do not project equally into amplitude and phase. To project navigation errors into real and imaginary components it is necessary to construct a covariance matrix for each value. It is simpler to assign a single error to each amplitude and phase than it is to create a covariance matrix for each real and imaginary value (Myer et al., 2012).

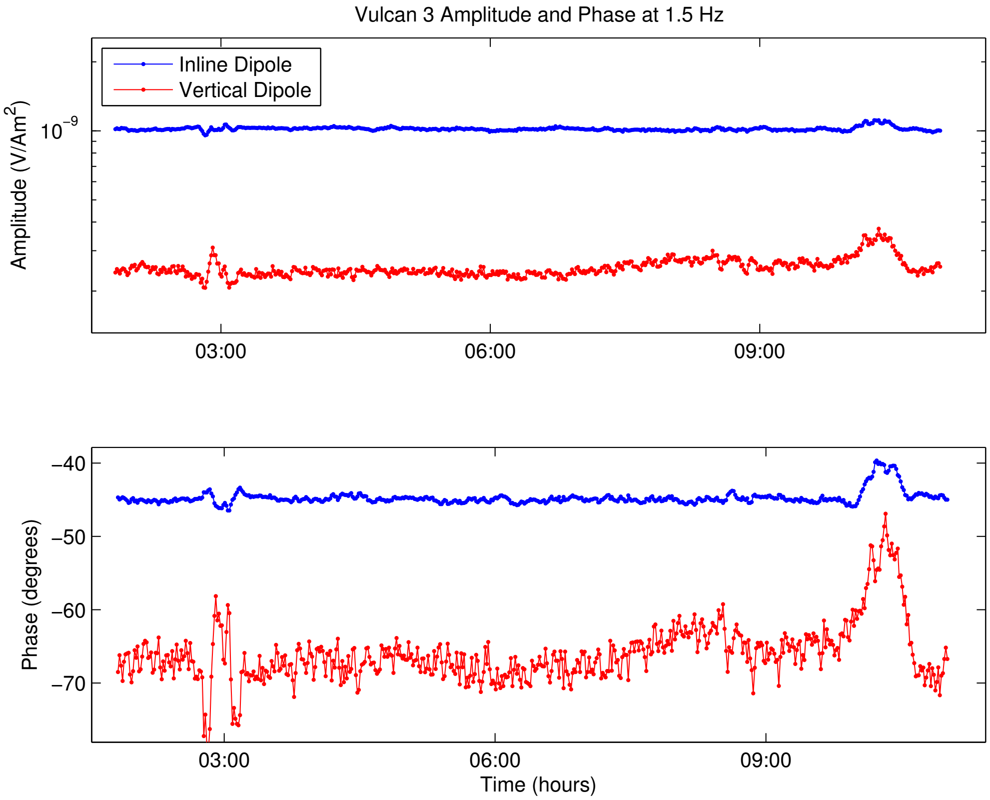

Figure 3.3: Amplitude and phase data for inline and vertical dipoles for line 1 at 1.5 Hz recorded on the third Vulcan. The anomalous response at the end of the line is the signature of the Del Mar Seep.

Data from the first Vulcan, located nearest to the transmitter, did not produce geologically realistic models when included in the inversions. It is unclear why this is the case, but it is possible that the finite dipole approximation did not accurately define the electric field at the source-receiver offset of the first Vulcan. For this reason data from the first Vulcan were not included in any inversions.

3.3.1 Line 1 Inversion

The resulting inversion shows largely uniform sediments throughout the San Diego trough (Figure 3.4). A large resistor is present at the Del Mar Seep, near the northwestern end of line 1. This resistor is ~1 km wide at the base, with a small, ~200 m wide vertical resistor connecting the deeper body to the seafloor. The peak resistivity at the seep is 20 Ωm. Conductive material lies on either side of the vertical seep resistor, and is the focus of modeling discussed later in the text. Another slight conductor underlying the eastern edge of the seep could be the result of advection of warmer, more conductive fluids along faults known to bracket the seep (Ryan et al., 2012). These advective fluids could be tapping the gas rich bodies interpreted by Maloney et al. (2015) and sourcing the seep with methane.

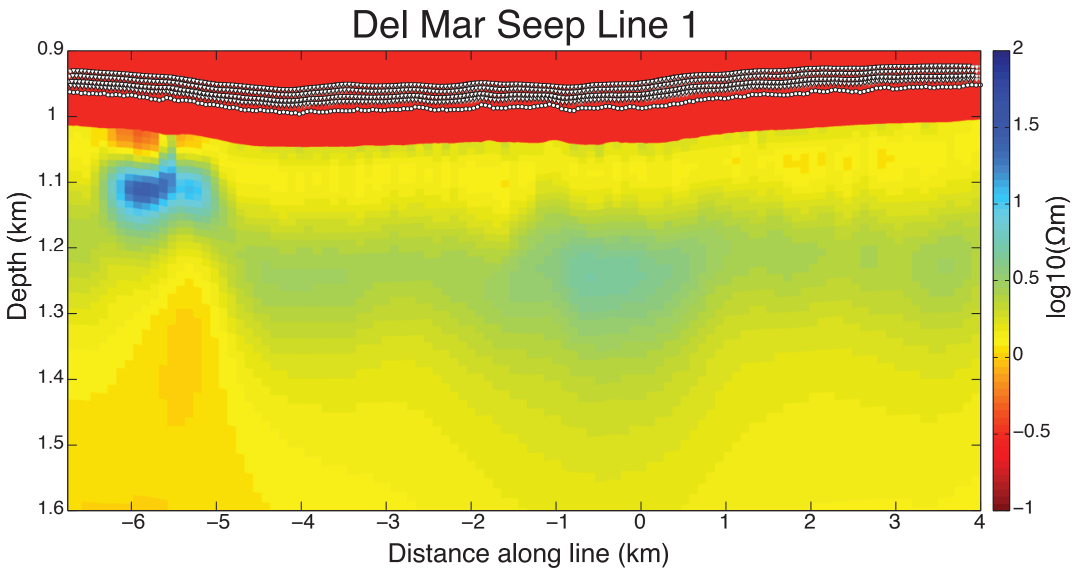

Figure 3.4: Resistivity inversion of line 1. The resistor associated with the Del Mar Seep is present between -6 and -5 km. Academic color scheme showing colder colors as more resistive than warmer colors.

In the center of the trough, at the -1 km mark in figure 3.4, there is a slight change in sediment resistivity. This could be interpreted to be a lithologic change associated with the eastern strand of the San Diego Trough fault. Another interpretation is that the transpressional fault system is compressing the sediment and reducing porosity, which would lead to an increase in bulk resistivity, as exhibited in the inversion result. It is not possible to differentiate between the two hypotheses solely using our results.

Our line 1 inversion model fit the entire dataset to a root mean squared (RMS) error of 0.99 using the error structure described preciously. Data fits for individual components are best across the trough, with misfits generally increasing across the seep (Figure 3.5). While efforts were made to understand and accommodate expected navigational errors, biases in the residuals exist, and are likely the result of unaccounted for, or excessively large, perturbations in the array geometry. These biases are typically small, less than 1 error bar, and across the entire dataset, the average of the residuals is

0.1 (ideally it should be zero). Navigational errors were calculated based on how typical array geometry errors would propagate through a 1 Ωm halfspace. This is likely why our best model fits are typically found in the trough, where the resistivity of the sediment ranges from 1-2 Ωm. However at the seep, the errors calculated for a 1 Ωm halfspace are no longer accurate, so our error structure applied to the data across the seep is likewise inaccurate, resulting in larger errors around the seep. Constable et al. (2016) show that the navigational errors differ by up to 5 percent in amplitude, and 3 degrees in phase, when comparing errors calculated in a 1 Ωm halfspace to those calculated in a 10 Ωm halfspace. A potential solution to this would be to iteratively update the error structure based on prior model resistivity, although this has not yet been implemented.

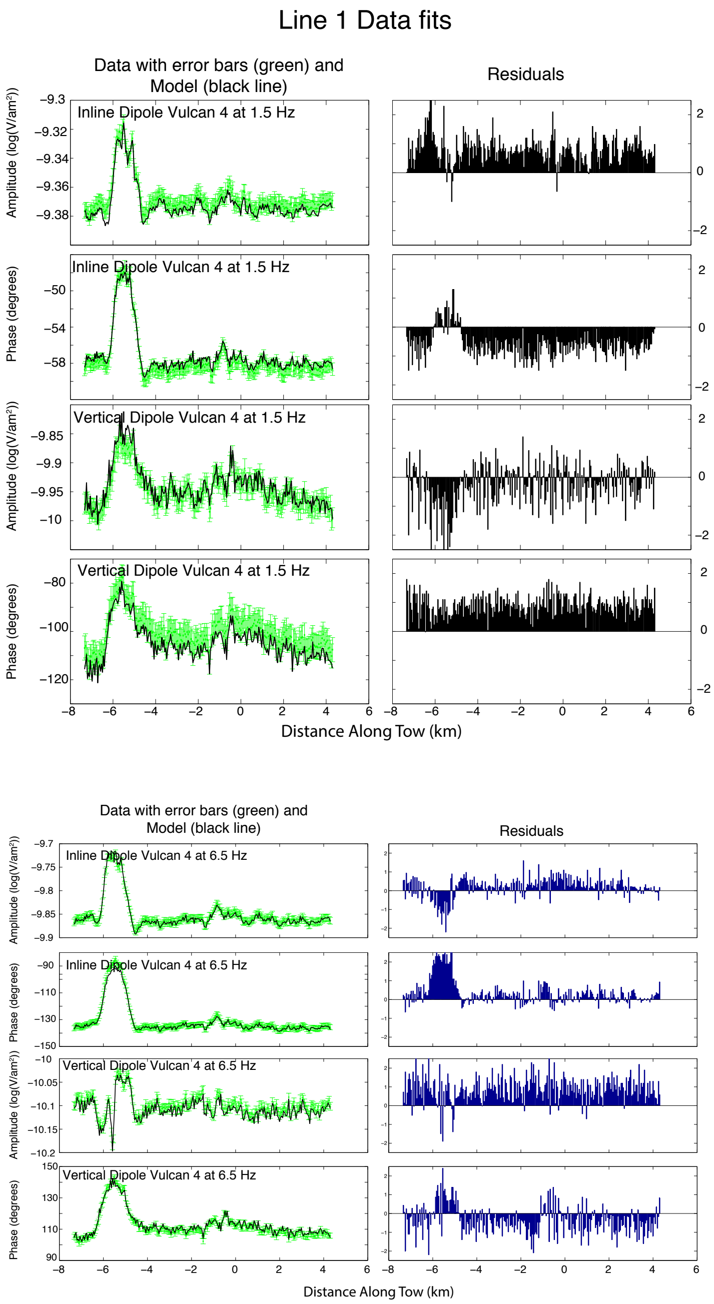

Figure 3.5: Data fits for the inversion shown in figure 3.4. Data with error bars shown in green in left column, with the corresponding model response at black dots. The right column shows residuals between the data and model. Residual biases present are likely the result of navigation errors.

3.3.2 Inversion of Line 1 Focused on the Del Mar Seep

Computational constraints limited the total number of parameters available in a given inversion, which resulted in using 100 m wide by 20 m tall parallelograms in the line 1 inversion. This mesh is too coarse to fully resolve the structure of the seep, so a finer mesh, focused on the seep itself was inverted to better image the resistivity of the central vertical and tabular seep resistors. For the focused inversion, the parallelogram mesh measured 50 m wide by 10 m in height. At standard tow speeds of 2 knots the array will advance 45 m during one 60 s data stacking window, so decreasing the mesh size below this value would only increase computational intensity, without adding any appreciable structure to the resulting inversion.

The focused inversion of the Del Mar Seep has a similar structure to the initial coarse inversion, however the width of the seep can be accurately measured to be 150 m wide, and the underlying tabular resistor is roughly 1100 m wide by 80 m thick at its thickest point (figure 3.6). Resistivity of the seep peaks at 25 Ωm in the tabular resistor, with the resistivity of the vertical structure peaking at 7 Ωm. In the bathymetry profile constructed with the depth and altitude sensors aboard SUESI, the small bathymetric high associated with the seep is not apparent, indicating that we did not traverse directly over the seep, but rather the array was likely pushed by currents to the south or north of the seep.

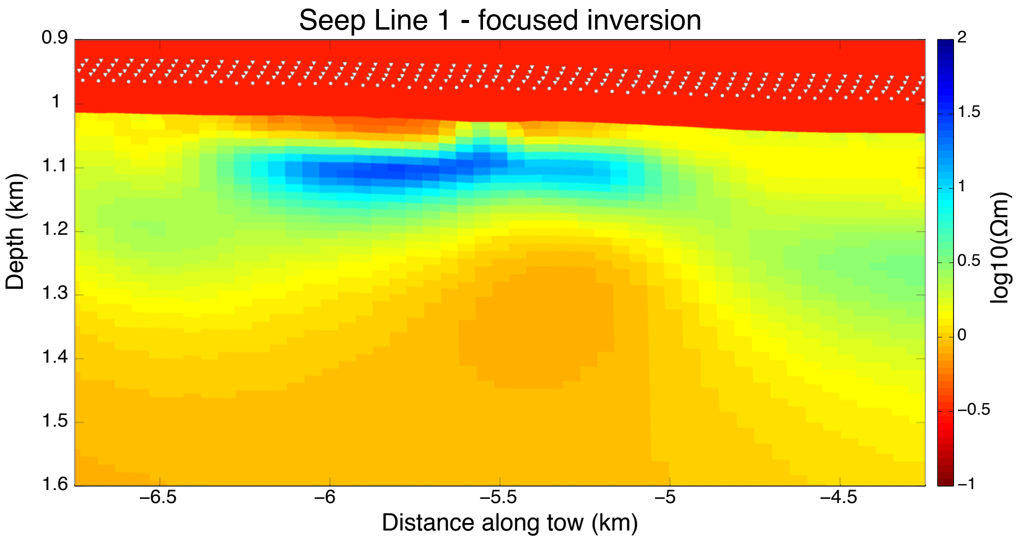

Figure 3.6: Focused inversion of the Del Mar Seep showing vertical resistivity. This model fit the data to an RMS 1.6. The seafloor expression of the seep is located at kilometer -5.5.

3.3.3 Anisotropic Inversion

The MARE2DEM inversion software allows the anisotropic penalty between the vertical and horizontal resistivities to be set by the user (Key, 2016). Lowering the penalty will result in increasingly disparate vertical and horizontal resistivity models. Choosing an appropriate anisotropy penalty is a trial and error process, where multiple penalties are inverted, and the subjectively more geologically realistic model is selected as the preferred model. For the Del Mar Seep inversions, inversions were run at penalties of 1, 0.5, 0.1, 0.05, 0.01, and 0.005. Of these, the vertical and horizontal resistivity models differed very little until penalties smaller than 0.05 were applied. These penalties are much smaller than those typically used for traditional node based CSEM surveys. Higher data densities from towed surveys necessitates much lower, weaker penalties before the models begin to diverge. Here, the inversions were run using an anisotropy penalty of 0.01. The anisotropy of the focused seep inversion of line 1 is show in figure 3.7. The vertical to horizontal anisotropy ratio peaks at 20 while marine sediments typically have an anisotropic ratio of between 1 and 2. Using resistivity well logs, Cook et al. (2010) found that the vertical resistivity can be an order of magnitude or larger than the horizontal resistivity in hydrate bearing sediments. Hydrate preferentially forms in more porous, coarser grained material than in fine-grained sediments. Graded Bouma sequences (Bouma, 1962), such as would be common in the San Diego trough, would have alternating high and low porosity sediments. When filled with hydrate, this would cause alternating high and low resistivity material, resulting in high electrical anisotropy.

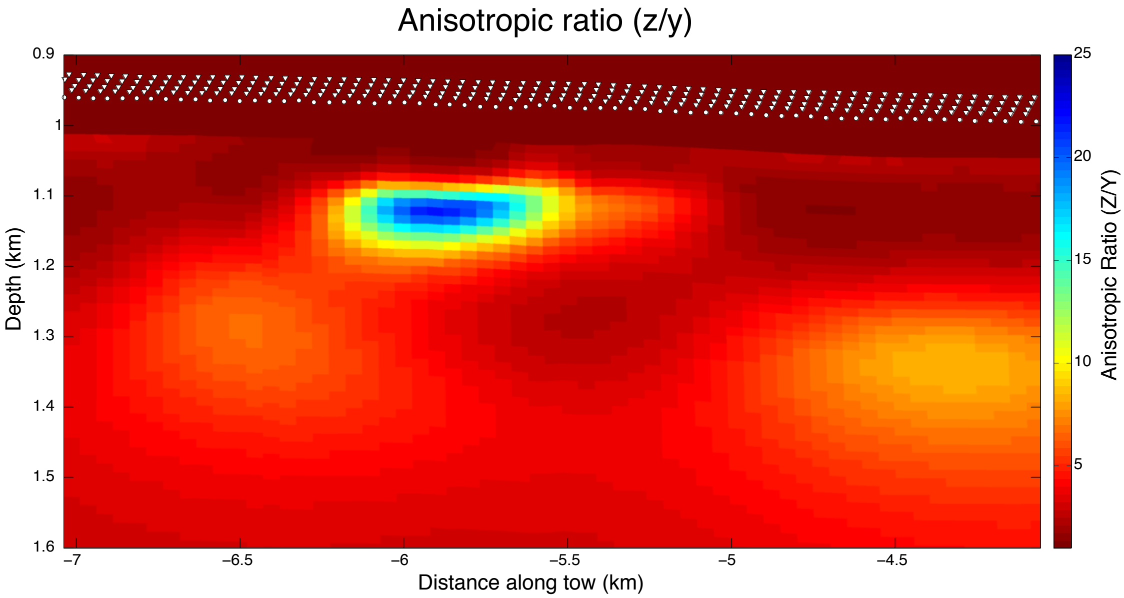

Figure 3.7: Anisotropic ratio (vertical resistivity over horizontal resistivity) of the focused seep inversion shown in figure 3.6. A maximum ratio of 20 is coincident with the highest vertical resistivity in the inversion

3.3.4 Line 2 Inversion

A second survey line was towed across the seep trending more north-south

(Figure 3.1). Line 2 was shorter than line 1 because of time constraints, allowing for a focused inversion of the seep itself. Line 2 inversion model was parameterized the same way as the line 1 focused inversion, with a 50 m by 10 m bathymetry tracking parallelogram mesh, and reached an RMS of 1.5 using the previously discussed error structure. Figure 3.8 shows the resulting inversion, showing strong similarities to the line 1 focused inversion. Unlike line 1, line 2 traversed directly over the seep, and the bathymetry in the inversion shows the bathymetric high of the seep located directly above, and of the same width, as the vertical resistor connecting the underlying tabular resistor to the seafloor. The resistivity of the tabular body peaks at 25 Ωm, just as in line 1. However, the vertical pipe resistivity reaches 17 Ωm, more than double the resistivity at the same point in line 1, and is another indicator that line 2 passed more directly over the seep.

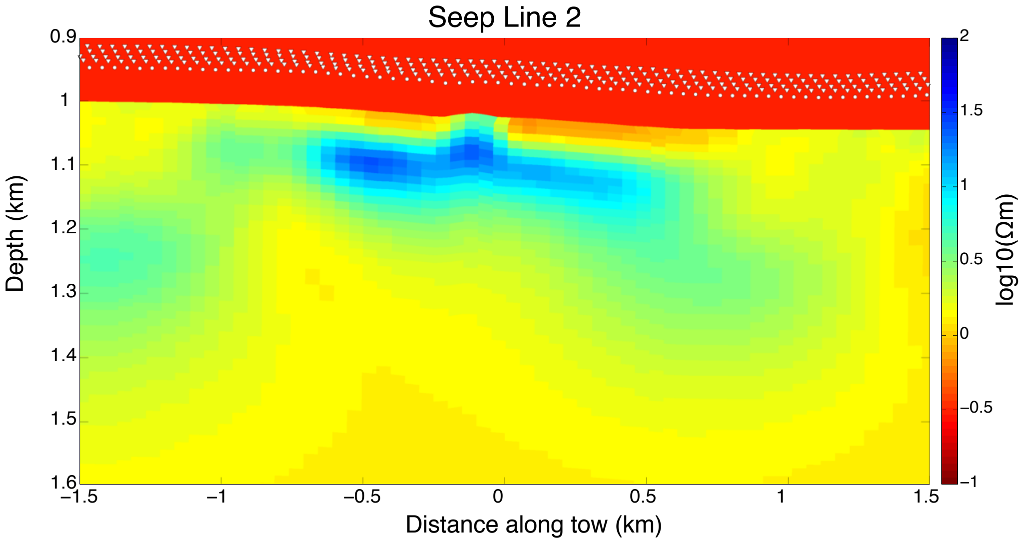

Figure 3.8: Line 2 inversion, focused on the seep. The seep mound is apparent in the bathymetry of this line.

3.4 Discussion

3.4.1 Hydrate saturation and gas in place estimation

Both borehole resistivity measurement and CSEM surveys are sensitive to the increased resistivity resulting from hydrate displacing conductive brine in the sediment pore space. Pearson et al. (1983) first suggested using Archie's law to convert bulk resistivity into hydrate saturation. Archie's law, empirically derived from the resistivity tradeoff of pore fluids composed of either electrically resistive oil and gas or conductive brines in sandstone, states that the pore fluid in a sedimentary system will be the dominant conduction pathway provided everything else (e.g. sediment, free gas, ice, hydrate) is significantly more resistive (Archie, 1942). Archie's equation can be reformed to determine the pore fraction of hydrate as follows:

$$S_h = 1 - \left(\frac{aR_w}{\phi^m R_t}\right)^{\frac{1}{n}} \qquad \text{eq. 3.1}$$

where S_h is the pore space hydrate saturation, a is the tortuosity factor, R_w is the pore fluid resistivity, ϕ is the formation porosity, m is the cementation exponent, R_t is the measured formation resistivity, and n is the saturation exponent (Collett and Ladd, 2000).

By applying the above equation to the resistivity profile of the focused seep inversion of line 1, we can construct a hydrate saturation profile across the Del Mar Seep (figure 3.9). The saturation exponent in eq. 3.1, n, is taken from Cook and Waite (2018), and is calculated based on hydrate-bearing well logs in the Alaskan permafrost and Gulf of Mexico. A cementation exponent (m) of 2.5 was derived by Collett and Ladd (2000) from Blake Ridge sediments. Porosity (ϕ) is taken as 0.5, likely conservative for this depositional environment at these depths, because average porosity of sands at 100 mbsl is 0.5, for silts is 0.7, and clays 0.65 (Bahr et al., 2001). Pore fluids are assumed to be seawater, with a resistivity of 0.3 Ωm. In summary, Archie's parameters used were $n = 2.5$, $m = 2.5$, $\phi = 0.5$, and $R_w = 0.3$ Ωm.

Hydrate saturation derived this way peaks at 67% in the tabular body just northwest of the seep, with average concentrations above 30% across the rest of the seep feature. Archie's law assumes an electrically isotropic medium, which can cause electrical methods to overestimate hydrate concentration in electrically anisotropic environments. Cook et al. (2000) notes that caution should be exercised when applying Archie's equation in environments that are dominated by hydrate filled fractures in near vertical gas chimneys, such as at most natural marine methane seeps. This is not an argument against the CSEM method, but rather an argument against using Archie's law in this situation. Given these limits on the applicability of Archie's law, hydrate saturation calculated using Archie's equation should be considered an upper bound. Laboratory based efforts are ongoing to understand the electrical properties of hydrate bearing sediments with conductive pore fluids (Dufrane et al., 2015, Lu et al., in prep).

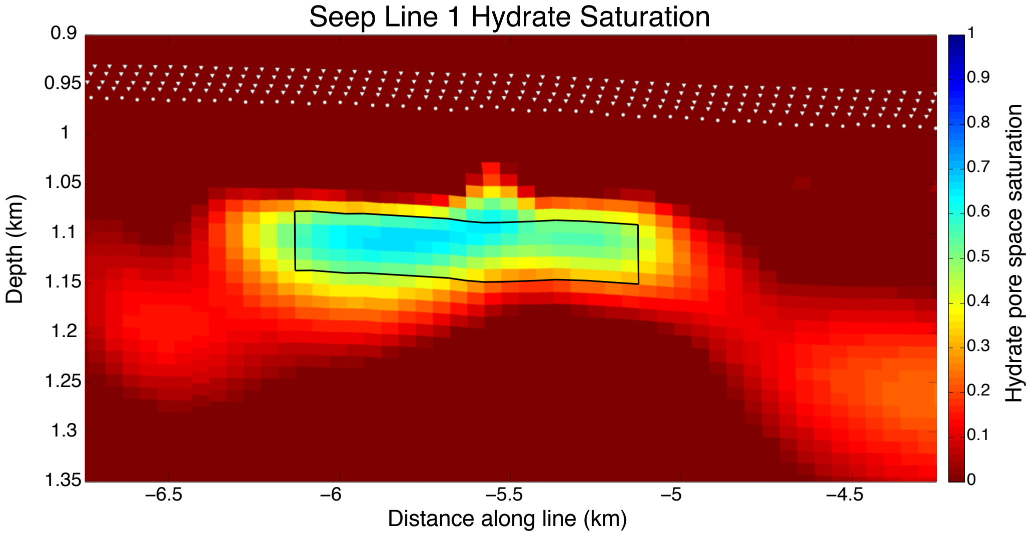

Figure 3.9: Gas hydrate pore space saturation calculated from Archie's equation using the resistivities in the inversion shown in figure 3.6.

Once hydrate saturation is calculated, total gas in place can be estimated. Our two lines cross the seep at a 30° angle, and show remarkably similar resistivity structure. This suggests that the tabular resistor under the seep can be approximated to be a disc. As the hydrate saturation is not symmetric across the seep, the 2D profiles were projected onto to half-discs with different average saturations. Total gas in place at the Del Mar Seep is approximately 2×10^9 m^3 at standard temperature and pressure. To put this in context, the Mount Evans hydrate prospect in the Alaskan permafrost is estimated to hold 17×10^9 m^3 of gas (U.S. Geological Survey Alaska Gas Hydrate Assessment Team, 2013).

3.4.2 Anisotropic Modeling

Anisotropy can be the result of three factors in a material. First, certain minerals are inherently anisotropic, such as graphite. Secondly, structural anisotropy is the result of either alternating layers of isotropically conductive and resistive material whose dimensions small enough to be unresolvable by the given sampling method. Inherent anisotropy is indistinguishable from structural anisotropy, as they both occur on scales below the resolution of the CSEM method. The last form of anisotropy is model induced, where resistive structures within a model alter the model sensitivities to those structures. These altered sensitivities can require the model to be anisotropic to adequately fit the data and be geologically reasonable even when the individual components of the model are isotropic. Synthetic tests were performed to first determine if structural anisotropy is distinguishable from model-induced anisotropy.

Two synthetic models were created, based loosely on the Del Mar Seep, with the models mimicking the wide tabular resistor. The first model has a 50 m tall by 1 km wide isotropic resistor with a resistivity of 10 Ωm in an isotropic 1 Ωm halfpace. This model represents homogenous methane hydrate saturation in a single lithology, and any anisotropy in this model will be the result of model-induced anisotropy. The second model is constructed of a stack of 5, 5 m tall by 1 km wide layers representing alternating fine and coarse-grained lithologic units where the hydrate is present in the coarse material. To keep the resistivity thickness product equivalent in the two models, the thin resistive layers are given a resistivity of 20 Ωm. This stacked layer model will have both structural and model anisotropy, as the resistive layers are individually unresolvable using CSEM. Synthetic data were calculated, and 2% Gaussian errors were added to the data. These data were then inverted with an anisotropic ratio of 0.01. Figure 3.10 shows that the two models are indistinguishable. Model anisotropy dominates the models, with nearly identical vertical resistivity and anisotropic ratios in the two models. There is a small difference in the underlying conductive artifact in the two models, with the stronger artifact present in the homogenous model, though this difference is unlikely to be meaningful when applied to a genuine inversion. These models show that CSEM is unlikely to be able to delineate between massive and interbedded hydrate. However, it may be still be possible if using a high frequency broadside data and 3D inversion methods.

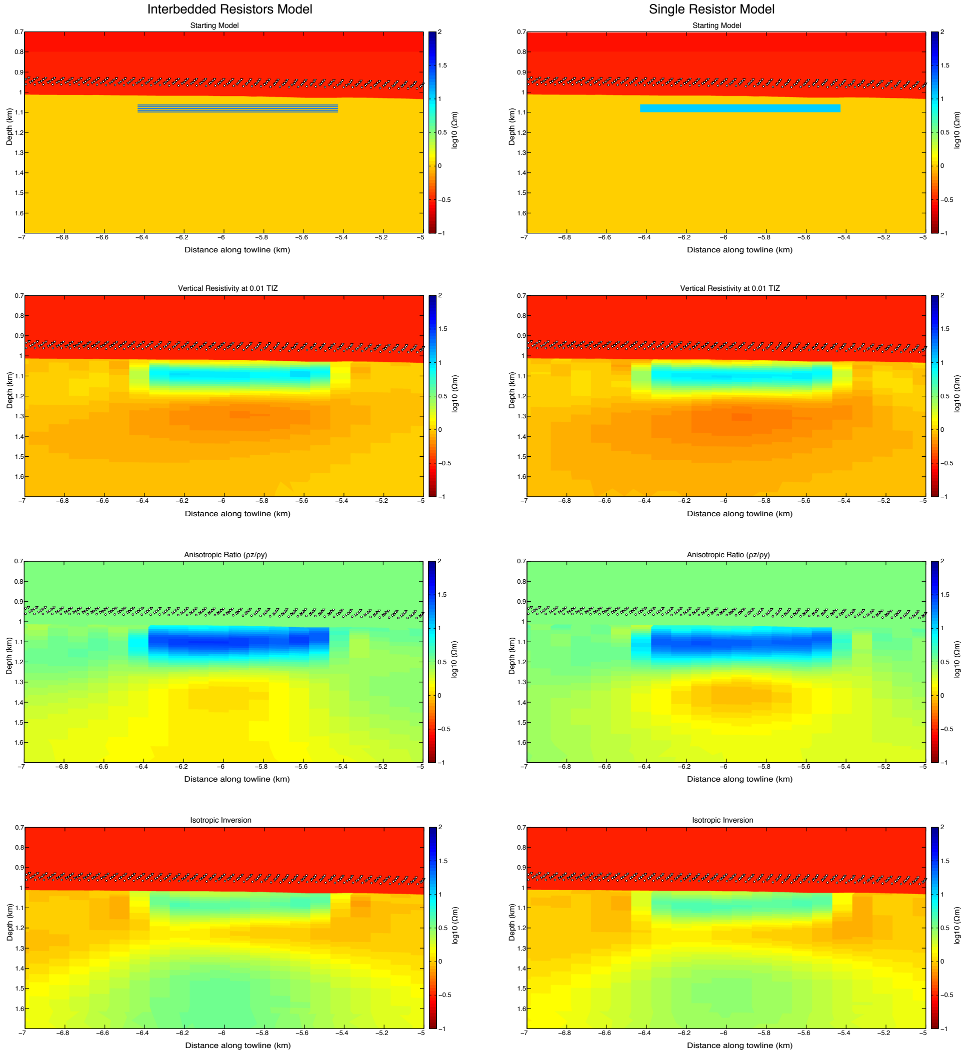

Figure 3.10: Two models meant to mimic the Del Mar Seep, one composed of stacked resistors representing interbedded hydrate, and one a solid resistor representing hydrate partially saturating a thick sand body, were indistinguishable using the CSEM method. Inversions of both models accurately captured the resistivity thickness product of the original resistor. Note that even though the starting model in both cases was isotropic, an anisotropic inversion better replicates the starting model.

3.4.3 Geomorphological context of the Del Mar Seep

The exact age of the Del Mar Seep is unknown, but the geomorphology suggests that is a relatively young seep (Paull et al., 2015). Paull et al. (2015) show that many of the seeps along the western US border are of a similar size, with similar distinctive features. One such feature is the 100-200 m wide seep mound, the top of which is 10-50 m proud of the seafloor. Our results suggest that the surface expression of the Del Mar Seep is similar to these other seeps, and that the deeper hydrated region of the seep is on the order of a kilometer wide. More mature seeps, such as the pinnacle at southern Hydrate Ridge, are found to be of a similar scale. The pinnacle is a 50 m tall carbonate structure rising near the summit of Hydrate Ridge. Surrounding the pinnacle is an 800 m diameter depression, where the seafloor is composed of large carbonate blocks. The bathymetric profile across the pinnacle of hydrate is similar in shape to the upper edge of the resistor imaged at the Del Mar Seep. The Del Mar Seep could be analogous to what the pinnacle at southern Hydrate Ridge looked like when it started. Increased hydrate and authigenic carbonate formation can lead to cementing sediment pore throats, inhibiting methane flux, which force fluid flow to the periphery of hydrated and cemented region. Teichert et al. (2003) showed that authigenic carbonates at the summit of southern Hydrate Ridge were younger than those of the pinnacle, suggesting that the methane flux has migrated from the pinnacle to the summit. At southern Hydrate Ridge, the majority of the venting is now occurring at the summit of the ridge (Philip et al., 2016), 500 m to the east of the pinnacle, the same as the radius of the resistor at the Del Mar Seep. The resistive hydrate body imaged at the Del Mar Seep could be an intermediate stage in the evolution of natural methane seeps. The width of the tabular body at the Del Mar Seep could be at a natural limit, at which point the seep itself will migrate to the periphery of the tabular body, where the increased porosity is more accommodating of fluid flow, as it has a southern Hydrate Ridge. Other older seeps, such as northern Hydrate Ridge, could have followed a similar process; the end result at which is multiple migrations with multiple active seeps. This process is also going to be dependent on local geologic factors, such as faulting.

5. Conclusions

The use of CSEM is a robust method for detecting methane hydrate in marine sediments such as at the Del Mar Seep.

- Advances in our acquisition system, including GPS-synced receiver timing on deep towed receivers, improves accuracy, particularly in phase data.
- High quality data acquisition, coupled with an accurate error model provide robust inversion results.
- A 25 Ωm resistor coincident with the Del Mar methane seep is interpreted to be methane hydrate. This resistor consists of a kilometer wide resistor 50 m thick located 50 mbsf with a 200 m wide vertical resistor rising from the center that extends to the seafloor. This vertical resistor is collocated with the surface expression of the seep.

- Multiple lines across the Del Mar Seep show very similar resistivity structures.
- San Diego trough seafloor resistivity is typical of marine sediments, and exhibits little variation.
- Using Archie's law, total gas in place is estimated to be 2×10^9 m^3.
- Anisotropic inversions are necessary to fit the data. However, anisotropy cannot be used to differentiate between interbedded and massive hydrate formations.
- Seep geomorphology appears to be controlled by subsurface structures imaged using CSEM at the Del Mar Seep.

Chapter 4

Methane Hydrates in the Santa Cruz Basin

4.1 Abstract

Methane hydrate, an ice-like clathrate of water and methane, forms in shallow continental slope sediments, and is both a potential energy source and geologic hazard. Hydrates presence is traditionally inferred from the presence of the bottom simulating reflector (BSR), a seismic velocity inversion resulting from free gas pooling at the base of the hydrate stability field. The BSR is not a measure of hydrate, but rather a proxy for free gas presence. Whereas seismic methods are sensitive to velocity anomalies, controlled-source electromagnetic (CSEM) methods are sensitive to conductivity anomalies. The electrically resistive methane hydrate makes a favorable target for CSEM surveys, which are capable of detecting and potentially quantifying the presence of

methane hydrate directly. We present results from a 6-day June 2014 survey in the Santa Cruz Basin, located in the Outer California Borderlands 100km west of Los Angeles.

CSEM surveys are performed by deep-towing an electromagnetic source that is transmitting a known signal; this signal is detected by receivers towed behind the transmitter. The towed CSEM array used in the Santa Cruz Basin was composed of an electric field transmitter ("SUESI") and 4 "Vulcan" 3-axis electric field receivers. The initial EM source signal is altered by the electrical properties of the surrounding environment. Conductors such as brine and seawater are attenuating mediums, while resistors such as methane hydrate, gas, and oil are preservative of the original signal.

Using 30-year-old 2D seismic profiles as a guide, potential hydrate targets were identified, and the transmitter and array were towed over 150 km on 6 lines with 5 seafloor receivers each. The 6 towed lines were coincident with legacy seismic lines. The towed array is sensitive to sediment depths less than 1km, allowing for high data density through the hydrate stability field. Joint interpretation of CSEM and seismic data sets provides structural detail from the seismic data, and pore-fluid information from the CSEM data. Identified in the Santa Cruz Basin are extensive hydrate deposits, predominantly on basin flanks, where they are coincident with gas migration pathways such as faults and anticlines. Additionally, two methane seeps are identified on the southeastern flank of the basin.

4.2 Introduction

4.2.1 Gas Hydrate Molecular Structures

Synthesis of methane hydrate is predicated upon the presence of gas, water, and appropriate environmental conditions. Temperature, pressure, salinity and guest molecule type combine to define the hydrate stability curve, which in turn is used to identify if hydrates will be present in a given environment. To properly define the hydrate stability curve, it is necessary to understand the local supply of guest molecules. Methane is typically supplied through microbially mediated methanogenic decomposition of organic carbon in the sediments. In such a case, the resulting hydrate will be composed of almost entirely methane, and the carbon and hydrogen atoms will have an isotopically light biogenic signature. Hydrate composed of only methane and other small guest molecules is known as structure I hydrate. Higher order hydrocarbons such as ethane and butane can also form hydrate, however the lattice structure will change shape in order to accommodate these larger guest molecules, forming structure II hydrate. Incorporation of these larger molecules into the hydrate matrix stabilizes the hydrate, allowing it to exist beyond the methane-only stability zone. These higher order hydrocarbons are formed thermogenically at greater depths and higher temperatures and are isotopically heavier than biogenically formed hydrocarbons. Clumped isotope analysis can be used to determine molecular formation temperatures (Stolper et al., 2014).

4.2.2 Geology of the Outer California Borderlands

The Outer Borderlands are located in the Southern California Bight and comprise a series of north-south trending basins bracketed by islands and bathymetric highs. This study focuses on the Santa Cruz Basin, one of two major basins in the Outer Borderlands (Figure 4.1). The geology and geomorphology of the borderlands is the result of tectonic evolution that began 30 Ma in the late Oligocene (Nicholson et al., 1994). Prior to this, the Outer Borderlands and Western Transverse Range were part of the Great Valley, consisting of Cretaceous and Paleocene fore-arc sediments overlying an ophiolotic basement (Miller 2002). At 30 Ma, the remaining Farallon microplates offshore southern California subducted under the North American plate, causing the Rivera triple junction to migrate to the southeast. This migration resulted first in the clockwise rotation of the Western Transverse Range and the westward translation of the Outer Borderlands. The Outer Borderlands underwent relatively minor deformation during this process, with the original ophiolotic basement and Cretaceous-Paleocene sediments still present (Bohannon and Geist, 1998). At the time, the Rivera triple junction was a ridge-transform-transform boundary, which as the triple junction migrated southward and eastward underneath the Outer Borderlands resulted in volcanism that is preserved as Miocene basalts (Schindler, 2010). These basalts are not continuous, and their presence is not identifiable in 2D reflection seismic data in the area (Bohannon and Geist, 1998). During translation of the Outer Borderlands, the fore-arc sediments at or near the sea-surface were partially eroded, and have since subsided up to 4 km (Schindler, 2010). The subsidence and formation of the basins was likely the result of exhumation and flow of lower-crustal material into the inner borderlands, causing a thinning of the Outer Borderlands crust.

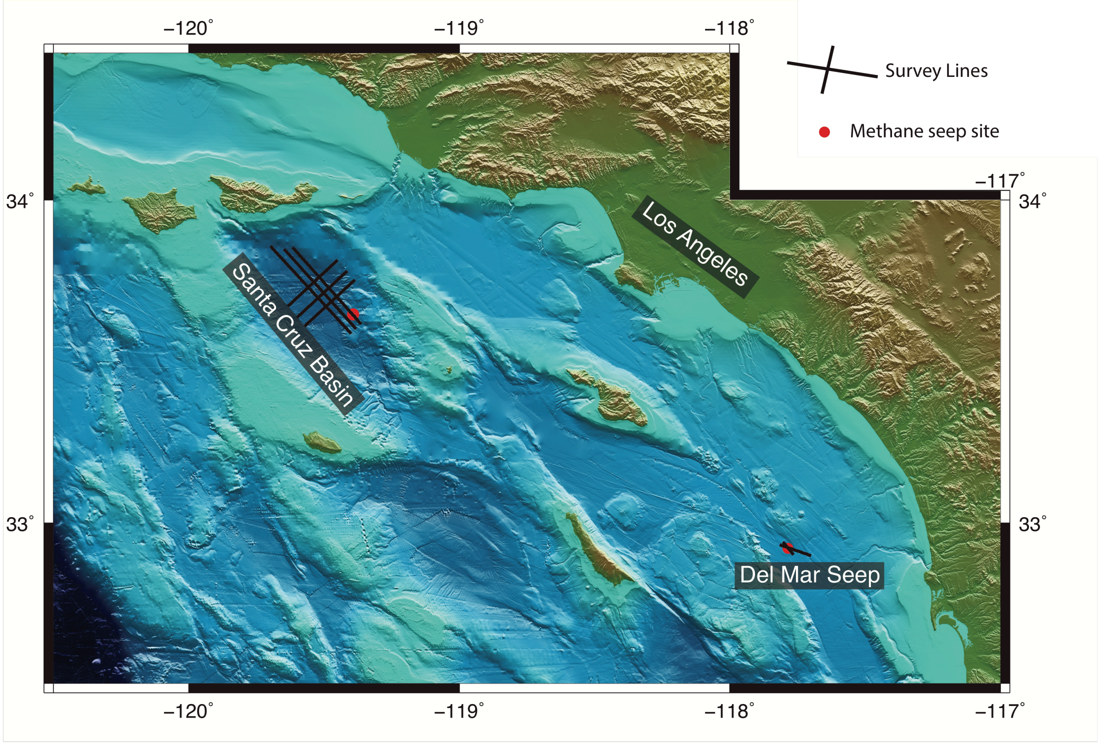

Figure 4.1: Map of the California Borderlands showing survey lines at the Santa Cruz Basin and at the Del Mar Seep (Chapter 3). Survey lines are black lines, and inferred methane seep sites are red circles.

4.2.3 Hydrocarbon Potential in the Outer California Borderlands

Unlike the inner borderlands, where sediments are relatively thin and young, the Outer Borderlands have old, and in some areas thick, sediment cover. This disparity in sedimentation histories controls the source and composition of hydrate forming gas. While gas in inner borderlands is biogenic, and therefore almost exclusively methane, the great valley sedimentary sequence present in the Outer Borderlands sediments has a history of producing thermogenic hydrocarbons (Victor, 1997; Piper and Ojukwu, 2014). Prior to the breakup of the Western Transverse Range, Outer Borderlands, and formation of the inner borderlands, the Western Transverse Range, Outer Borderlands, and Great Valley were aligned in the same depositional setting (Atwater, 1998). Figure 4.2 shows the current gas and oil reservoirs in California, as well as a reconstruction of the tectonic placement of the Great Valley, Western Transverse Range, and Outer Borderlands illustrating the petrologic connection between the three areas. These petroleum systems could source the methane and higher hydrocarbons necessary for sI and sII hydrate formation in the Santa Cruz Basin.

The Santa Cruz Basin is a northwest trending basin surrounded by Santa Cruz Island to the north, the Santa Cruz-Catalina Ridge to the west, San Nicolas Island to the south, and to the west by an unnamed ridge that separates the Santa Cruz Basin from the Santa Rosa Basin. Santa Cruz Basin is roughly 80 km in length by 40 km wide, with water depths up to 1900 m. The basin is bounded to the east and north by the East Santa Cruz Basin fault, a series of reactivated oblique reverse faults (Schindler, 2010) which is thought to be the lithologic boundary between the metamorphic core complex Catalina terrain of the inner borderlands and the Great Valley sediments and Great Valley ophiolite of the Nicolas terrain in the Outer Borderlands (Bohannon and Geist, 1998, ten Brink et al., 2000; Miller, 2002). However, recent seismic analyses by Schindler (2010) found evidence of Nicolas terrain east of the East Santa Cruz Basin fault system, suggesting that the lithologic transition from Nicolas to Catalina terrain is located further east. While not recognized as an active fault system by the USGS, a magnitude 5.3 earthquake occurred on this fault on April 5, 2018 (Patton, 2018).

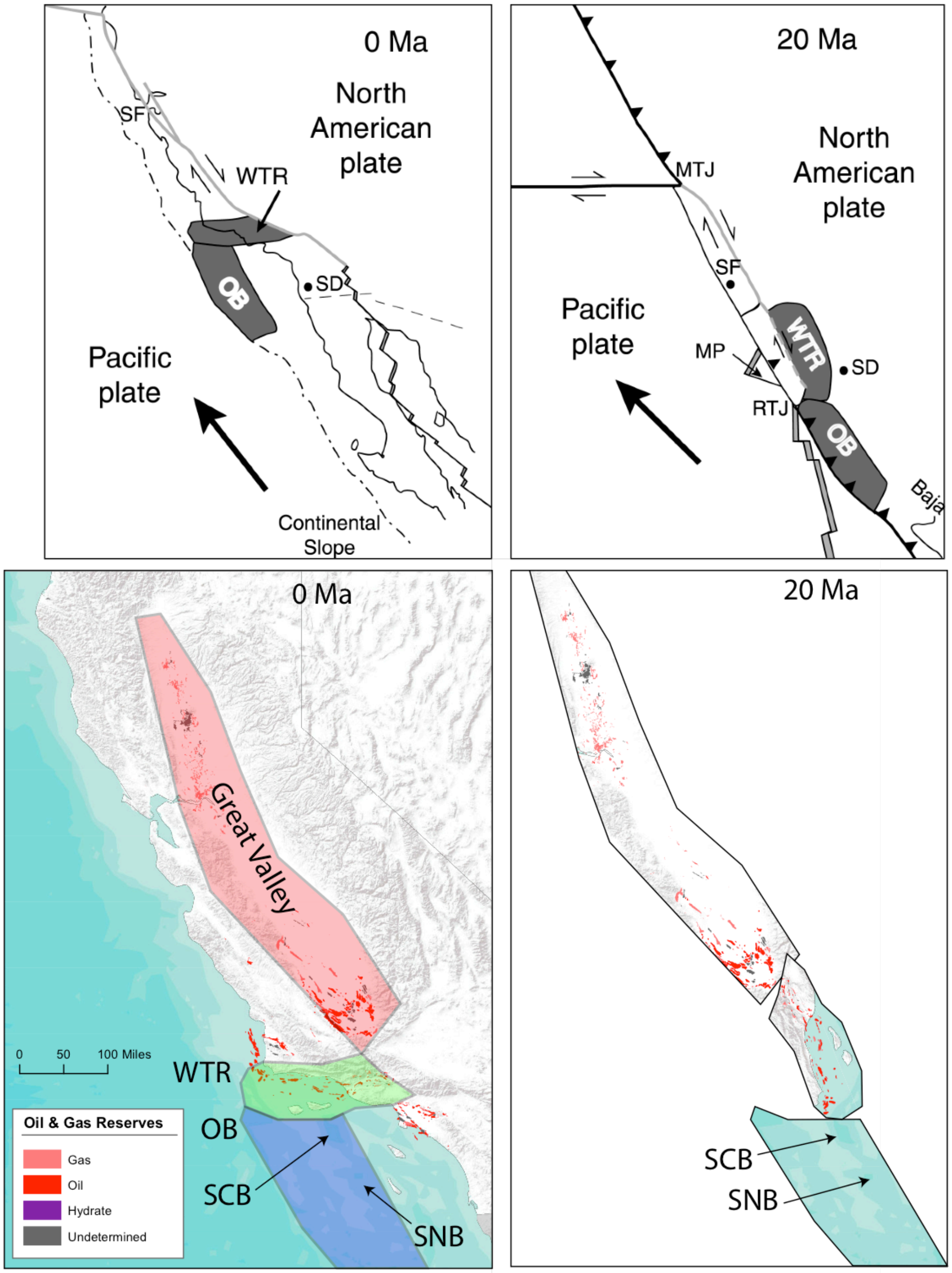

Figure 4.2: Tectonic reconstruction of the California Borderlands from 20 million years ago (right column) to present (left column). Upper row shows translation of the Outer Borderlands and rotation of the Western Transverse Range. Bottom row identifies currently discovered oil and gas fields in California. The Outer Borderlands has the same source rocks that source the oil and gas found in the Great valley and Western Transverse Range, and were once aligned in a similar depositional environment prior to 20 million years ago. Oil and gas fields adapted from Thomas and Pointe (2009). Tectonic reconstruction based on Nicholson et al. (1994) and Miller (2002).

4.3 Methodology

4.3.1 Instrumentation

The target of the CSEM surveys in the Santa Cruz Basin was a continuous BSR that stretched the width of the basin. In the center of the basin, the BSR becomes bedding parallel, and is indistinguishable from the local bedding planes. A research cruise to map hydrate in the Santa Cruz Basin took place in June of 2014. This survey used the Scripps Vulcan array; a shallow sediment focused array consisting of a deep towed electric field transmitter, "SUESI", followed by 4 electric field receivers, known as "Vulcans".

The transmitter used in the Santa Cruz Basin had a 100 m transmitter antenna (110 m total length with 10 m copper electrodes) which broadcasted a 200 A "waveform-D" signal transmitted at a 0.5 Hz fundamental frequency. This signal was received on 4 Vulcan receivers, each separated by 200 m, with a maximum source receiver offset of 1220 m. The arrays were navigated using an inverted long baseline system (ILBL) designed to locate SUESI, a transponder at the end of the antenna, and another transponder at the end of the receiver array. Unfortunately, only SUESI could be accurately navigated, possibly due to kelp fouling the surface transponders of the ILBL system, or the slant ranges of the longer, deeper array were too great to accurately resolve. In the absence of array navigation, receiver positions were reconstructed assuming that the receiver array followed SUESI through the water.

4.3.2 Data Processing and Modeling

Time series data were processed using the method described by Myer et al. (2011) whereby time series data are Fourier transformed over the period of the fundamental transmitted frequency, then stacked over 60 s. By Fourier transforming the smallest period of data possible, data errors can be calculated from the stacking variance. In practice, these data errors are typically smaller than the effect of navigation errors. The now-standard method of recovering accurate phase by sending a GPS-synced timing pulse to each receiver had not yet been implemented in these surveys. The accuracy of the internal clocks is too uncertain to trust phase measurements, and so all inversions rely solely on amplitude data, excluding phase.

Once the data are processed, they are inverted using the MARE2DEM inversion code of Key (2016) to produce resistivity models. MARE2DEM is a 2.5D finite element inversion program that uses the Occam inversion method (Constable et al., 1987), which first minimizes the data misfit, then finds the smoothest model that fits the data to the target misfit. In this way, a unique solution is found from a non-unique problem, and ensures that any structure present in the model is required by the combination of data, error structure, and model parameterization. Line inversions are parameterized with a bathymetry tracking parallelogram mesh where each parameter is 200 m by 20 m. For areas of interest, a focused inversion of specific anomalies identified in the line inversion is performed. In these inversions, the parameter size is decreased to 50 m by 10 m parallelograms. In each line, this mesh spans beyond the edge of collected data and extends to 1200 m below seafloor. Beyond that an efficient triangular mesh extends to the model boundaries, 100 km in each direction. Seawater conductivity is fixed using values measured on the conductivity sensor aboard SUESI.

4.3.3 Santa Cruz Basin Seismic Data

Each of our survey lines was towed coincident with publicly available legacy 2D seismic data in the Santa Cruz. Comprehensive seismic data acquisition stopped in 1982, when the federal government stopped selling oil and gas leases offshore California. Seismic profiles shown here were collected in the late 1970s and early 1980s. The seismic data are time migrated, and velocity models are either absent or too sparse to inform depth conversion. For comparison with resistivity profiles, seismic profiles were depth converted using a fixed value of 1600 m/s, which should be sufficient for comparison in the shallow sediment where hydrate is present. The precise frequency of the seismic source is unknown, but given the age, it is likely that it is relatively low frequency, which is more sensitive to the BSR, but will have lower resolution (Hillman et al., 2017).

4.4 Results

In the Santa Cruz Basin, six lines were towed, three along basin strike (lines 4-6), and three perpendicular (lines 1-3) (Figure 4.3). Data quality is generally good across the basin with all receivers capturing useable data. The nearest Vulcans have three useable frequencies at the first three harmonics (1.5, 3.5, and 6.5 Hz), while at the furthest Vulcan only the first and second harmonics were useable. The fundamental frequency suffers from low signal to noise ratios for two reasons; firstly, the "waveform D" purposefully lowers the power at the fundamental frequency to increase the power at higher frequencies where attenuation is higher, and secondly, the number of data points stacked over a given stack window is much less than at higher frequencies. Therefore, data at the fundamental frequency was excluded from inversions. Figure 4.4 shows amplitude and phase data for the inline and vertical dipoles of the second Vulcan at 1.5 Hz. While the phase data appears useable, there is an unknown timing offset that varies by receiver renders the phase data uninvertable.

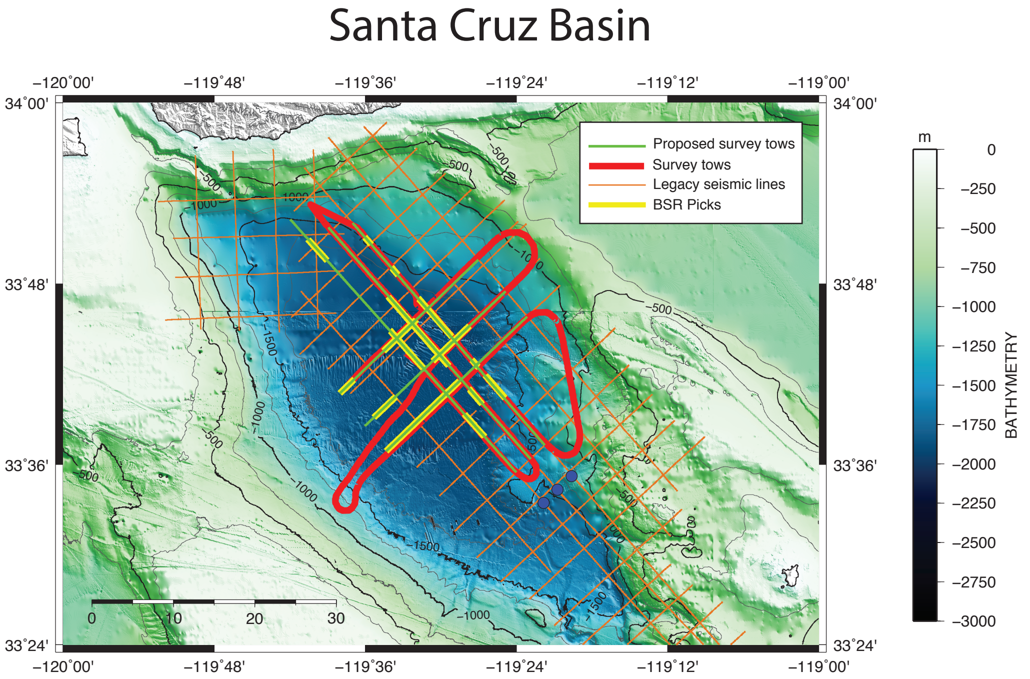

Figure 4-3: Santa Cruz Basin survey lines as towed. Green lines are the proposed survey lines, which were coincident with legacy seismic lines (thin orange lines). Yellow lines are the locations of bottom-simulating reflectors picked from those legacy seismic profiles. Thick red line is the actual position of the transmitter as it was towed over the seafloor.

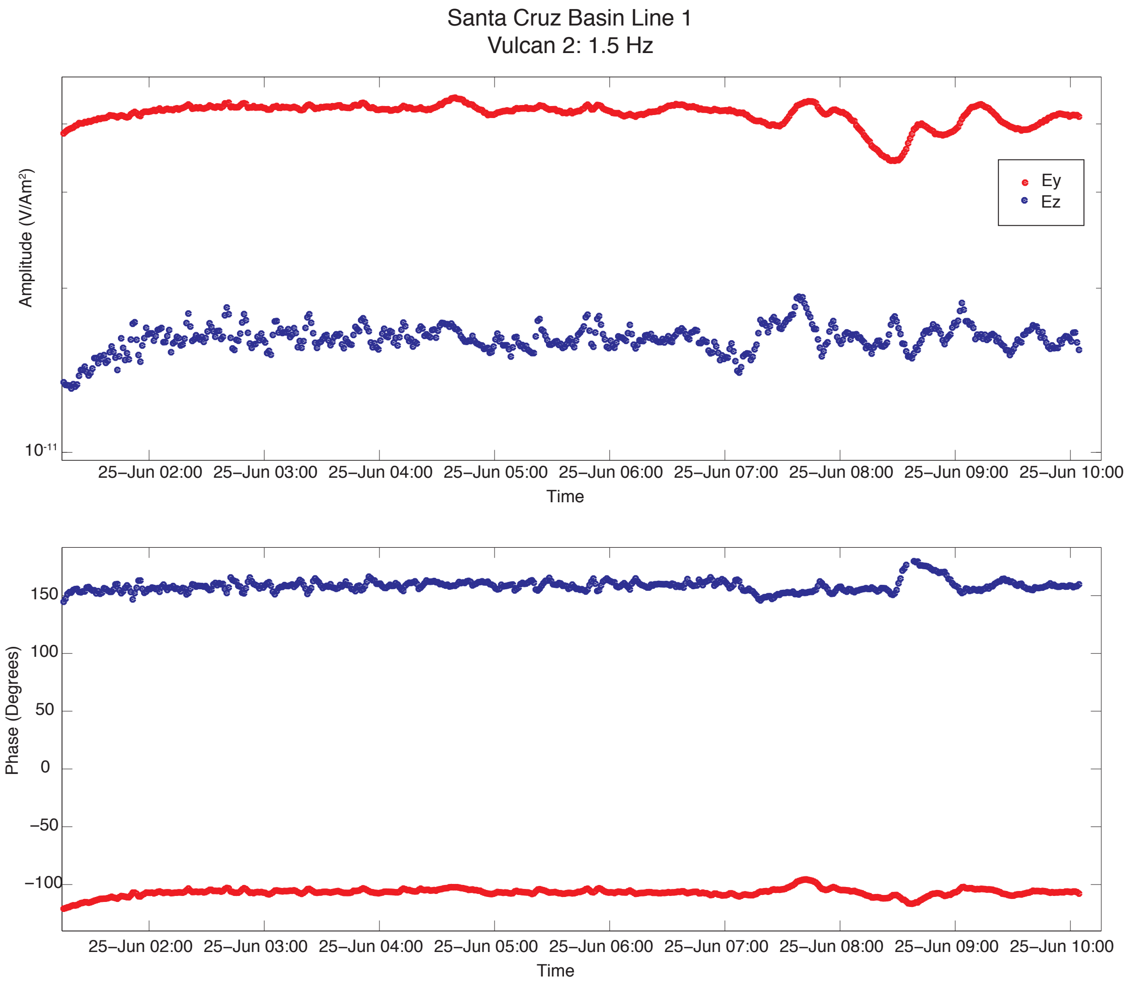

Figure 4.4: Amplitude (upper plot) and phase (lower plot) data of line 1 from the 2nd Vulcan at 1.5 Hz, the first odd harmonic. Inline dipole (Ey) shown in red and the vertical dipole (Ez) is shown in blue. At this source receiver offset, the inline electric field is about 5 times stronger than the vertical field. High frequency fluctuations, especially apparent in the vertical amplitude, are the result of navigation and array geometry changes.

BSRs picked from seismic profiles are present throughout the basin, shown as yellow lines in figure 4.3. The BSRs are clearly cross-cutting local strata along the edges of the basin, and become bedding parallel in the basin center. These BSRs are often continuous throughout the central basin, but become discontinuous on the flanks. Resistors in the Santa Cruz Basin tend to be strongest at the estimated depth of the hydrate stability field. Highest resistivity values were found on the flanks of the basin, with lesser, patchy resistors present in the central basin. On the flanks, resistivity reaches ~10 Ωm, while in the central basin the maximum resistivities are 2 Ωm, with sediments modeled at 1 Ωm.

Isotropic inversions of an anisotropic model produce strong striping as the model oscillates between resistors and conductors in an effort to create the effect of anisotropy in the data, producing geologically unrealistic models in which sediments in the isotropic models can be more conductive than the seawater. This effect is illustrated in Figure 4.5 where isotropic inversions are compared to anisotropic inversions. Marine sediments are typically anisotropic, especially in basins where shale content is high (Ellis et al., 2010). With the exception of those in figure 4.5, all inversions discussed here are vertically anisotropic, where both horizontal directions have equal resistivity, but the vertical resistivity can vary. For each survey line, a number of inversions were performed at a range of anisotropic penalties (the penalty between horizontal and vertical resistivities). Out of that set, a preferred model was chosen based on geologic plausibility. Anisotropic penalty in the inversions shown here typically range from 0.05-0.01. Inversion line locations are shown in figure 4.6.

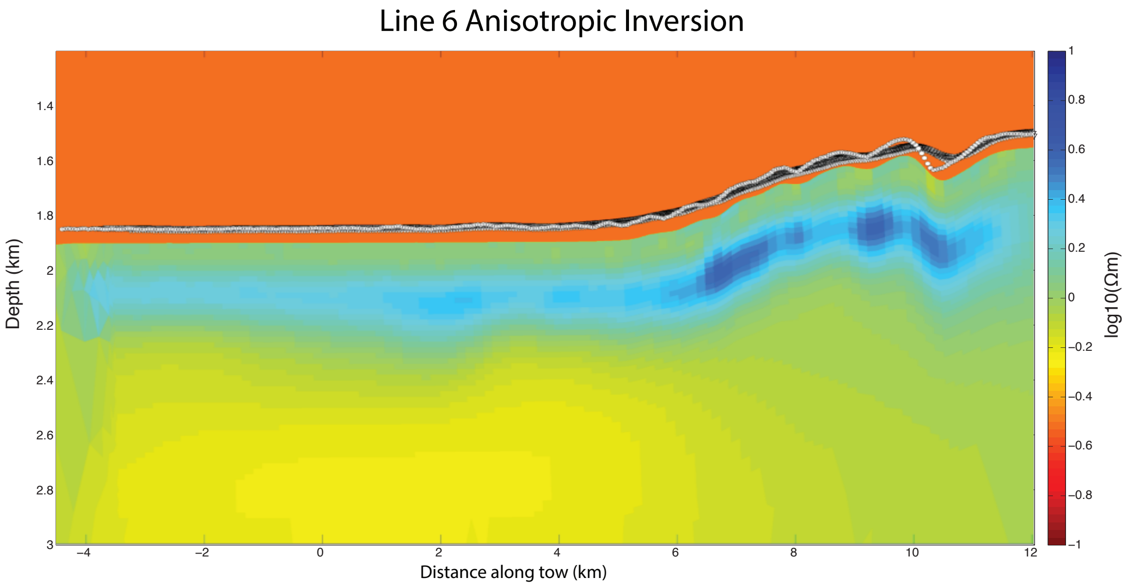
Line 6 Anisotropic Inversion

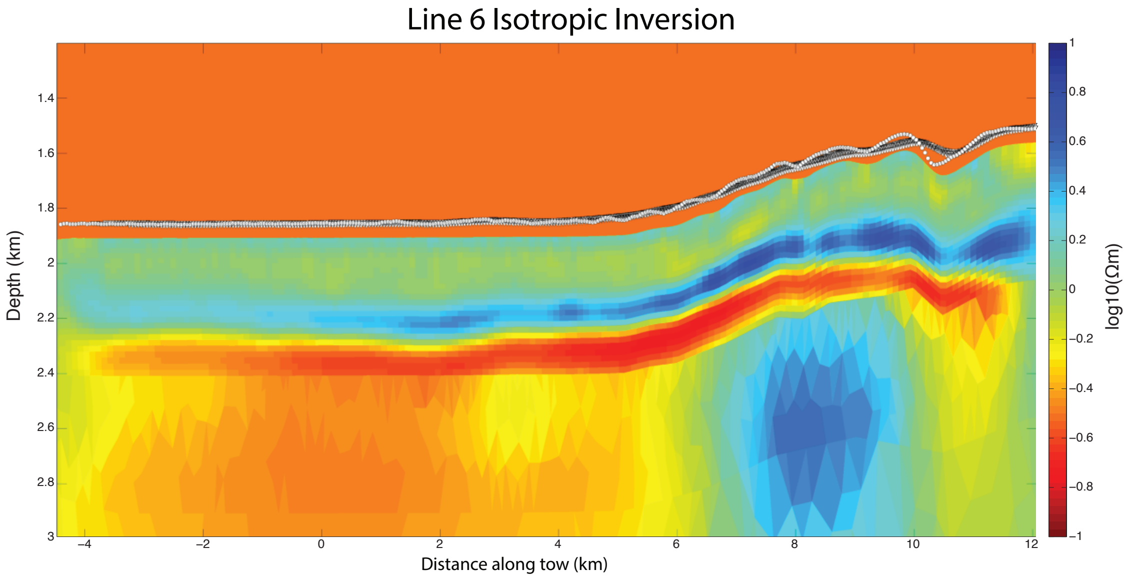
Line 6 Isotropic Inversion

Figure 4.5: Comparison of isotropic and vertically anisotropic inversions of line 6 dataset. Upper figure is the vertical resistivity component of the anisotropic inversion, with peak vertical over horizontal anisotropy ratio reaching 6 and is associated with increased vertical resistivity on the southeastern flank (right side of profile). Bottom figure shows the isotropic inversion of the same dataset. While the upper resistors are roughly in the same location, their absolute resistivity is increased, and they overlay geologically unreasonable conductors. On the right side of the profile these conductors in turn overlay another resistor. This striping is commonly observed when inverting anisotropic models isotropically.

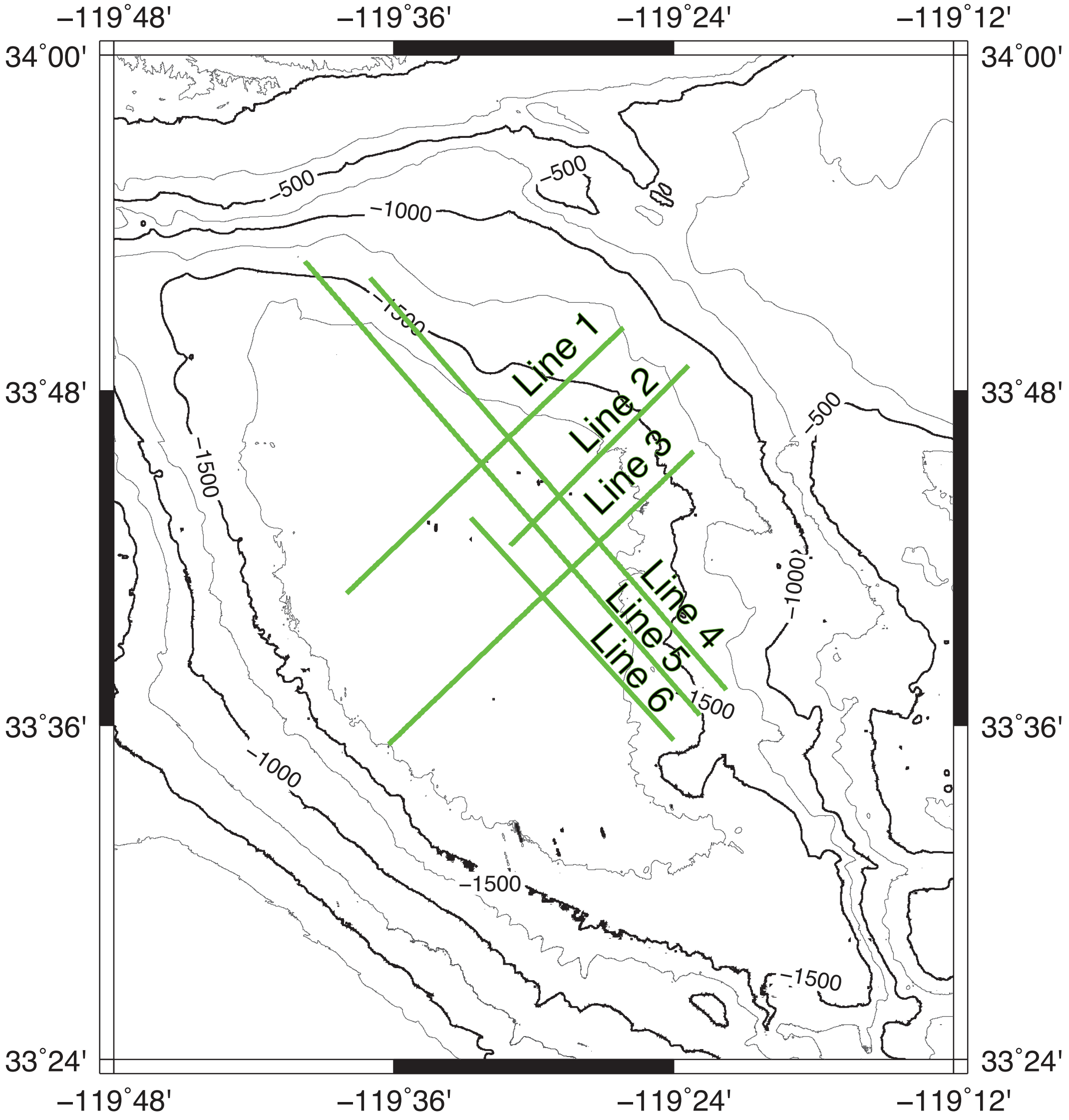

Figure 4.6: Map of Santa Cruz Basin inversion locations and extent. Line 2 was truncated by an unplanned course change, while line 6 was shortened due to time constraints.

4.4.1 Line 1 Inversion

Line 1 is the most northerly line, extending from the broad, flat central basin to the northeastern flank. The central basin is marked by patchy resistivity whose locations tend to correspond with places where high amplitude reflectors cross the BSR (Figure 4.7). This line was expected to have the highest hydrate concentration based on seismic evidence of hydrate formation. At the toe of the flank, a polarity reversal occurs as the reflector crosses the BSR at kilometer 25 in figure 4.7. This polarity reversal is probably caused by seismically slow free gas below the BSR transitioning to seismically fast hydrate above the BSR. Occurances such as this are typically targeted by drilling operations as it is one of the few direct indicators of hydrate formation that is inferable from seismic data alone (Cook et al., 2009). However, the CSEM response we see in that area is small, and the inversion of line 1 shows the feature to have a resistivity of 2 Ωm, less than many of the other resistors on the line. Increased resistivity is more prominent further up the flank, with high resistivities associated with high amplitude anticlinal structures in the seismic data. The BSR is weak or absent across most of the flank, and is indistinguishable amongst the chaotic, mottled reflectivity at the anticlines. The association of high resistivity with dipping beds as they cross into the HSZ, whether they occur in the central basin or on anticlines on the basin flanks, suggests that for hydrate deposits to accumulate, a migration pathway must exist to concentrate flow of methane rich fluids. All of these resistors are found at or above the base of the HSZ.

Figure 4.7: Santa Cruz Basin line 1 resistivity and seismic profiles. Top plot is the resistivity profile, shown with a logarithmic academic color scale, where cooler colors are resistive and warmer colors are conductive. Middle plot is the coincident seismic profile, pseudo-depth converted using a constant velocity and the lower plot is the resistivity profile overlain on the seismic data. Line location shown in figure 4.4.

Line 1 Resistivity

Anisotropic Rho z, RMS: 4.2 Inline amplitude with 1% error floor, vertical amplitude with 2% error floor

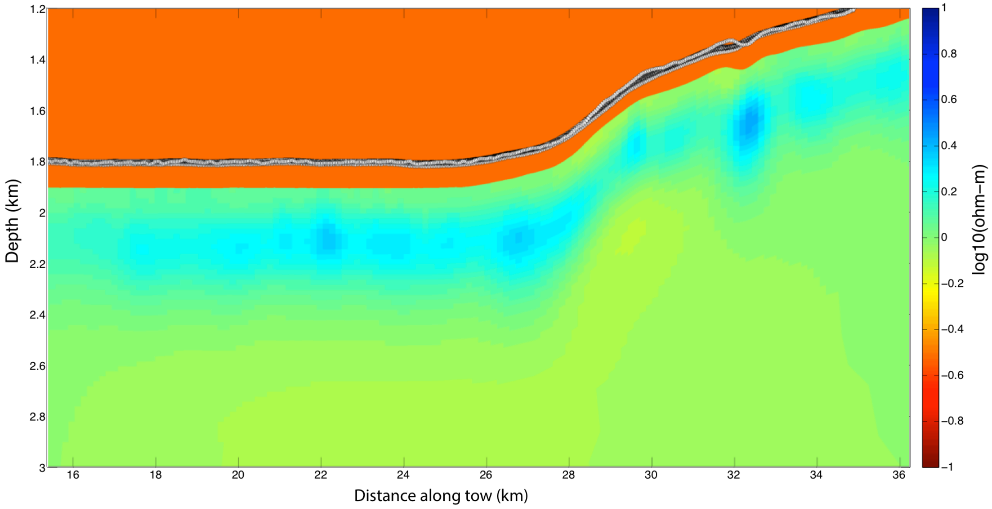

Line 1 seismic profile

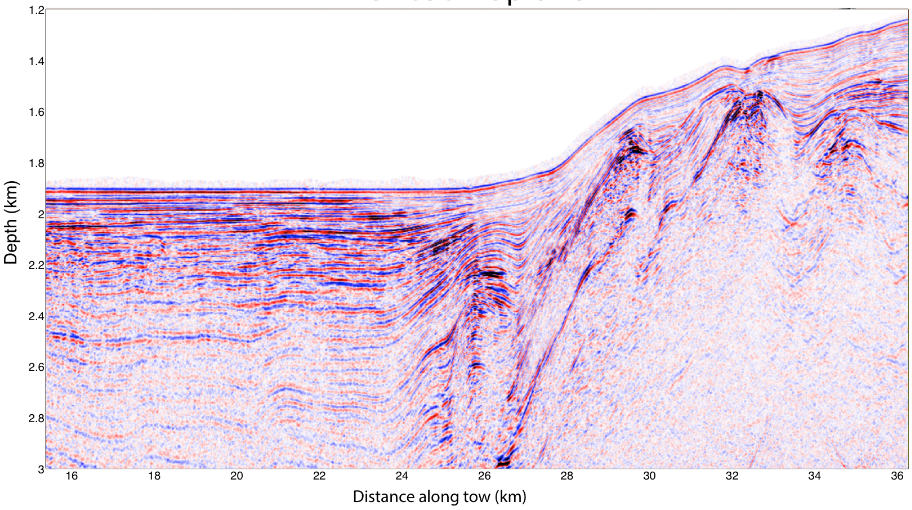

Line 1 Seismic overlain on Resistivity

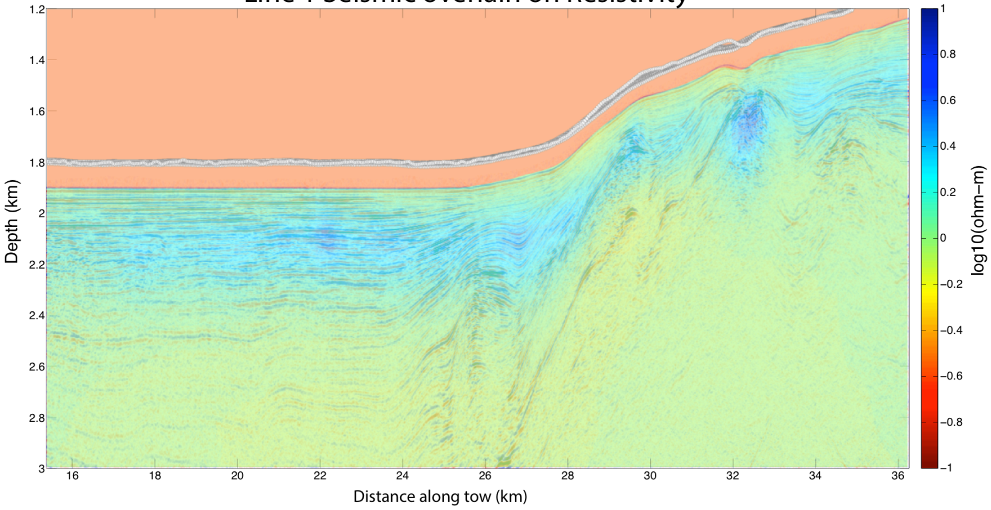

4.4.2 Line 2 Inversion

While survey lines were towed as near to legacy seismic lines as possible, we had to deviate from line two as planned to avoid live fire exercises by a nearby US Navy destroyer. Unfortunately, this course change limited the useable data along that line, as the offline data no longer conformed to the 2D approximation of MARE2DEM. The inversion of line 2 includes data up until the course change (Figure 4.8). Two prominent resistors are present on the line, and occur on the flanks of an anticline where steeply dipping beds cross into the HSZ. Strong BSRs are coincident with the resistors, which bracket the anticline. The northeast side of the anticline is bounded by a fault (kilometer 29 in figure 4.8) that could be transporting methane and other hydrocarbons to the shallow sediment. At kilometer 32, there is a conductor 400 m below seafloor. Increased conductivity in sediments is either the result of increased pore fluid salinity, or increased porosity. The coincident seismic data are largely featureless, but the conductor underlies a negative amplitude anomaly, indicating decreased velocity across the reflector. The reflector is at the same depth as the BSR, but the eastern end of the reflector turns sharply downward, which would only occur as a result of a sudden lateral drop in heat flow, which is unlikely. It is unclear what this reflector and underlying conductor represent geologically. This part of line 2 is towed above a shallow ridge crest, so off-line energy could be refracting and reflecting back onto line 2, obfuscating the seismic data.

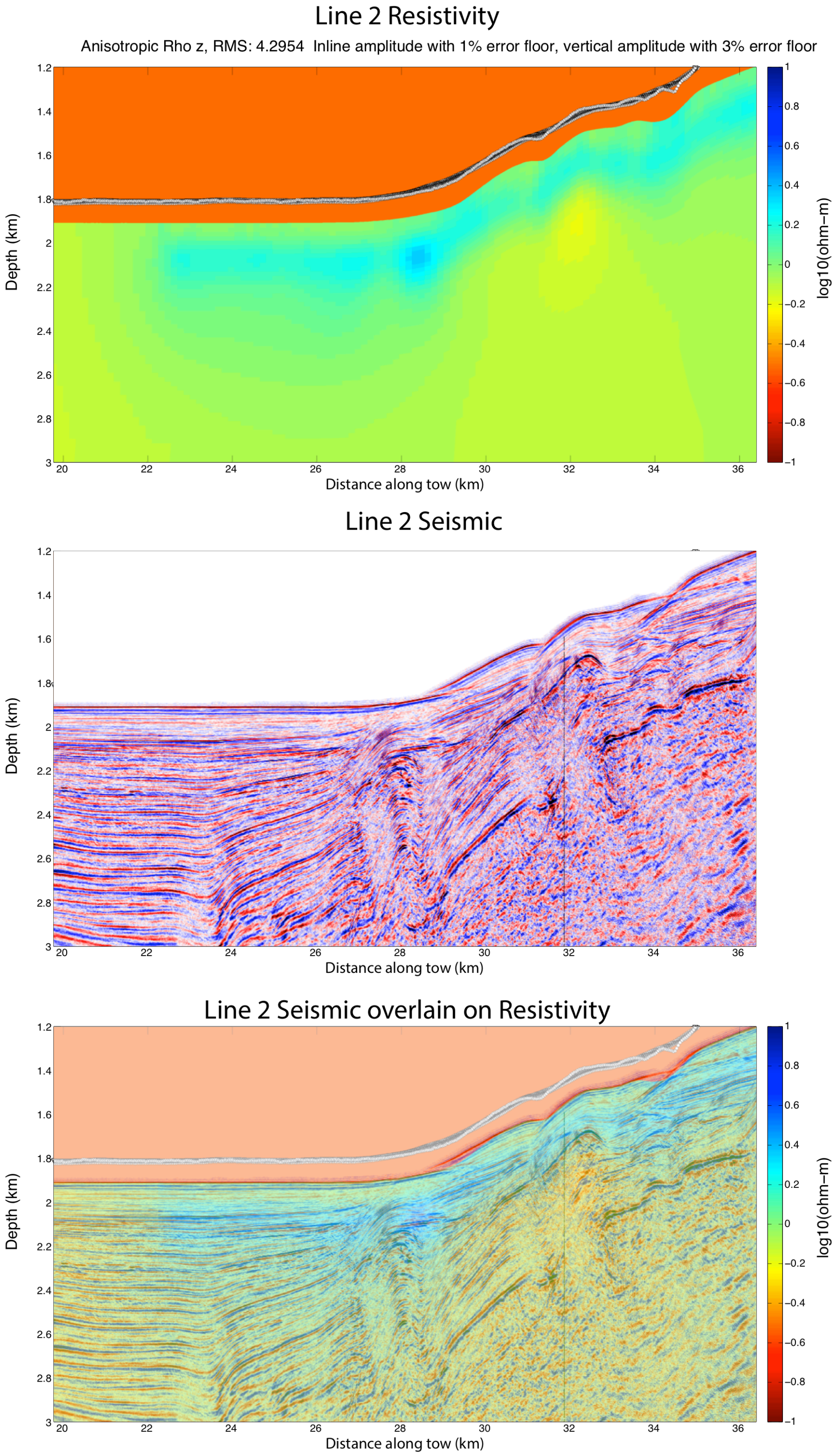

Figure 4.8: Resistivity (top), seismic (middle) and combined (lower) profiles of line 2.

4.4.3 Line 3 Inversion

Line 3 is the only line to transect the entire basin from southwest to northeast. The southwest flank shows high resistivity, up to 10 Ωm, within the estimated HSZ (Figure 4.9). There are no seismic data on this portion of the line, as the seismic line aswe were following does not extend up the southwest flank, and no other seismic lines in the area overlap onto this part of the Santa Cruz Basin. This resistor is unlikely to be volcanic, as any volcanics present should be much deeper on this side of the basin. Additionally, there is a strong BSR at the southwestern end of the seismic profile, suggesting that this resistor is hydrate. As with the rest of the inversions, the central basin exhibits patchy resistivity. On the northeast flank, resistors are draped across a fault bounded anticline, with the highest resistivity coincident with a fault at kilometer 27. Further upslope, at kilometer 30, the strong resistor is associated with a high amplitude reflector in the seismic data.

Line 3 Resistivity

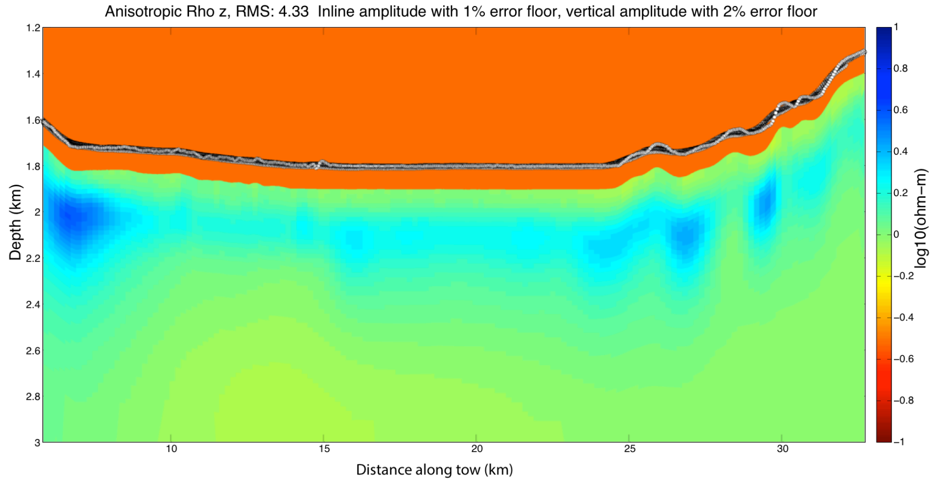

Line 3 Seismic

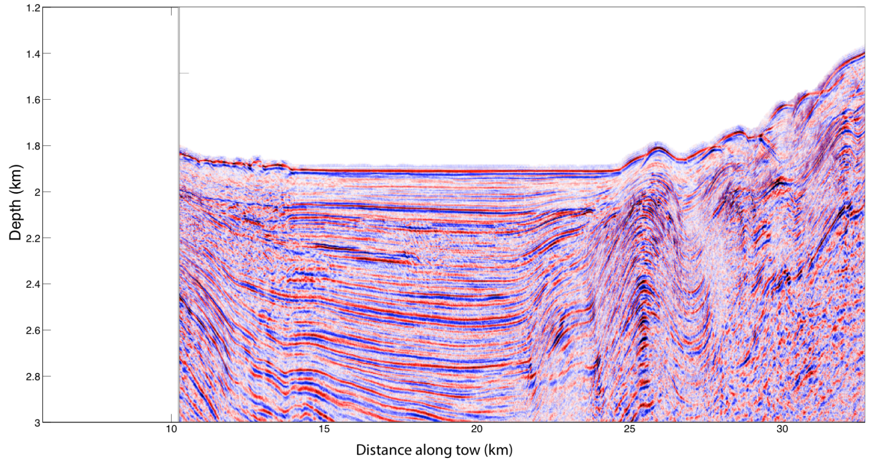

Line 3 Seismic overlain on Resistivity

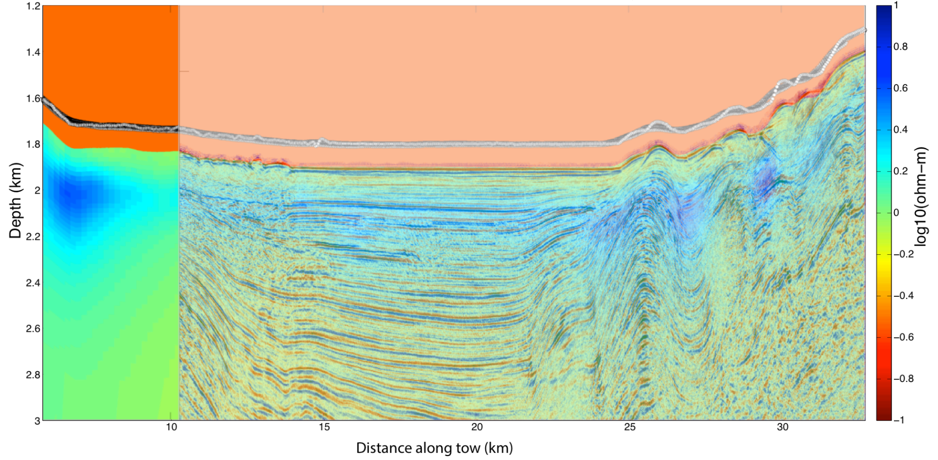

Figure 4.9: Resistivity (top), seismic (middle) and combined (lower) profiles of line 3. The seismic line does not extend as far as the CSEM profile, but there are strong resistors at the toe of the western basin flank.

4.4.4 Line 4 Inversion

Line 4 trends southeast-northwest, perpendicular to lines 1-3, and the resulting inversion produced the most surprising results of the survey (Figure 4.10). Line 4 contained the highest resistivity we measured in the Santa Cruz Basin, as well as exhibiting resistors that extended all the way from the base of the HSZ to the seafloor. As with other lines, the central basin shows weak discontinuous resistors, with the strongest resistors on the southeast flank. Strong resistors underlying bathymetric highs at kilometers 0-2 are associated with discontinuous BSRs, and if the focus of a higher resolution inversion. Further upslope, at kilometer 7.5, a resistor extends to the seafloor, and is interpreted to be a methane seep. A focused inversion was also performed at this site. The southeastern portion of line 4 follows the crest of a bathymetric ridge as it slopes into the central basin. Fluid flow is likely being focused towards the ridge crest, producing the strong resistors and seeps imaged here.

The first of two focused inversions on line 4 centers on the broad resistive region underlying two bathymetric highs. The resistivity of this feature peaks at 3-4 Ωm, the highest resistivity (kilometer 0.5 in figure 4.11) coincident with a discontinuous BSR. As the dipping seismic reflectors pass into the HSZ, there appears to be a polarity reversal, though the resolution of the seismic data may be too low for that to be definitively determined. Upslope at kilometer 2.5 is another 3 Ωm resistor associated with high amplitude reflectors. A BSR is not apparent here, though it would likely be bedding parallel, and indistinguishable from local sedimentary reflectors. The resistor at kilometer 1 pinches towards the seafloor, similar to the resistivity structure at the Del

Figure 4.10: Resistivity (top), seismic depth, converted using a constant velocity as in the other figures in chapter 4 (middle), and combined (lower) profiles of line 4. Inset boxes show the focused inversion extents for the eastern seep (figure 4.11) and western seep (figure 4.12). Clearly present at kilometer 7 is a resistor that extends from the base of the hydrate stability zone to the seafloor.

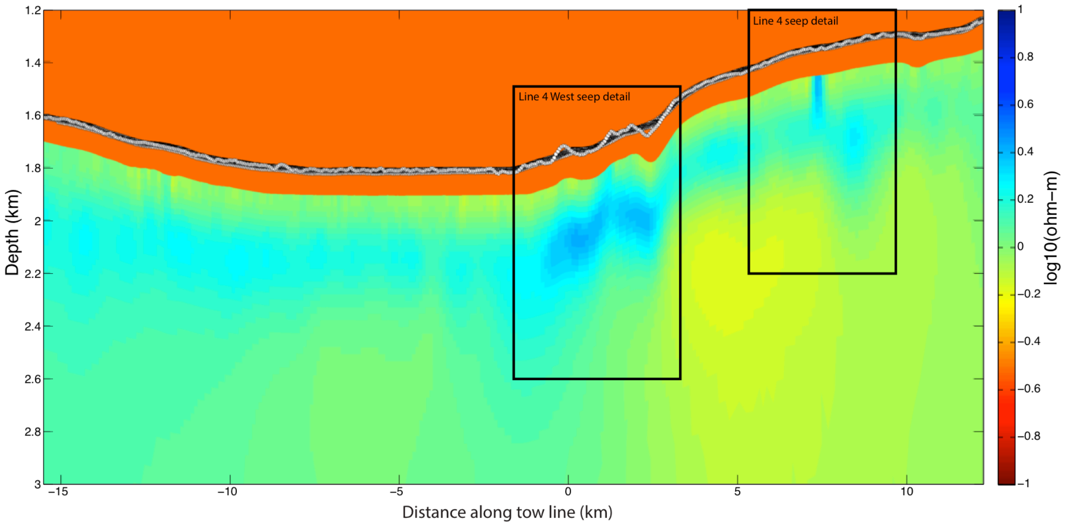
Line 4 Resistivity

Anisotropic Rho z, RMS: 3.4 Vulcans 2, 3, and 4, Inline amplitude with 1% error floor, vertical amplitude with 3% error floor

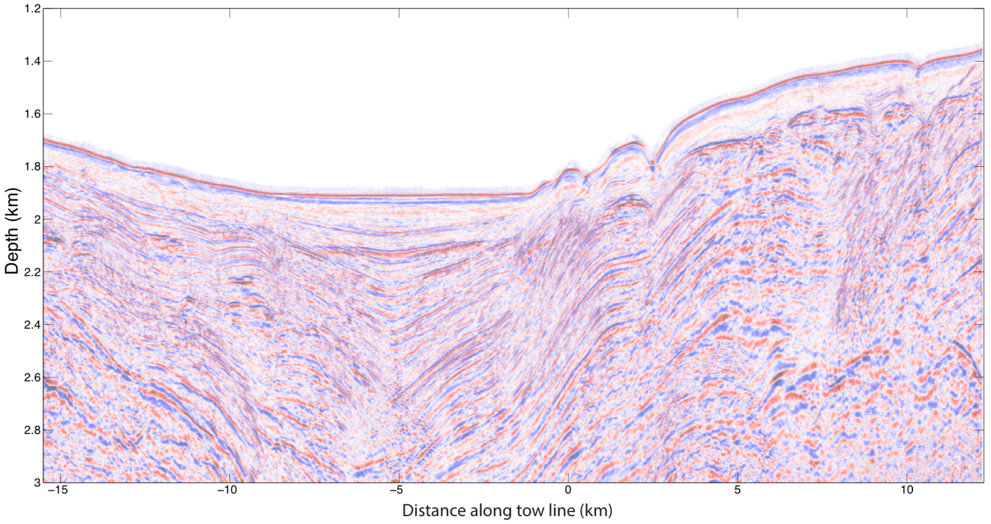
Line 4 Seismic

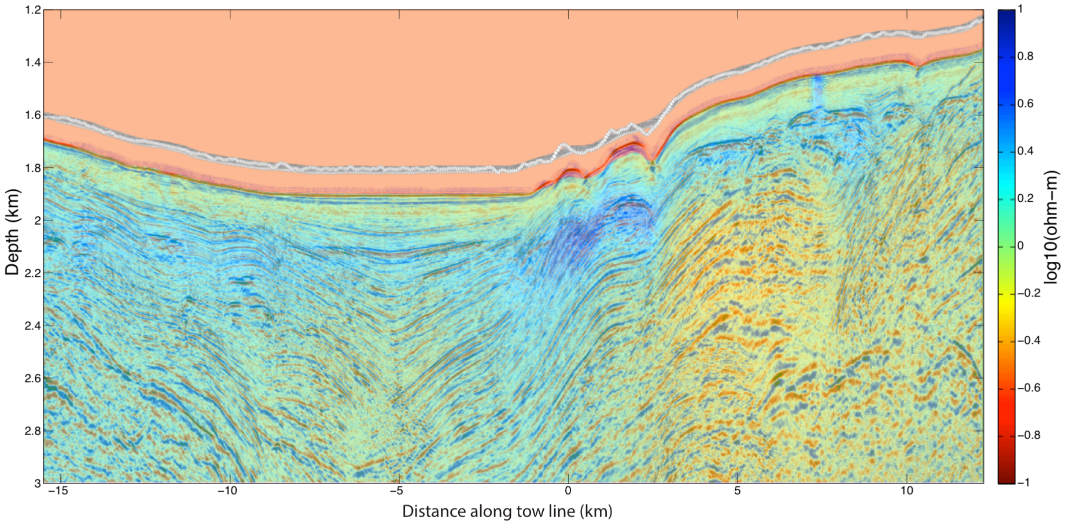
Line 4 Seismic overlain on Resistivity

Figure 4.11: Resistivity (top), seismic (middle) and combined (lower) profiles of the western seep on line 4. High resistivity regions are associated with both the broad anticline on the right side of the figure, as well as high amplitude reflectors crossing the BSR in the central portion of the figure. The high amplitude reflectors may produce phase velocity reversals, indicating a transition from free gas to hydrate, but given the low resolution of the seismic data, it is difficult to be definitive.

Line 4 West Seep Resistivity

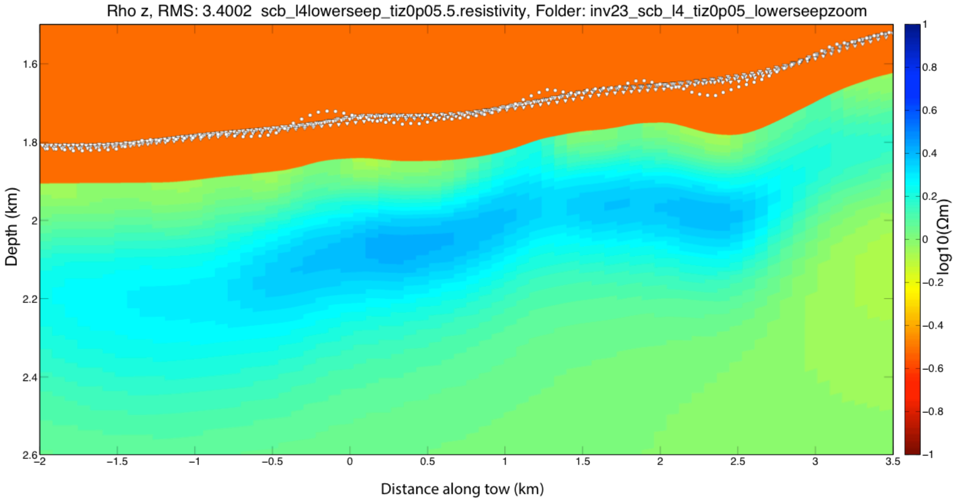

Line 4 West Seep Seismic

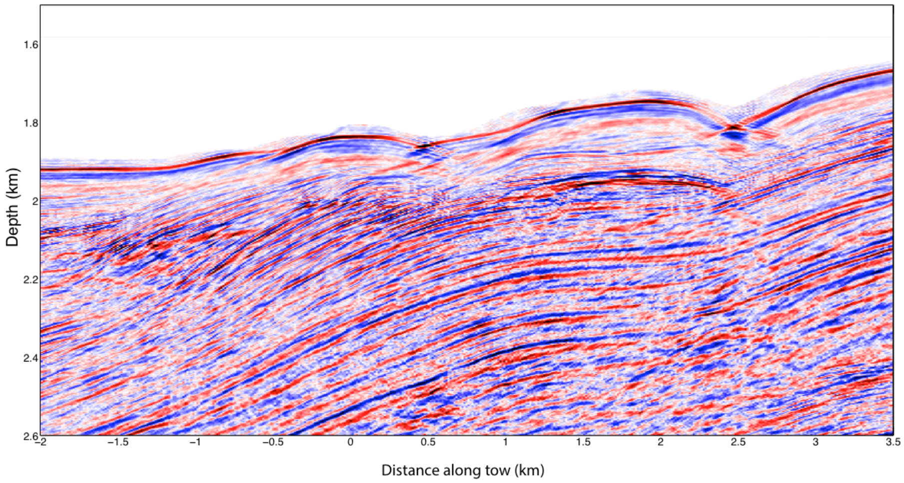

Line 4 West Seep Seismic Overlain on Resistivity

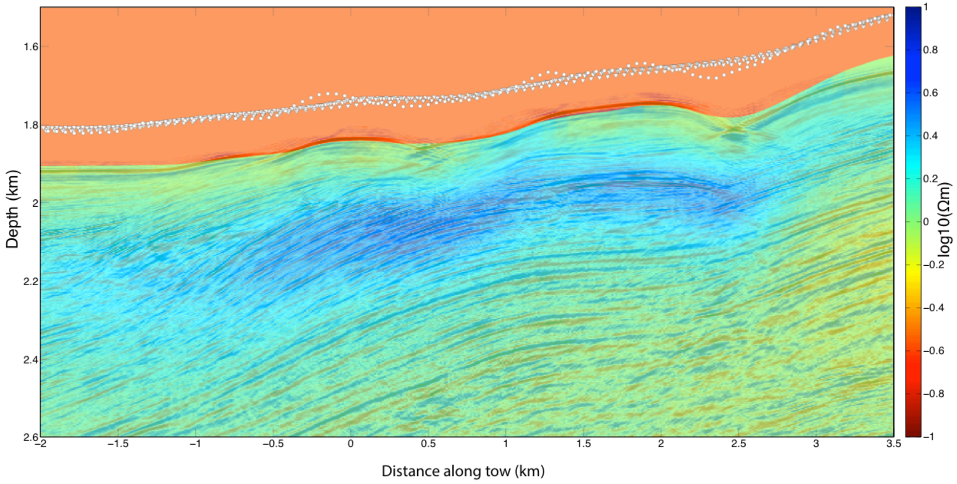

Mar seep. The faint appearance of this vertical resistor compared with the Del Mar Seep resistor is interpreted to be the result of our survey not crossing directly over the seafloor expression of the seep.

The vertical resistor stretching from the base of the HSZ to the seafloor was the site of the second focused inversion on line 4. This feature more closely resembles the structure of the Del Mar seep, with both having a broad tabular resistor just above base of the HSZ from the center of which is a narrow vertical resistor extending to the seafloor. The line 4 east seep, however, has a more complicated tabular body. A BSR is not readily apparent in the seismic data, though if the base of the HSZ is inferred from BSR depth elsewhere in the seismic profile, most of the resistor at the eastern seep lies above the BSR. However, at kilometer 8.5 in figure 4.12 the resistor extends below the base of the HSZ. This is interpreted to be either a free gas reservoir that is feeding the seep, or structure II hydrate forming in the presence of higher order hydrocarbons. The CSEM method is sensitive to the conductive pore fluids, so gas is indistinguishable from hydrate, as both are resistive materials displacing conductive brines. Seismic data, however, is highly sensitive to the presence of free gas (Lee et al., 2004). The seismic data at kilometer 8.5 does not have anomalously high amplitudes compared to the surrounding regions, though the seismic reflectors here are fairly chaotic. This implies that the resistor is unlikely to be the result of high concentrations of free gas. For this feature to be the result of structure-II hydrate, there must be a source of higher order thermogenic hydrocarbons. Schindler's (2010) seismic analysis of the Santa Cruz Basin interprets most of the eastern flank sediments to be middle Miocene to Cretaceous age. The middle Miocene includes the Monterey formation (Victor, 1997), a prolific

Figure 4.12: Resistivity (top), seismic (middle) and combined (lower) profiles of the eastern seep on line 4. The vertical resistor associated is interpreted to be hydrate and free gas culminating in a methane seep at the seafloor. Underlying the vertical resistor is a broad tabular resistor predominantly located above the base of the hydrate stability zone. The to the east, at kilometer 8.5 the resistivity seems to extend below the base of the s-I hydrate stability field, and is interpreted to be a gas reservoir or s-II hydrate.

Line 4 Seep Resistivity

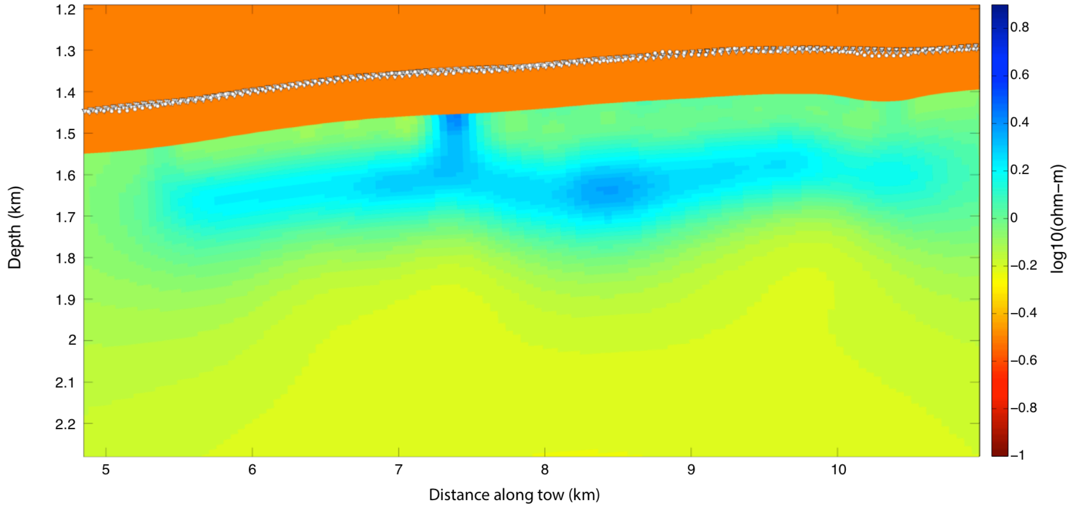
Anosotropic Rho z, RMS: 3.5 Inline amplitude with 1% error floor, vertical amplitude with 3% error floor

Line 4 Seep Seismic

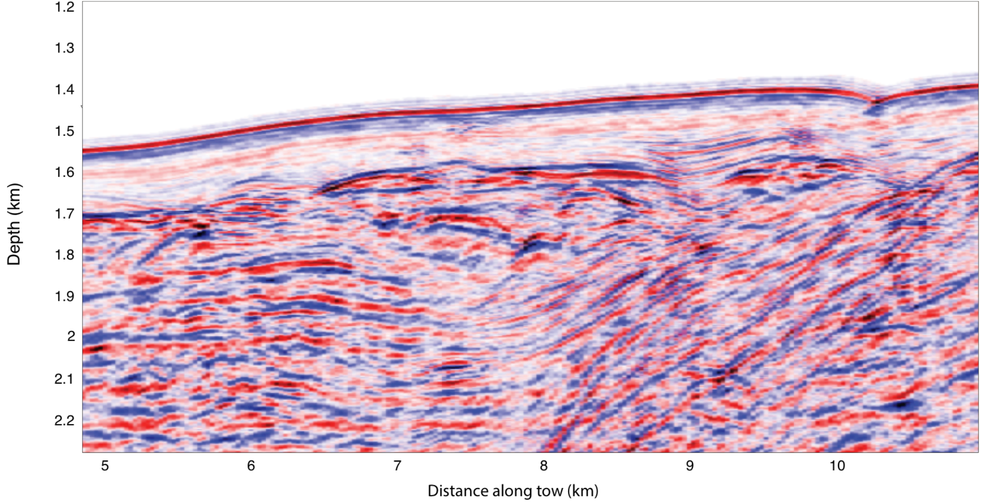

Line 4 Seep Seismic overlain on Resistivity

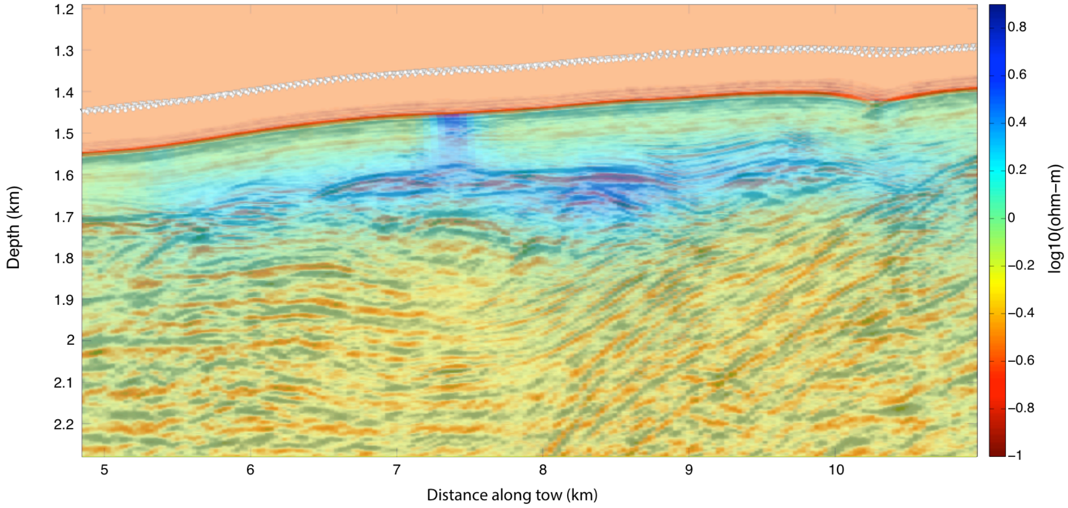

hydrocarbon source rock (Behl, 2012), while deeper sediments are composed of Paleogene-Cretacious sandstone that is also a thermogenic hydrocarbon source (Victor, 1997). Logging evidence of structure-II hydrate underlying a structure-I BSR was found at the Gumusut-Kakap oil and gas reservoir field by Paganoni et al. (2016). They found that the structure-II (s-II) BSR was ~80 m deeper than the structure-I (s-I) BSR. The offset between s-I and s-II stability curves is a function of gas chemistry and local temperature gradients. The gas chemistry of the Santa Cruz Basin is unknown, but the geothermal gradient ranges from 70-100 °C/km (Lee and Henyey, 1975), whereas at the Gumusut-Kakap it is 60-65 °C/km, resulting in a shorter offset between the base of the s-I and s-II HSZs. At the 8.5 km resistor in the Santa Cruz Basin, the resistor extends 75 m below the expected base of the s-I HSZ.

Located directly coincident with the vertical resistor at kilometer 7.5 in figure 4.12 appears to be a velocity pull-up structure. A pull-up structure is a localized shoaling of a reflector caused by higher velocity material that is not accounted for in the time-migration velocity model. The seep associated pull up structure could be the result of seismically fast hydrate deposits (but not oil or gas). The velocity of the sediments is unknown, but to cause the pull-up feature would require a 7% increase in velocity. Using the three-phase weighted equation with the weight of 1.0 from Lee at al. (1996) and a porosity of 0.5, which is conservative, this equates to an average hydrate saturation of ~12% above the reflector. Archie's equation (Archie, 1942) can be used to convert resistivity measurements into porosity. By assuming sediment porosity, the difference between the assumed porosity and the estimated porosity using Archie's equation will give the hydrate pore-space saturation. Using constants described in Chapter 3, and an average resistivity of 2.6 Ωm in the vertical seep resistor results in 15% pore space hydrate saturation. Given the low resolution of the seismic data and the lack of velocity models, the two methods are in good agreement.

Attached to SUESI was a CONTROS methane sensor, which was measuring dissolved methane concentrations 50 m above the seafloor. These sensors have been problematic, and absolute measurements cannot be trusted. One of the known issues with these sensors is that they are slow to respond to anomalies, and relict signal remains after the anomaly has passed. Despite these issues, a clear qualitative signal is present as the instrument is towed over the western seep on line 4 (Figure 4.13). Of the four anomalously high methane signals recorded, three are short, and only two are associated with resistors. The strongest signal is coincident with the vertical resistor at the western seep, and lasts for about 10 minutes. Another increased methane spike is coincident with the eastern seep, but the relatively weak signal is short lived.

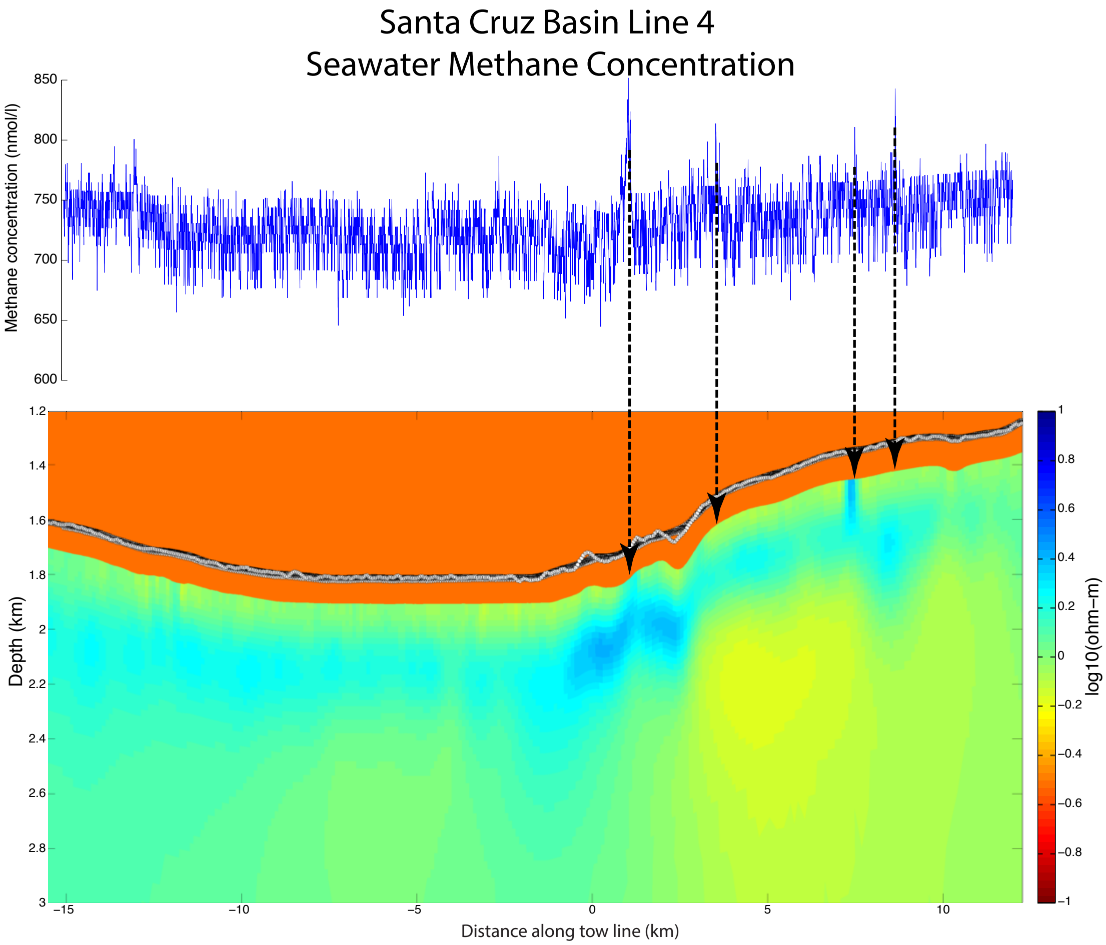

Figure 4.13: Relative methane concentration from a dissolved methane sensor shown with the resistivity profile of line 4. While the highest and broadest increased methane concentration anomaly is associated with the western seep, the eastern seep produces a much smaller methane anomaly. Two other anomalies do not appear to be correlated with seep resistors.

4.4.5 Line 5 Inversion

Line 5 is downslope of line 4 on the same bathymetric high. Sporadic resistors are present in the central basin in the line 5 inversion (figure 4.14), the strongest of which are coincident with the high amplitude reflectors cross the BSR. On the southeastern flank, resistors are concentrated in regions of high amplitude reflectors. As expected, there are no apparent methane seeps on this line. Warm, methane rich fluids would tend to be buoyantly driven towards the summit of the ridge, and are unlikely to pool here on the ridge flank. There is no clear BSR on the southeastern end of line 5. At the northwestern end of the line, the CSEM inversion extends beyond the edge of the seismic line. Once again we have a strong resistor, but no seismic data to help understand the structure and gas migration pathways.

4.4.6 Line 6 Inversion

Like the other lines, the resistors in the central basin of line 6 are patchy, and associated with bright reflectors crossing the BSR (Figure 4.15). Stronger resistors are present on the broad anticlinal structure on the southeastern end of the line. Line 6 was cut short due to time constraints.

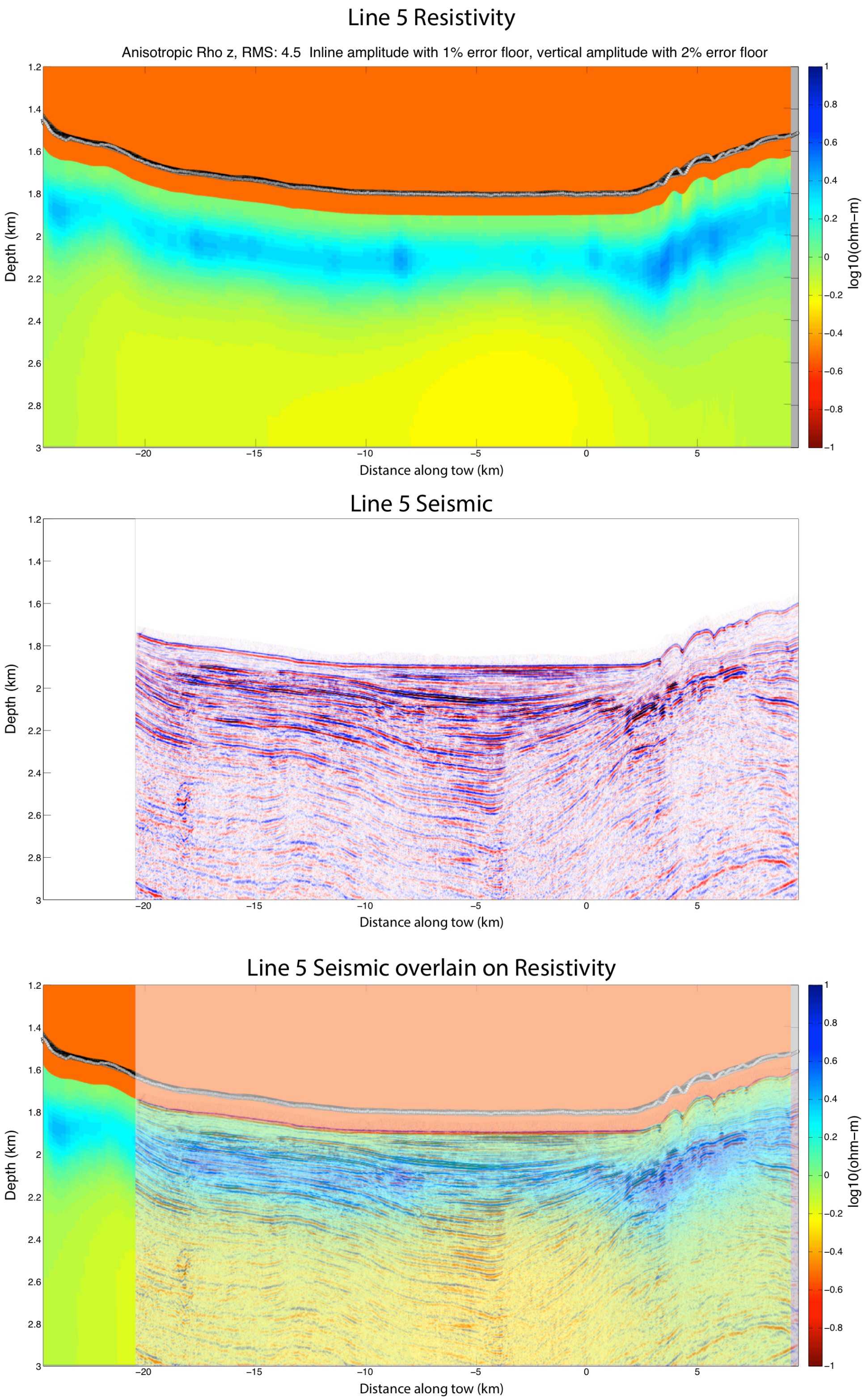

Figure 4.14: Resistivity (top), seismic (middle) and combined (lower) profiles of line 5. The seismic line does not extend as far as the CSEM profile.

Line 6 Resistivity

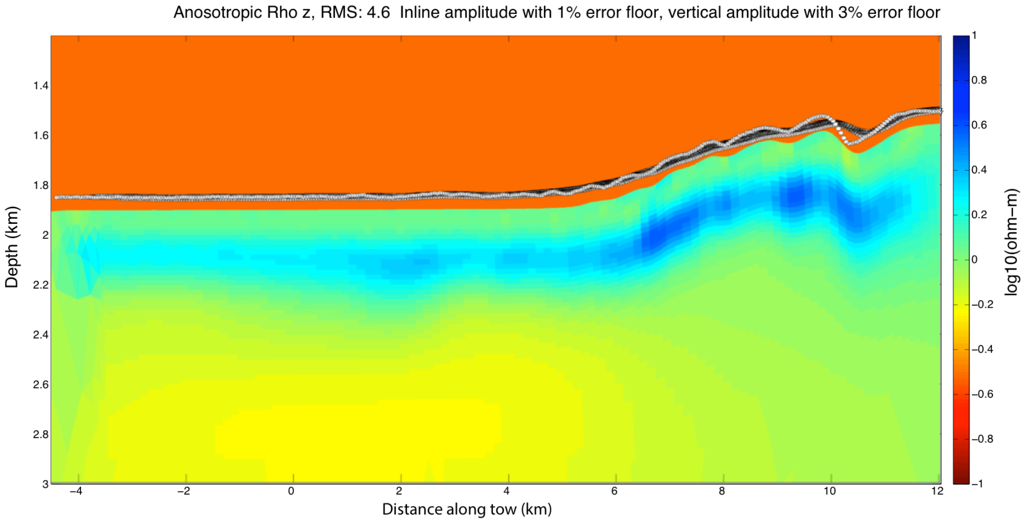

Line 6 Seismic

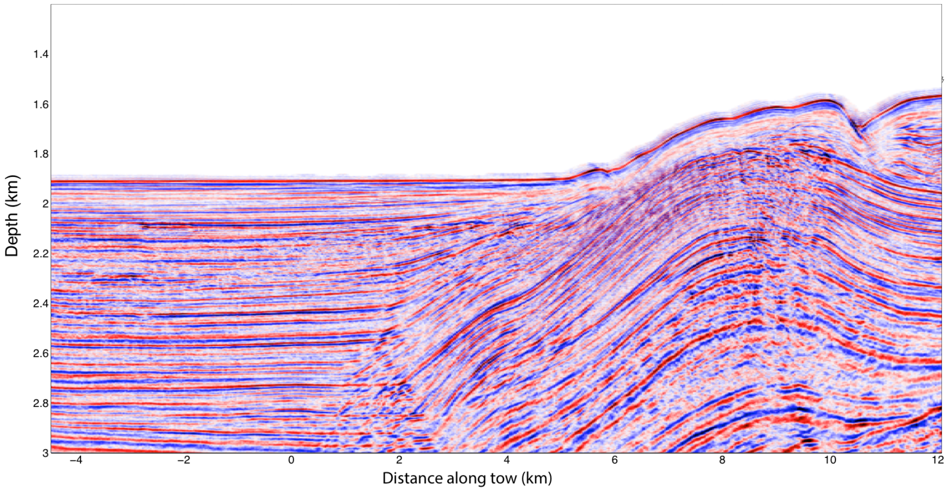

Line 6 Seismic overlain on resistivity

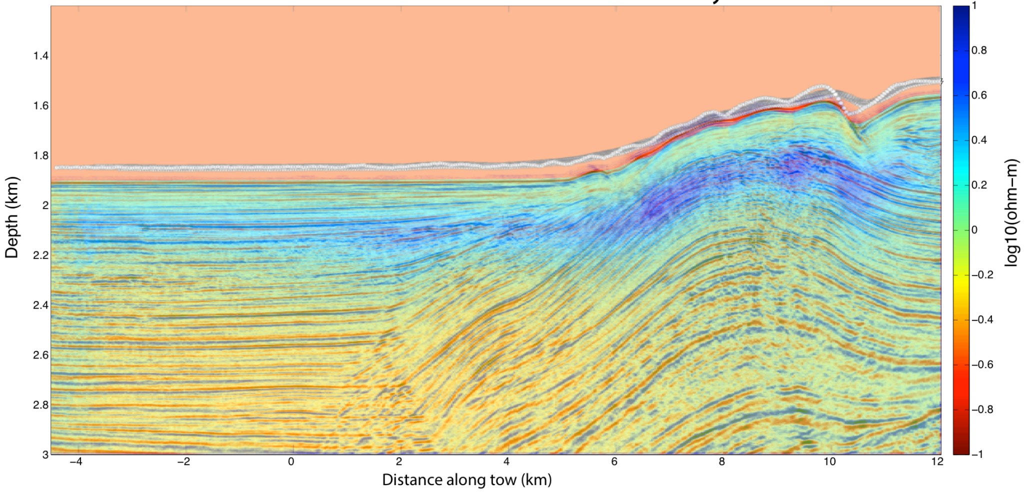

Figure 4.15: Resistivity (top), seismic (middle) and combined (lower) profiles of line 6.

4.5 Discussion

Our understanding of hydrate systems is evolving and we now view them as petroleum systems that need high permeability pathways in order to focus gas migration. Hydrate formation can serve as a trap in the absence of a lithologic one. In the Santa Cruz Basin, these gas migration pathways will tend to focus flow away from the center of the basin and towards the flanks, regardless of BSR presence. As has been found in the Gulf of Mexico, the presence of a BSR is not a strong indicator of hydrate occurrence (Majumdar et al., 2016). Likewise, in the Santa Cruz Basin, the strongest resistors we associate with hydrate accumulations are often found in the absence of a BSR. Furthermore, if only the presence of a BSR were used to guide drilling operations, the largest hydrate accumulations would be disregarded.

4.5.1 Abiotic Methane Potential of the Eastern Santa Cruz Basin

Thermogenic and biogenic methane form the vast majority of methane hydrate deposits. However, abiotic methane generation has recently been explored as an additional source of methane gas in Arctic marine sediments (Johnson et al., 2015). Abiotic methane generation follows the Fischer-Tropsch type reactions, where hydrogen, formed through hydration and serpentinization of ultramafic rocks, reacts with carbon dioxide to form methane and in the marine environment is typically associated with spreading ridges (Proskurowski et al., 2008, Johnson et al., 2015). In the Santa Cruz Basin, however, it could be result from hydration of the ophiolitic basement. Ophiolites are known to produce abiotic methane on land; Pliny the Elder in 79 AD noted the eternal flame produced in this manner at the Chimaera gas seep, in modern day Turkey (Etiope et al., 2011). This is the largest identified abiotic seep, and was the source of the first Olympic flame (Hosgormez et al., 2008). Other methane producing ophiolites have been found in the Philippines, Oman, and New Zealand (Etiope et al., 2011).

Fischer-Tropsch type reactions happen most efficiently at temperatures ranging from 200-350 °C (Martin and Fyfe, 1970), which occurs in the Santa Cruz Basin at depths of 2-5 km below seafloor, using a geothermal gradient of 70-100 °C/km (Lee and Henyey, 1975). However, abiotic methane generation is thought to occur at temperatures as low as 40 °C (Etoipe and Lollar, 2013), which equates to depths as shallow as 400 m below seafloor. On the northeastern edge of the basin, ophiolitic basement is interpreted from seismic data to exist at depths within 1 second of two-way travel time of the seafloor. Acoustic velocities of Miocene rocks measured in boreholes in the Outer Borderlands are high, measured to be up to 3000 m/s. Sonabuoy seismic data from the San Nicolas Basin, located southeast of the Santa Cruz Basin in a similar tectonic regime, measured Miocene sediments at 2000 m/s and Paleogene sediments at 4000 m/s. These velocities indicate basement depths within 2 km of the seafloor, but they are probably shallower than that. Ophiolites on the northeastern side of the Santa Cruz Basin are likely to exist within temperature ranges that favor abiotic methane generation.

Previously mentioned ophiolitic methane seeps are terrestrial, hydrated by meteoric water. However, in the Santa Cruz Basin, the ophiolite would be hydrated by seawater. The East Santa Cruz fault zone is an active fault, most recently producing a M5.0 earthquake in early 2018 (Patton, 2018). The increased porosity and permeability of faults provides a fluid pathway for hydration and serpentinization of the ophiolite. This type of crustal hydration of reactivated faults can be found at the Middle America

Trench, where Naif et al. (2015) found increased conductivity in faults that was attributed to rehydration as plate bending occurred on the subducting slab. In that study, fluidized faults extended up to 5 km below seafloor.

The potential for abiotic methane generation is present in the Santa Cruz Basin, however any methane generated in this manner is likely to be mixed with biogenic and/or thermogenic gases. Isotopic analysis is the only way to determine the source of the gas, as each gas generation mechanism imparts a specific carbon and hydrogen isotope signature during methane synthesis (Whiticar, 1999). Gas samples would have to be collected, either by collecting free gas at the seep, or recovering hydrate in core samples in order to determine gas source. Abiotic methane is not typically considered when calculating global carbon budgets, but there have been very few studies of abiotic methane generation in the marine environment, where favorable conditions may be more prevalent.

4.5.2 Other Electrical Resistors in Marine Sediments

Hydrate is not the only resistor present in marine sediments. Volcanics, especially basalt, and carbonates are both resistive and found in marine environments. In the outer California borderlands, basalt was cored in industry wells drilled on the ridges surrounding San Nicolas and Santa Cruz Basins. The basalt is related to volcanism caused by extension in the borderlands, and is early Miocene in age (Bohannon and Geist, 1998). In the center of the basin, any volcanics would be kilometers deep, while on the flanks where sediment thins the basalt could be within a kilometer of the surface.

Resistors present in the Santa Cruz Basin CSEM inversions are not interpreted as basalt because the resistive sections are limited to the HSZ.

Authigenic carbonates are associated with methane seeps, forming as a result of methane oxidation and sulfate reduction in the shallow sediments (Ritger et al., 1987). These carbonate deposits manifest in many forms, with carbonate pavements and pinnacles frequently found at seafloor while carbonate nodules are common in sediments. The pavements are typically thin (cm scale), but thicker blocks (m scale) are present at some seeps, such as southern Hydrate Ridge. CSEM surveys at active methane seeps have never imaged resistors in the upper 10 meters of sediment, where authigenic carbonates form. Additionally, a CSEM survey at Mississippi Canyon in the Gulf of Mexico showed no anomalous resistivity where authigenic carbonates are known to be present (Weitemeyer and Constable, 2011). This is either because the carbonates are of a similar resistivity to the surrounding sediments, which would indicate that they are porous enough to be indifferentiable from seafloor sediments, or the carbonates are too thin to be resolved using the CSEM method. Carbonates recovered from southern Hydrate Ridge show large interconnected cavities that were interpreted as gas migration pathways (Teichert et al., 2003). Carbonates are seismically fast, so it is possible that acoustic methods could identify them (e.g. Sleeper at al., 2006). However, active seeps where carbonates form typically have three phase methane flow, where hydrate, dissolved methane, and free gas coexist within the HSZ. The seismically slow free gas could confound seismic interpretation. Gravity is another geophysical tool that could be used to differentiate hydrate from carbonate. Hydrate has a density of 0.9 g/cm^3 (Holbrook et al., 1996), while carbonates are much denser, with values of 2.7-2.9 g/cm^3

(Anselmetti and Eberli, 1993). Based on FastGrav 2D gravity modeling, ship based gravimeters may be too far from the seafloor, and deep towed gravimeters may not have the resolution, to detect a gravity anomaly. Seafloor gravimeters would be capable of differentiating carbonate from hydrate, but are time consuming to deploy and recover. Seafloor gravimeters have been used to study hydrates, though they were used to evaluate hydrate saturation using seafloor compliance, and were not used to differentiate hydrate from carbonates (Willoughby and Edwards, 1997).

4.6 Conclusions

We have shown that a deep-towed CSEM array is capable of efficiently characterizing methane hydrate reservoirs in marine sediments. CSEM methods, which are sensitive to pore space resistivity, are a powerful tool for understanding hydrate saturation, and when jointly interpreted with geologic structural information from seismic reflection surveys, provide a broad understanding of gas migration pathways culminating in hydrate bearing sediments. When interpreting CSEM data, it is apparent that inverting the data isotropically leads to geologically impossible models, and anisotropic inversions are necessary to capture the anisotropy inherent in marine sediments in general and hydrate systems in particular. Across the Santa Cruz Basin, larger and stronger resistors interpreted to be hydrate are preferentially found on the flanks of the basin. BSRs are strongest in the central basin, but resistivity inversions show that increased resistivity is limited to places where high amplitude reflectors cross the BSR. Seismic phase reversals are considered to be dependable indicators of hydrate, but in the Santa Cruz Basin a prominent phase reversal is not associated with a particularly strong resistor. It is clear in the Santa Cruz Basin, that hydrate formation is predicated upon a gas source, and that in the central basin, the largely unfaulted horizontal sediments do not provide gas migration pathways sufficient enough to form measureable amounts of hydrate. Conversely, faulting and anticlinal structures provide ample gas pathways that feed hydrate reservoirs and methane seeps on the basin flanks. These gas pathways likely feed a mixture of biogenic and thermogenic gases to the HSZ, and even abiotic methane generation is possible due to the unique tectonic history of the Outer Borderlands. Methane seeps are prevalent in marine shelf and slope environments, but our understanding of the breadth of hydrate underlying these seeps is still evolving. While the seafloor expression of these seeps can be small, 10s to 100s of meters, the hydrate systems underlying these seeps can be measured in kilometers.

Chapter 5

Conclusions

CSEM methods are sensitive to pore fluid resistivity, and are uniquely suited to identifying and quantifying electrically resistive methane hydrate in-situ. Knowing the current extent and volume of methane hydrate deposits in ocean sediments is critical for identifying hydrate energy resources, assessing the increased risk of hydrate related slope failure, and recognizing hydrate that is vulnerable to climatic effects. We know that there are tens of thousands of trillion cubic feet of methane stored in technically recoverable hydrate deposits (Boswell and Collett, 2011). Because CSEM methods are sensitive to total hydrate volume, they are able to characterize hydrate reservoirs, differentiating those that are economically exploitable from those that aren't. In a warming world, a certain fraction of the hydrate in the ocean is susceptible to dissociation at bottom water temperatures increase. Quantifying how much shallow hydrate is present in climatically sensitive sediments is necessary to predict the oceanic and atmospheric effects of seafloor methane release. Slope stability is enhanced by the presence of hydrate, and decreased by hydrate dissociation. In addition, as seafloor infrastructure increases globally, locating hydrate using CSEM methods near these structures can help minimize potential hazards.

Oil and gas exploration typically tries to avoid hydrate bearing sediments, as the heat of drilling and cementation can dissociate hydrate, destabilizing sediments where platform anchors and boreholes are located. Current strategies to avoid hydrate involve first looking at seismic data, then drilling holes until locating a suitable site with minimal hydrate presence. Drilling is expensive, with day rates for drill ships hovering at $300,000 (Ihsmarkit.com, 2018). Seismic reflection data, especially in the absence of full waveform velocity inversions, is unlikely to be sensitive to hydrate. CSEM is more capable of detecting hydrate than seismic surveys, and is a fraction of the cost. Drilling days can be reduced by first conducting a CSEM survey, the results of which can be used to eliminate unacceptable borehole and platform mooring locations. However, industry is slow to adopt new technologies, and CSEM methods have never publically been used for the express purpose of identifying shallow hydrate related hazards.

Traditional CSEM surveys consisted of a deploying a series of seafloor receivers along a transect, then towing a transmitter over the receivers along that transect. The long source receiver offsets allow sensitivity to geologic structures kilometers deep. However, if the target depth is limited to the upper few hundred meters of sediments, seafloor receivers are of limited value due to the dense receiver spacing and requisite Deploying enough seafloor receivers to accurately characterize the upper sediment along a typical line would tax even the largest receiver fleets. Seafloor site spacing must be less than 250 m to match the data density of a 4 Vulcan array. To replicate the Santa Cruz Basin survey, where inverted lines measured 150 km, would require 600 seafloor receiver sites. While this could be broken up into individual lines, a single 35 km line in the Santa Cruz Basin would require 140 seafloor instruments, an unrealistic value for any institution other than Scripps Institution of Oceanography. Even if the number of seafloor instruments were not an issue, it would be difficult to justify the ship time needed to deploy and recover that many instruments. Deployment, navigation, and recovery of a single seafloor instrument takes about an hour and a half. In deep water, it would take 37 days of ship time to deploy and recover the 600 receivers necessary for a Santa Cruz Basin scale survey. Deployment of SUESI and the Vulcan array requires around two hours, and will be at depth recording data after another hour or two.

Instrumentation advances, especially the incorporation of a timing pulse from SUESI to the Vulcans, have been instrumental in improving our ability to accurately model geologic resistivity. The waveform generated by SUESI is transmitted down the tow-line to each of the Vulcans, where it is recorded and used to correct the drift on the internal clock. Implementing this has allowed incorporation of phase data into the inversions, doubling the amount of data in the inversion. Phase data is especially important because it is independent of amplitude data in a number of ways. Firstly, it is insensitive to changes in certain receiver geometries that affect amplitude, and secondly, phase is affected only by induction, whereas amplitude is affected by geometric, galvanic and inductive effects. This may be why incorporating phase into an inversion seems to help accurately model the sediments in the upper 10s of meters below the seafloor, minimizing the galvanic effect of the seafloor-ocean contact.

These improvements were tested during our survey of the Del Mar Seep, an active methane vent in the San Diego Trough. The results of this cruise demonstrated the capability of using CSEM methods to characterize hydrate reservoirs. The inclusion of phase data, coupled with an accurate error model based on data variance and uncertainties in instrument geometry allow for robust inversion results. We found a 1 km wide 25 Ωm tabular resistor underlying the seep, with a vertical resistor at the center extending to the seafloor at the vent site. A second line across the seep site confirmed the result. Total gas in place was estimated to be 2×10^9 m^3 using Archie's law. However, Archie's law has multiple shortcomings in this application. Firstly, it was not designed to be applied to anisotropic deposits, which both our inversions and well log modeling suggest is the case. Secondly, while Archie's law is non-linear, the resistivity thickness product that CSEM methods are broadly sensitive to is linear. Shallow targets such as hydrate should have more sensitivity to absolute resistor thickness than deeper targets, but there will still be some amount of tradeoff between resistivity and thickness, especially with a smoothed inversion. When comparing two resistors with identical resistivity thickness products, the one that is thicker will always have higher total gas in place volumes when calculated using Archie's equation. That is, if you were to halve the thickness of a resistor, the resistivity will double to maintain the same resistivity thickness product, but doubling the resistivity will not double the saturation calculated using Archie's equation. In this manner it is possible to overestimate hydrate saturation. Other inversions schemes, such as an L-1 norm inversion, where large jumps in model resistivity are preferred over smoothly varying resistivities, may be better suited for gas-in-place estimation.

A survey of the Santa Cruz Basin in the Outer California Borderlands found many instances of increased resistivities interpreted to be methane hydrate. Initial interpretation of the seismic data in the region, largely based on the presence of a bottom-simulating reflector, suggested that the hydrate should be present in the broad flat basin. While there was some increased resistivity associated with locations where high amplitude reflectors crossed the BSR, the vast majority of the high resistivity regions were found in basin flanks. These resistors, interpreted to be methane hydrate deposits, are typically associated with a structural migration pathway, such as a fault or dipping sedimentary beds. While the source of the methane in the Santa Cruz Basin is likely of biogenic and thermogenic origin, abiotic methane generation is possible given the unique geologic and tectonic history of the Outer Borderlands. A resistor similar to the one imaged at the Del Mar Seep was found on a ridge crest in the Santa Cruz Basin and interpreted to be a methane seep. The presence of hydrate at this site is corroborated by a seismic pull up structure, which would not have been identified as such were it not for the associated resistor. A second likely methane seep was found downslope on the same line, the presence of which was supported by qualitative dissolved methane concentration measurements.

While resistors in both the Del Mar Seep and the Santa Cruz Basin are interpreted to be the result of hydrate accumulations, both sites suffer from the lack of corroborating evidence. Ryan et al. (2012) discovered the Del Mar Seep as part of a broad seismologic and tectonic study of the Inner California Borderlands, while Maloney et al. (2015) focused on the tranpressional structure that hosts the Del Mar Seep using a suite of acoustic methods and shallow push cores (<10 cm penetration). Grupe et al. (2015) biologically analyzed these push cores to understand importance of the methane seep ecosystems. There are no seismic profiles across the seep, only a Chirp profile that shows blanking associated with free gas (Maloney et al., 2015). The Santa Cruz Basin has plenty of seismic data, but they are low-frequency, low-resolution, and were acquired almost 40 years ago. Neither the Del Mar Seep nor the Santa Cruz Basin have been drilled, either to recover hydrate or to log the wells. In order to advance the science of using CSEM methods for hydrate exploration, a survey is needed in a location of known hydrate deposits, with high resolution depth migrated seismic data that can be used to constrain resistivity inversions, and resistivity well logs that can be used to ground truth those inversions. Such a place is Walker Ridge 313 and Green Canyon 955 in the Gulf of Mexico.

Hydrates in the Gulf of Mexico are a difficult target for CSEM methods. At Walker Ridge 313, the site of a collaborative academic, government and industry study, hydrate deposits are deep, up to 800 m below seafloor. They are found in relatively thin beds, at most 30 m thick, and have modest resistivities that peak at 200 Ωm, but average about 10-20 Ωm across the entire bed (Cook et al., 2010). Additionally, the salt tectonics of the Gulf of Mexico produce strong resistors, in the form of solid salt bodies, as well as conductors, when high salinity brines form from dissolved salt. To determine if CSEM could feasibly be used to image hydrates in the Gulf of Mexico, models based on interpreted seismic sections coupled with resistivity well logs were constructed. The resulting models showed that while an 1100 m Vulcan array would be capable of sensing the hydrate, the base of the resistors, as well as the absolute resistivity of the resistors was much better recovered with a 1600 m array. With funding from the Department of Energy, in June of 2017 we surveyed 4 sites in the Gulf of Mexico. These sites will be cored as part an IODP-style drilling expedition planned for early 2020. The 1600 m Vulcan array is the longest bathymetry tracking deep towed array ever deployed (and recovered). Over the course of the two-week cruise, we collected 360 line km of data, representing the largest academic CSEM survey of a hydrate target. The Gulf of Mexico field experiment is only a part of the Department of Energy funded proposal. The other part is to measure resistivity of methane hydrate mixed with a variety of sediments in an attempt to understand the resistivity of realistic hydrate bearing sediments, and is being done as a collaborative effort between USGS, LLNL, and SIO. Previous work has focused on setting a baseline resistivity for pure hydrate, and hydrate mixed with clean sands, however such clean samples are rarely found in the natural environment. Extending this research to resistivity profiles inverted using CSEM methods, perhaps a more complete understanding of the relationship between hydrate saturation and resistivity can be found, decreasing our reliance on inappropriate mixing laws such as Archie's equation.

From an exploration standpoint, it is important for CSEM methods to be incorporated into prospect evaluation early in the development of hydrate exploration and recovery. CSEM methods have a longer history in the oil and gas field, where a resistivity anomaly is a very strong predictor of the presence of petroleum (Carstens et al., 2015). Despite the apparent usefulness of the method, it has not been widely adopted by the oil and gas industry. Only a few places worldwide have been surveyed with the intent to quantify hydrate as an energy source. One of those is in the Sea of Japan, where three CSEM surveys have taken place. The results are still largely confidential, but a press release from the Japanese Ministry of Economy, Trade, and Industry discussed the method they used to calculate gas in place at a single site in the Sea of Japan. First boreholes were logged, then hydrate was recovered from core samples, and finally a CSEM survey was conducted (Meti.go.jp, 2018). What is especially notable is the absence of seismic data to infer hydrate location or quantity. While this seems like progress, CSEM methods are still not part of the standard suite of survey tools used in site selection prior to a drilling campaign. There have been multiple production tests in Japan, China, and the Alaskan and Canadian arctic permafrost, none of which has been assessed using CSEM methods. India is also planning an extended production test in the Krishna Godavari basin, which also lacks a CSEM survey. This extended test was located during India's second National Gas Hydrate Programme drilling expedition, after the first failed to identify quantities of hydrate worth exploiting. A CSEM survey of the sites may have helped inform their site selection prior to the first expedition, possibly saving them four months of drill ship time. Methane hydrate deposits in the Santa Cruz Basin and the Del Mar Seep will never be drilled for energy; there are much cheaper and easier ways to extract natural gas in North America (e.g. fracking shale). Countries that lack conventional hydrocarbons, however, may view hydrate as a strategic reserve, critical to their national security (Yatsu, 2018).

CSEM methods have facilitated our understanding of hydrates role as an energy source, potential geohazard, global warming enhancer, and chemosynthetic ecosystem host. At various points in this thesis, the relative merits of seismic and CSEM data have been discussed, mostly pointing out the fallibility of using acoustic methods to detect hydrate deposits. However, it is the synthesis of these two geophysical tools, sensitive to two different parameters of the earth, that when combined, allow a comprehensive understanding of natural gas hydrate systems. While most well studied hydrate sites have been subjected to thorough seismic analysis, there is a dearth of high-quality CSEM data at these sites. Incorporating CSEM methods into the standard suite of (largely acoustic) geophysical tools used to evaluate hydrate presence, saturation, and extent will make our assessments of these systems more complete, accurate, and credible.

References

Anselmetti, F. S., & Eberli, G. P. (1993) Controls on sonic velocities in carbonates, PAGEOPH 141, 287–323.

Archie, G. E. (1942). The electrical resistivity log as an aid in determining some reservoir characteristics. Petroleum Transactions of AIME. 146: 54–62. doi:10.2118/942054-g.

Atwater, T., & Stock, J. (1998). Pacific-North America Plate Tectonics of the Neogene Southwestern United States: An Update, International Geology Review, 40:5, 375-402, DOI: 10.1080/00206819809465216

Atwater, T., (1998). Plate tectonic history of southern California with emphasis on the Western Transverse Ranges and Santa Rosa Island, in Contributions to the Geology of the Northern Channel Islands, Southern California, edited by P. W. Weigand, 1-8, Am. Assoc. of Pet. Geol., Pac. Sect., Bakersfield, Calif..

Bahr, D. B., Hutton, E., Syvitski, J., & Pratson, L., (2001). Exponential approximations to compacted sediment porosity profiles, Computers and Geosciences, 27, 691-700

Behl, R. J., (2012). The Monterey Formation of California: New Research Directions, AAPG Search and Discovery Article #10435

Bohannon, R. G., & Geist, E., (1998). Upper crustal structure and Neogene tectonic development of the California continental borderland: Geological Society of America Bulletin, v. 110, p. 779–800.

Boswell, R. & Collett, T. S. (2011). Current Perspectives on Gas Hydrate Resources, Energy Environ. Sci., 2011, 4, 1206–1215

Bouma, A. H. (1962). *Sedimentology of some Flysch deposits: a graphic approach to facies interpretation..* Amsterdam ; New York: Elsevier Pub. Co.

Brown, V., Hoversten, M., Key, K., & Chen, J., (2012). ”Resolution of reservoir scale electrical anisotropy from marine CSEM data.” GEOPHYSICS, 77(2), E147-E158. https://doi.org/10.1190/geo2011-0159.1

Burger, H. R., Sheehan, A. F., & Jones, C. H. (2006). Introduction to applied geophysics: Exploring the shallow subsurface. W.W. Norton.

Cannat, M., Fontaine, F., & Escartin, J., (2010). Serpentinization and associated hydrogen methane fluxes at slow spreading ridges, *in* Rona, P.A., et al., eds., Diversity of Hydrothermal Systems on Slow Spreading Ocean Ridges: American Geophysical Union Geophysical Monograph 188, p. 241–264, doi:10.1029/2008GM000760.

Carstens, H., Hartley, R., & Somarin, A. (2015). Three Disappointments in the Barents Sea. Retrieved from https://www.geoexpro.com/articles/2015/05/three-disappointments-in-the-barents-sea

Collett, T. S., & Ladd, J., (2000). Detection of gas hydrates with downhole logs, in: C.K Paull, R Matsumoto, P.J Wallace, W.P Dillon (Eds.), Proc. ODP, Sci. Results, vol. 164, Ocean Drilling Program, College Station TX, pp. 179–191

Collett T. S., Riedel, M., Cochran, J. R., Boswell, R., Presley, J., Kumar, P., Sathe, A. V., Sethi, A., Lall, M., Sibal, V., & NGHP Expedition 01 Scientists (2008) National Gas Hydrate Program Expedition 01 initial reports: Directorate General of Hydrocarbons, New Delhi

Collett, T., Lee, M., Lewis, R., Mrozewski, S., Guerin, G., Goldberg, D., & Cook, A., (2012). Gulf of Mexico gas hydrate joint industry project Leg II logging-while-drilling data acquisition and analysis. Journal of Marine and Petroleum Geology 34, 41-61.

Constable, S. C., R. L. Parker, & C. G. Constable (1987). Occam's Inversion: A practical algorithm for generating smooth models from EM sounding data, Geophysics, 52, 289–300.

Constable, S. & Srnka, L. J., (2007). An introduction to marine controlled-source electromagnetic methods for hydrocarbon exploration. GEOPHYSICS, 72(2), WA3-WA12. https://doi.org/10.1190/1.2432483

Constable S. (2010). Ten years of marine CSEM for hydrocarbon exploration, Geophysics, 75-5, 75A67-75A81.

Constable, S., Orange, A., & Key, K., (2015). And the geophysicist replied: "Which model do you want?". GEOPHYSICS, 80(3), E197-E212. doi: 10.1190/geo2014-0381.1

Constable, S., Kannberg, P. K., & Weitemeyer, K., (2016). Vulcan: A deep-towed CSEM receiver, Geochem. Geophys. Geosyst., 17, 1042–1064, doi: 10.1002/2015GC006174.

Cook, A., Mrozewski, S., Collett, T., & Boswell, R., (2009). Gulf of Mexico Gas Hydrate Joint Industry Project Leg II: Walker Ridge 313 LWD Operations and Results. Tech. rep.. Department of Energy https://www.netl.doe.gov/File%20Library/Research/Oil-Gas/methane%20hydrates/WR313LWDOps.pdf.

Cook, A. E., Anderson, B. I., Malinverno, A., Mrozewski, S., & Goldberg, D. S., (2010). Electrical anisotropy due to gas hydrate-filled fractures. GEOPHYSICS, 75(6), F173-F185. https://doi.org/10.1190/1.3506530

Cook, A. E., & Tost, B. C. (2014). Geophysical signatures for low porosity can mimic natural gas hydrate: An example from Alaminos Canyon, Gulf of Mexico, J. Geophys. Res. Solid Earth, 119, 7458–7472, doi:10.1002/2014JB011342.

Cook, A. E., & Waite, W. F. (2018). Archie's saturation exponent for natural gas hydrate in coarse-grained reservoirs. Journal of Geophysical Research: Solid Earth, 123, 2069–2089. https://doi.org/10.1002/2017JB015138

Crutchley, G. J., Mountjoy, J. J., Pecher, I. A., Gorman, A. R., & Henrys, S. A., (2016). Submarine Slope Instabilities Coincident with Shallow Gas Hydrate Systems: Insights from New Zealand Examples. In: Lamarche, G. (ed) Submarine Mass Movements and Their Consequences. Advances in Natural and Technological Hazards Research, vol 41. Springer, Switzerland, 371–380. doi:10.1007/978-3-319-20979-1_37

Du Frane, W. L., Stern, L. A., Weitemeyer, K. A., Constable, S., Pinkston, J. C., & Roberts, J. J., (2011). Electrical properties of polycrystalline methane hydrate, Geophys. Res. Lett., 38, L09313, doi:10.1029/2011GL047243.

Du Frane, W., Stern, L.A., Constable, S., Weitemeyer K. A., Smith, M.M., & Roberts, J.J., (2015). Electrical properties of methane hydrate sediment mixtures, J. Geophys. Res. Solid Earth, 120, 4773–4787, doi:10.1002/2015JB011940.

Edwards, R. N., (1997). On the resource evaluation of marine gas hydrate deposits using sea-floor transient electric dipole-dipole methods, Geophysics, 62(1), 63–74.

Edwards, R. N., (2005). Marine controlled source electromagnetics: Principles, methodologies, future commercial applications: Surveys in Geophysics, 26, 675–700.

Ellis, M.H., Sinha, M.C., and Parr, R., (2010). Role of fine-scale layering and grain alignment in the electrical anisotropy of marine sediments, First Break, 28 (9), 49-57.

Etiope, G., Schoell, M., & Hosgörmez, H., (2011). Abiotic methane flux from the Chimaera seep and Tekirova ophiolites (Turkey): Understanding gas exhalation from low temperature serpentinization and implications for Mars, Earth and Planetary Science Letters, 310, 1–2, 96-104, ISSN 0012-821X, https://doi.org/10.1016/j.epsl.2011.08.001.

Etiope, G., & Lollar., B. S. (2013). Abiotic methane on Earth, Rev. Geophys., 51, 276–299, doi: 10.1002/rog.20011.

Goswami, B. K., Weitemeyer, K. A., Minshull, T. A., Sinha, M. C., Westbrook, G. K., Chabert, A., Henstock., T. J., & Ker, S. (2015). A joint electromagnetic and seismic study of an active pockmark within the hydrate stability field at the Vestnesa Ridge, West Svalbard margin. Journal of Geophysical Research: Solid Earth, 120(10), 6797-6822.

Grant, N. J., & Whiticar, M. J., (2002). Stable carbon isotopic evidence for methane oxidation in plumes above Hydrate Ridge, Cascadia Oregon Margin. Global Biogeochem. Cycles 16 (4), 71-1–71-13.

Guerin, G., Goldberg, D., & Meltser, A., (1999). Characterization of in situ elastic proper- ties of gas hydrate-bearing sediments on the Blake Ridge. J. Geophys. Res. 104, 17781–17795.

Hadley, C., Peters, D., Vaughan, A., & Bean, D., (2008). Gumusut-Kakap project: geohazard characterization and impact on field development plans. In: Proceedings, International Petroleum Technology Conference, IPTC-12554.

Heeschen, K. U., Collier, R. W., de Angelis, M. A., Suess, E., Rehder, G., Linke, P., & Klinkhammer, G. P., (2005). Methane sources, distributions, and fluxes from cold vent sites at Hydrate Ridge, Cascadia Margin, Global Biogeochem. Cycles, 19, GB2016, doi:10.1029/2004GB002266.

Holbrook, W.S., Hoskins, H., Wood, W.T., Stephen, R.A., Lizarralde, D., & Leg 164 Science Party, (1996) Methane hydrate and free gas on the Blake Ridge from vertical seismic profiling, Science, 273, pp. 1840-1843

Hosgormez, H., Etiope, G., & Yalçın, M.N., (2008). New evidence for a mixed inorganic and organic origin of the Olympic Chimaera fire (Turkey): a large onshore seepage of abiogenic gas, Geofluids, 8 pp. 263-275

Hillman, J. I, T., Cook, A. E., Sawyer, D. E., Küçük, H. M., & Goldberg, D. S., (2017). The character and amplitude of 'discontinuous' bottom-simulating reflections in marine seismic data, Earth and Planetary Science Letters, 459, 157-169, ISSN 0012-821X, https://doi.org/10.1016/j.epsl.2016.10.058.

Hein, J. R., Normark, W. R., McIntyre, B. R., Lorenson, T. D., & Powell II, C. L., (2006). Methanogenic calcite, hydrate from a mud volcano offshore southern California, Geology, 34, 109–112.

Hyndman, R.D. & Spence, G.D., (1992). A seismic study of methane hydrate marine bottom simulating reflectors. J. Geophys. Res. 97, 6683. http://dx.doi.org/10.1029/92JB00234.

Ihsmarkit.com. (2018). Offshore Rig Day Rate Index | IHS Markit. [online] Available at: https://ihsmarkit.com/products/oil-gas-drilling-rigs-offshore-day-rates.html

IPCC, (2014). Climate Change 2014: Synthesis Report. Contribution of Working Groups I, II and III to the Fifth Assessment Report of the Intergovernmental Panel on Climate Change [Core Writing Team, R.K. Pachauri and L.A. Meyer (eds.)]. IPCC, Geneva, Switzerland, 151 pp.

Johnson, J. E., Mienert, J., Plaza-Faverola, A., Vadakkepuliyambatta, S., Knies, J., Bünz, S., Andreassen, K., Ferré, B., (2015). Abiotic methane from ultraslow-spreading ridges can charge Arctic gas hydrates. Geology ; 43 (5): 371–374. doi: https://doi.org/10.1130/G36440.1

Kannberg, P. K., Tréhu, A. M., Pierce, S. D., Paull, C. K., & Caress, D. W., (2013), Temporal variation of methane flares in the ocean above Hydrate Ridge, Oregon, Earth Planet. Sci. Lett., 368, 33–42, doi:10.1016/j.epsl.2013.02.030.

Key, K. (2016). MARE2DEM: a 2-D inversion code for controlled-source electromagnetic and magnetotelluric data. Geophysical Journal International. 207:571-588. doi:10.1093/gji/ggw290

Key, K., Constable, S., Matsuno, T., Evans, R., & Myer, D. (2012). Electromagnetic detection of plate hydration due to bending faults at the Middle America Trench, Earth Planet. Sci. Lett., 351–352, 45-53

Kvenvolden, K. A. (1993) Gas hydrates—geological perspective and global change. Rev Geophys 31(2):173–187

Lee, T. C., & Henyey, T. L., (1975). Heat flow through the southern California borderland, J. Geophys. Res., 80, 3733-3743.

Lee, M. W., Hutchinson, D. R., Collet, T. S., and Dillon, W. P., (1996). Seismic velocities for hydrate-bearing sediments using weighted equation, J. Geophys. Res., 101, 20, 347-20, 358.

Lee, M. W., (2004). Elastic velocities of partially gas-saturated unconsolidated sediments, Marine and Petroleum Geology, 21, 6, 641–650, doi:10.1016/j.marpetgeo.2003.12.004.

Lee, M. W. (2012), Isotropic, anisotropic, and borehole washout analyses in Gulf of Mexico Gas Hydrate Joint Industry Project Leg II, Alaminos Canyon well 21-A, U.S. Geol. Surv. Sci. Invest. Rep., 2012–5046, 23 pp.

Leifer, I., & MacDonald, I., (2003). Dynamics of the gas flux from shallow gas hydrate deposits: interaction between oily hydrate bubbles and the oceanic environment. Earth Planet. Sci. Lett. 210(3-4), 411-424. doi: 10.1016/S0012-821X(03)00173-0.

Leifer, I., Luyendyk, B. P., Boles, J., and Clark, J. F. (2006). Natural marine seepage blowout: Contribution to atmospheric methane, Global Biogeochem. Cycles, 20, GB3008, doi: 10.1029/2005GB002668.

Liu, X., & Flemings, P.B., (2007). Dynamic multiphase flow model of hydrate formation in marine sediments. J. Geophys. Res. 112, B03101. http://dx.doi.org/10.1029/2005JB004227.

MacDonald, I.R., Leifer, I., Sassen, R., Stine, P., Mitchell, R., & Guinasso Jr, N., (2002). Transfer of hydrocarbons from natural seeps to the water column and atmosphere, Geofluids, 2(2), 95-107.

Martin, B., & Fyfe W. S., (1970). Some experimental and theoretical observations on the kinetics of hydration reactions with particular reference to serpentinization: Chemical Geology , 6, 185–202, doi:10.1016/0009-2541(70)90018-5.

Matsumoto, R., Tanahashi, M., Kakuwa, Y., Snyder, G., Ohkawa, S., Tomaru, H., & Morita, S., (2017). Recovery of thick deposits of massive gas hydrates from gas chimney structures, eastern margin of Japan Sea: Japan Sea Shallow Gas Hydrate Project, Fire in the Ice, 17, 1, 1-6.

Majumdar, U., Cook, A.E., Shedd, W., & Frye, M., (2016). The connection between natural gas hydrate and bottom-simulating reflectors. Geophys. Res. Lett. 43, 7044–7051. http://dx.doi.org/10.1002/2016GL069443.

McConnell, D. R., Zhang, Z., & Boswell, R., Review of progress in evaluating gas hydrate drilling hazards, Marine and Petroleum Geology, Volume 34, Issue 1, June 2012, Pages 209-223, ISSN 0264-8172, https://doi.org/10.1016/j.marpetgeo.2012.02.010.

Mclver, R. D., (1977) Hydrates of natural gas–important agent in geological processes. Geol. Soc. Am. Abstr. Programs 9:1089–1090

Merewether, R., Olsson, M. S., and Lonsdale, P., (1985). Acoustically Detected Hydrocarbon Plumes Rising From 2-km Depths in Guaymas Basin, Gulf of California, J. Geophys. Res., 90(B4), 3075-3085.

Meti.go.jp. (2018). ANRE Estimated the Amount of Shallow Methane Hydrate Resources and Verified the Estimation Results (METI. [online] Available at: http://www.meti.go.jp/english/press/2016/0916_03.html [Accessed 2 Jul. 2018].

Milkov, A. V., Dickens, G. R., Claypool, G. E., Lee, Y. -J., Borowski, W. S., Torres, M. E., Xu, W., Tomaru, H., Tréhu, A. M., Schultheiss, P., (2004). Co-existence of gas hydrate, free gas and brine within the regional gas hydrate stability zone at the Southern Summit of Hydrate Ridge (Oregon margin): Evidence from prolonged degassing of a pressurized core, Earth Planet. Sci. Lett., 222, 829-843

Miller, K. C.. (2002); Geophysical evidence for Miocene extension and mafic magmatic addition in the California Continental Borderland. GSA Bulletin ; 114 (4): 497–512. doi: https://doi.org/10.1130/0016-7606

Mountjoy J. J., Pecher, I., Henrys, S., Crutchley, G., Barnes, P. M., & Plaza-Faverola, A., (2014). Shallow methane hydrate system controls ongoing, downslope sediment transport in a low-velocity active submarine landslide complex, Hikurangi margin, New Zealand. Geochem. Geophys. Geosyst. 15:4137–4156. doi:10.1002/2014GC005379

Myer, D., Constable, S., Key. K. (2011). Broad-band waveforms and robust processing for marine CSEM surveys. *Geophys. J. Int*., 184 (2): 689-698. doi: 10.1111/j.1365-246X.2010.04887.

Myer, D., Constable, S., Key. K., Glinsky, M. E., & Liu, G., (2012). Marine CSEM of the Scarborough gas field, Part 1: Experimental design and data uncertainty. GEOPHYSICS, 77(4), E281-E299. doi: 10.1190/geo2011-0380.1

Naif, S., Key, K., Constable, S. & Evans, R. L., (2015). Water-rich bending faults at the Middle America Trench. Geochem. Geophys. Geosyst. 16, 2582–2597.

Nicholson, C., Sorlien, C. C., Atwater, T., Crowell, J. C., & Luyendyk, B. P., (1994). Microplate capture, rotation of the western Transverse Ranges, and initiation of the San Andreas transform as a low-angle fault system. Geology ; 22 (6): 491–495.

Paganoni, M., Cartwright, J. A., Foschi, M., Shipp, R. C., and Van Rensbergen, P., (2016). Structure II gas hydrates found belowthe bottom-simulating reflector, Geophys.Res. Lett., 43, 5696–5706, doi:10.1002/2016GL069452.

Paull, C. K., Brewer, P.W., Ussler, W., Peltzer, E.T., Rehder, G., & Claque, D., (2003). An experiment demonstrating that marine slumping is a mechanism to transfer methane from the seafloor gas-hydrate deposits into the upper ocean and atmosphere. Geo-marine Letters, 22(4), 198-203.

Paull, C. K., Normark, W. R., Ussler III, W., Caress, D. W., & Keaten, R. (2008). Association among active deformation, mound formation, and gas hydrate growth and accumulation with the seafloor of the Santa Monica Basin, offshore California, Mar. Geol. 250, 258–275.

Paull, C. K., Caress, D. W., Lundsten, E., Anderson, K., & Gwiazda, R., (2011). Distinctive geomorphology of gas venting and near seafloor gas hydrate sites, Abstr. Programs Geol. Soc. Am. 43, 394.

Paull, C.K., Caress, D.W., Thomas, H., Lundsten, E., Anderson, K., Gwiazda, R., Riedel, M., McGann, M., & Herguera, J.C., (2015). Seafloor geomorphic manifestations of gas venting and shallow subbottom gas hydrate occurrences. Geosphere ; 11 (2): 491–513. doi: https://doi.org/10.1130/GES01012.1

Patton, J., (2018) "Earthquake Report: Channel Islands." Jay Patton Online, 5 Apr. 2018, 4:33 PM, earthjay.com/?p=7311.

Piper, K.A., & Ojukwu, C.O., eds. (2014). 2011 National Assessment of Oil and Gas Resources Assessment of the Pacific Outer Continental Shelf Region. Bureau of Ocean Energy Management OCS Report 2014-667, 243 p

Philip, B. T., Denny, A. R., Solomon, E. A., & Kelley, D. S., (2016). Time-series measurements of bubble plume variability and water column methane distribution above Southern Hydrate Ridge, Oregon, *Geochem. Geophys. Geosyst.*, 17, 1182–1196, doi:10.1002/2016GC006250.

Priegnitz, M., Thaler, J., Spangenberg, E., Schicks, J. M., Schrotter, J., & Abendroth, S., (2015). Characterizing electrical properties and permeability changes of hydrate bearing sediments using ERT data. Geophys. J. Int. 202, 1599–1612 doi: 10.1093/gji/ggv245

Proskurowski, G., Lilley, M.D., Seewald, J.S., Früh-Green, G.L., Olson, E.J., Lupton, J.E., Sylva, S.P., & Kelley, D.S., (2008). Abiogenic hydrocarbon production at Lost City Hydrothermal Field: Science , 319, 604–607, doi:10.1126/science.1151194.

Rehder, G., Brewer, P. W., Peltzer, E. T., & Friederich, G., 2002. Enhanced lifetime of methane bubble streams within the deep ocean. Geophys. Res. Lett. 29. doi:10.1029/2001GL013966.

Rehder, G., Leifer, I., Brewer, P. G., Friederich, G., & Peltzer, E. T., (2009). Controls on methane bubble dissolution inside and outside the hydrate stability field from open field experiments and numerical modeling. Mar. Chem. 114, 19-30.

Ritger, S., Carson. B., & Seuss, E., (1987). Methane-derived authigenic carbonates formed by subduction-induced pore-water expulsion along the Oregon/Washington margin. Geol. Soc.Am. Bull.; 98; 147-156

Sauter, E. J., Muyakshin, S.I., Charlou, J., Schlüter, M., Boetius, A., Jerosch, K., Damm, E., Foucher, J., & Klages, M., (2006). Methane discharge from a deep-sea submarine mud volcano into the upper water column by gas hydrate-coated methane bubbles. Earth Planet. Sci. Lett. 234(3-4), 354-365.

Schindler, C. S., (2010). 3D Fault Geometry and Basin Evolution in the Northern Continental Borderland Offshore Southern California: MS Thesis, California State College, Bakersfield. 42 p.

Schwalenberg, K., Haeckel, M., Poort, J., & Jegen, M. (2010). Evaluation of gas hydrate deposits in an active seep area using marine controlled source electromagnetics: Results from Opouawe Bank, Hikurangi Margin, New Zealand. Marine Geology, 272(1), 79-88.

Sleeper, K., Lowrie, A., Bosman, A., Macelloni, L., & Swann, C. T., (2006). Bathymetric mapping and high resolution seismic profiling by AUV in MC 118 (Gulf of Mexico). Offshore Technology Conference OTC18133. May 14, 2006

Shedd, W., Boswell, R., Frye, M., Godfriaux, P., & Kramer, K., (2012). Occurrence and nature of “bottom simulating reflectors” the Northern Gulf of Mexico. Mar. Pet. Geol. 34, 31–40.

Shipley, T. H., Houston, M. H., Buffler, R. T., Shaub, F. J., McMillen, K. J., Ladd, J. W., & Worzel, J. L., (1979). Seismic evidence for widespread possible gas hydrate horizons on continental slopes and rises. Am. Assoc. Pet. Geol. Bull. 63, 2204–2213.

Sloan, E. D., & Koh, C., (2007). *Clathrate hydrates of natural gases*, third ed. CRC Press, Florida.

Solomon, E.A., Kastner, M., MacDonald, I.R., & Leifer, I., (2009). Considerable methane fluxes to the atmosphere from hydrocarbon seeps in the Gulf of Mexico. Nat. Geosci. 2(8), 561-565.

Spangenberg, E., (2001). Modeling the influence of gas hydrate content on the electrical properties of porous sediments: Journal of Geophysical Research, 106, B4, 6535–6548, doi: 10.1029/2000JB900434.

Spangenberg, E., & Kulenkampff, J., (2006), Influence of methane hydrate content on electrical sediment properties, Geophys. Res. Lett., 33, L24315, doi:10.1029/2006GL028188.

Stolper, D. A., Lawson, M., Davis, C. L., Ferreira, A. A., Santos Neto, E. V., Ellis, G. S., Lewan, M. D., Martini, A. M., Tang, Y., Schoell, M., Sessions, A. L., & Eiler , J. M., (2014). Formation temperatures of thermogenic and biogenic methane, Science 27 344, 6191, 1500-1503, DOI: 10.1126/science.1254509

Teichert, B. M. A., Eisenhauer, A., Bohrmann, G., Haase-Schramm, A., Bock, B., & Linke, P., (2003). U/Th systematics and ages of authigenic carbonates from Hydrate Ridge, Cascadia Margin: recorders of fluid flow variations, Geochimica et Cosmochimica Acta, 67, 20, 3845-3857, ISSN 0016-7037, https://doi.org/10.1016/S0016-7037(03)00128-5.

ten Brink, U. S., Zhang, J., Brocher, T. M., Okaya, D. A., Klimgord, K. D., & Fuis, G. S., (2000). Geophysical evidence for the evolution of the California inner Continental Borderland as a metamorphic core complex, Journal of Geophysical Research, v.105, no.B3, p 5835-5857

Thomas, S. D. & La Pointe, P., (2009). Carbon Dioxide Resource Assessment –Oil and Gas Fields of California, Technical Memorandum, Golder Associates 063-1282.500.

Tréhu, A. M., Long, P. E., Torres, M. E., Bohrmann, G., Rack, F. R., Collett, T. S., Goldberg, D. S., Milkov, A. V., Riedel, M., Schultheiss, P., Bangs, N. L., Barr, S. R., Borowski, W. S., Claypool, G. E., Delwiche, M. E., Dickens, G. R., Gracia, E., Guerin, G., Holland, M., Johnson, J. E., Lee, Y. -J., Liu, C. -S., Su, X., Teichert, B., Tomaru, H., Vanneste, M., Watanabe, M., & Weinberger, J. L., (2004). Three-dimensional distribution of gas hydrate beneath southern Hydrate Ridge: constraints from ODP Leg 204, Earth and Planetary Science Letters, 222, 3–4, 845-862, ISSN 0012-821X, https://doi.org/10.1016/j.epsl.2004.03.035.

U.S. Geological Survey Alaska Gas Hydrate Assessment Team, (2013). National assessment of oil and gas project—geologic assessment of undiscovered gas hydrate resources on the North Slope, Alaska: U.S., Geological Survey Digital Data Series, p. 100, 69–CC, http://dx.doi.org/10.3133/ds69CC

Valentine, D. L., Blanton, D. C., Reeburgh, W. S., & Kastner, M., (2001). Water column methane oxidation adjacent to an area of active hydrate dissociation, Eel River Basin. Geochim. Cosmochim. Acta, 65, 2633-2640.

Victor, F. W. (1997). Outer Borderland Province. In C.A. Dunkel and K.A. Piper, eds. 1995 National Assessment of United States Oil and Gas Resources Assessment of the Pacific Outer Continental Shelf Region. US Minerals Management Service OCS Report 97-0019 p.151-153.

Weitemeyer, K. A., Constable, S. C., Key, K. W., & Behrens, J. P. (2006). First results from a marine controlled-source electromagnetic survey to detect gas hydrates offshore Oregon. Geophysical Research Letters, 33(3).

Weitemeyer, K., & Constable, S. (2010). Mapping shallow geology and gas hydrate with marine CSEM surveys, First Break, 28, 97–102.

Weitemeyer, K. A., Constable, S. & Tréhu, A. M. (2011). A marine electromagnetic survey to detect gas hydrate at Hydrate Ridge, Oregon. Geophysical Journal International, 187: 45–62. doi:10.1111/j.1365-246X.2011.05105.x

Weitemeyer, K. A., & Constable, S. (2011) Mapping Gas Hydrates with Marine Controlled Source Electromagnetics, In: Proceedings of the 7th International Conference on Gas Hydrates (ICGH 2011), Edinburgh, Scotland, United Kingdom, July 17-21.

Westbrook, G.K., Carson, B., Musgrave, R.J., et al. (1994). Proc. Ocean Drill. Prog. Init. Reports 146 (Part 1). College Station, TX (Ocean Drilling Program). doi:10.2973/odp.proc.ir.146-1.1994.

Whiticar, M. J., (1999). Carbon and hydrogen isotope systematics of bacterial formation and oxidation of methane, Chem. Geol., 161 (1999), pp. 291-314

Willoughby, E. C., & Edwards, R. N., (1997). On the resource evaluation of marine gas-hydrate deposits using seafloor compliance methods, Geophysical Journal International, 131, 3, , 751–766, https://doi.org/10.1111/j.1365-246X.1997.tb06610.x

Yatsu, M. (2018). Will ‘Flammable Ice’ Be a Critical Factor in Asia’s Regional Security?. [online] The Diplomat. Available at: https://thediplomat.com/2018/06/will-flammable-ice-be-a-critical-factor-in-asias-regional-security/

Yelisetti, S., Spence, G. D., Riedel, M., (2014). Role of gas hydrates in slope failure on frontal ridge of northern Cascadia margin. Geophys J Int 199(1):441–458. doi:10.1093/gji/ggu254